The Effect of Molecular Vibrations and Surface Structure on the Chemisorption of Methane on Platinum

PAR

Marco SACCHI

laurea in ingegneria chimica, Politecnico di Milano, Italie
et de nationalité italienne

EPFL

ÉCOLE POLYTECHNIQUE
FÉDÉRALE DE LAUSANNE

Suisse
2008

a

Abstract

In this thesis, I report state-resolved measurements of the chemisorption probability of CH_4 on Pt(111) and Pt(110)-(1×2) for several rovibrationally excited states ($2\nu_3$, $\nu_1+\nu_4$, and $2\nu_2+\nu_4$) in addition to the ground state. Measurements of the state resolved reactivity as function of the incident translational energy lead to state-resolved reactivity curves for each of the states under study. The relative efficacy of activating the dissociation reaction is obtained for each excited state by comparing the increase in reactivity observed upon excitation of a particular state to the effect of increasing the translational energy of CH_4 in the ground state.

The results provide clear evidence for mode specific reactivity with the highest efficacy for the stretch-bend combination ($\nu_1+\nu_4$), followed by the stretch overtone ($2\nu_3$) and the bend overtone state ($2\nu_2+\nu_4$). The results demonstrate that vibrational activation of CH_4/Pt chemisorption process does not simply scale with the total internal energy of the incident CH_4 molecule, which is a central assumption of the PC-MURT statistical model for dissociative chemisorption reactions developed by the group of Harrison [Ukraintsev *et al.*, Chem. Phys., 1994. **101**(2): p. 1564]. On the contrary, the qualitative predictions of the vibrationally adiabatic model proposed by Halonen *et al.* [J. Chem. Phys., 2001. **115**(12): p. 5611] are in good agreement with our results. The higher efficacy of the $\nu_1+\nu_4$ state can also be rationalized by observing that, at the transition state, the breaking C-H bond is both stretched and bent from its equilibrium geometry, therefore I suggest that this state might have a significant projection on the reaction coordinate [Psofogiannakis *et al.*, J. Phys. Chem. B, 2006. **110** : p. 24593 ; Anghel *et al.*, Phys. Rev. B, 2005. **71** : p. 4]. Comparison between the state-resolved reactivity for $CH_4(2\nu_3)$ on Pt(111) and Ni(111) is used to obtain information about differences in barrier height and transition state location for the dissociation on the two different metals [Bisson *et al.*, J. Phys. Chem., 2007. **111**: p. 12679].

Finally, for the more corrugated Pt(110)-(1×2) surface, I determined the state-resolved sticking coefficients for different polar and azimuthal angles of incidence. Comparison between the reaction probability for incidence parallel and perpendicular to the missing rows of this

surface shows shadowing effects that are consistent with predominant reactivity of the top layer Pt atoms.

c

Version abrégée

Dans ce mémoire de thèse, je présente des mesures résolues en états quantiques de la probabilité de réaction de chimisorption dissociative du CH_4 sur le Pt(111) et le Pt(110)-(1×2), pour plusieurs états ro-vibrationnels excités ($2\nu_3$, $\nu_1+\nu_4$, and $2\nu_2+\nu_4$) ainsi que pour l'état fondamental. Ces mesures de réactivité résolues en états quantiques, effectuées en fonction de l'énergie translationnelle incidente du CH_4, donnent des courbes de réactivité résolue en états quantiques pour chaque état étudié. L'efficacité relative de l'activation de la réaction est obtenue pour chaque état excité en comparant l'augmentation de réactivité due à l'excitation de l'état avec l'effet de l'augmentation de l'énergie translationnelle du CH_4 dans son état fondamental.

Ces résultats procurent une preuve claire d'une réactivité spécifique au mode de vibration, avec la plus grande efficacité pour la combinaison d'élongation-déformation ($\nu_1+\nu_4$), suivie par la première harmonique d'élongation ($2\nu_3$) et l'harmonique de déformation ($2\nu_2+\nu_4$). Ces résultats démontrent que l'activation vibrationnelle de la chimisorption du CH_4 sur le Pt n'est pas simplement proportionnelle à l'énergie interne de la molécule de CH_4 incidente, proportionnalité qui est l'hypothèse centrale du modèle statistique pour les réactions de chimisorption dissociative PC-MURT, développé par le groupe de Harrison [Ukraintsev *et al.*, Chem. Phys., 1994. **101**(2) : p. 1564]. A l'inverse, les prédictions qualitatives du modèle vibrationnel adiabatique proposé par Halonen *et al.* [J. Chem. Phys., 2001. **115**(12) : p. 5611] sont en bon accord avec nos résultats. La plus grande efficacité de l'état $\nu_1+\nu_4$ peut aussi être rationalisée en observant que, à l'état de transition, la liaison C-H rompue est à la fois allongée et déformée par rapport à la géométrie d'équilibre, par conséquent je suggère que cet état pourrait avoir une projection significative sur les coordonnées de réaction [Psofogiannakis *et al.*, J. Phys. Chem. B, 2006. **110** : p. 24593 ; Anghel *et al.*, Phys. Rev. B, 2005. **71** : p. 4]. Par ailleurs, des comparaisons entre la réactivité résolue en états quantiques du $CH_4(2\nu_3)$ sur le Pt(111) et sur le Ni(111) sont utilisées pour obtenir des informations sur la différence de hauteur de barrière et la localisation relative de l'état de transition pour la dissociation sur les deux métaux [Bisson *et al.*, J. Phys. Chem., 2007. **111** : p. 12679].

Finalement, j'ai déterminé la réactivité résolue en états quantiques du CH_4 sur la surface de Pt(110)-(1×2), plus corruguée, pour différents angles d'incidence polaire et azimutal. La comparaison de la probabilité de réaction pour une incidence parallèle et perpendiculaire aux structures de colonnes manquantes, typique de cette surface, montre des effets d'ombrage, cohérents avec une réactivité prédominante des atomes de Pt de la couche supérieure.

Mots clefs : méthane, chimisorption, Pt(111), Pt(110), énergie vibrationnelle, réactivité résolue en états quantiques, spécificité d'état, dépendance angulaire.

Index

iii

Chapter 1:   Introduction

1.1   Motivation

Since the beginning of the XXth century, the scientific community has devoted an enormous effort in the study of surface reactions. The motivation for such an effort is well described in the presentation of the 2007 Nobel Laureate for Chemistry, Gerhard Ertl: "*Chemical reactions on solid surfaces are very important in our everyday live but difficult to study*"[1]. Detailed studies of elementary chemical processes on well-characterized single crystal surfaces have contributed substantially to the understanding of heterogeneous catalysis. A few specific examples are given below to underline the central role of gas-surface reactions and catalysis in several chemical processes used in industry.

Chemical vapor deposition, oxidation, ion implantation and etching are key steps in the manufacturing of microelectronic devices, and a detailed understanding of these processes requires fundamental studies of the dynamics of the gas-surface interactions. In the *Haber-Bosch* process, nitrogen is extracted from the air and reacted with hydrogen to produce ammonia (NH_3). This is an important raw material for the production of synthetic fertilizers and explosives and the reaction uses an iron catalyst. Steam reforming, which converts natural gas and water into H_2 and CO, is of tremendous economical importance because it is the dominant method for large-scale production of hydrogen, as well as the starting point for many synthetic processes in the petrochemical industry.

The rate-limiting step in these processes is often the adsorption of one of the gas phase reagent molecules (N_2, or CH_4) on the catalyst surface. Understanding the mechanism by which a relatively inert molecule becomes the precursor of a wide series of chemical compounds is the reason that motivates us to explore the details of the adsorption mechanism. In order to reduce the energy consumption associated with this key process, one could ask, for example: "what is the most efficient way to promote the reaction?" or, more specifically: "Will vibrational

excitation of the reactants promote the reaction more efficiently than increasing their kinetic energy?", and again "which surface sites are the most reactive for dissociating the impinging molecules?". To these and several others questions we can try to answer only by systematically analyzing, one by one, the effect of all the several parameters that influence the adsorption probability such as:

- the catalyst surface composition, orientation and temperature;
- the translational energy and the angle(s) of incidence of the reagent molecules;
- the initial electronic, vibrational and rotational quantum state of the reagent molecules;
- the molecular orientation and the surface impact site.

Several of these parameters are schematically represented in Figure 1.1.
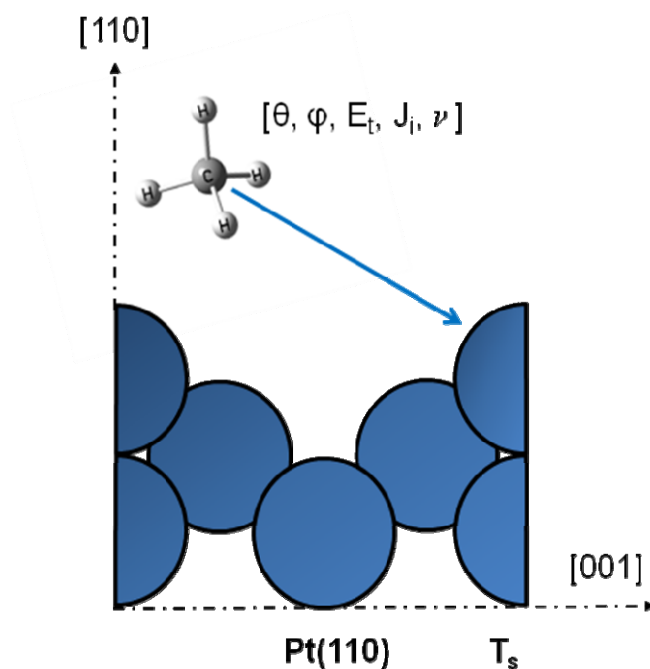
Figure 1.1 Parameters that influence the probability of adsorption, of CH_4 on Pt(110). E_t, J_i, ν_I indicate the translational energy, the rotational and the vibrational state of the incident molecule. θ an φ indicate the polar and azimuthal angle of incidence. The crystallographic plane of the surface, in this case the (110), and the surface temperature T_s are also important, as well as the orientation of the approaching molecule and the impact site (in this case a top atom).

At the end, our goal is to reach, for gas-surface reactions, the same level of understanding that we have now for the dynamics of gas-phase reactions. In the following section, I will first introduce some of the most recent and important results in gas-phase reaction dynamics. From these, I will move to surface dynamics and I will try to make you appreciate how, in the last 10 years, "*surface dynamicists*" have struggled in the effort to reach a molecular-scale description of the adsorption mechanism. We have partially succeeded in this goal by continuously developing new experimental and theoretical methods and by cleverly applying "old" gas-phase dynamics ideas to new systems.

1.2   Gas-surface dynamics

The goal of chemical reaction dynamics[2] is to explore the mechanism of chemical reactions at the microscopic level. A complete understanding of a complex chemical reaction can be obtained only from the systematic study of each of the elementary steps involved in the overall reaction. By measuring the reaction probability as a function of different initial quantum states of the adsorbing molecules, it is possible to acquire information on several interesting aspects of the chemisorption mechanism, and among them:

- the energy requirement for a gas-surface reaction;
- the efficacy of the vibrational energy compared to the translational energy;
- the effect of the initial rotational and vibrational quantum state of the reactants on the reaction probability.

Furthermore, by averaging the "microscopic" (state-specific) reaction rates over the reactant state distributions, it is possible to calculate macroscopic reaction rates. In the following part, I first present some of the classic topics on gas-surface interactions. In this short introduction I do not pretend to be exhaustive, but my purpose is rather to introduce some key concepts, such as the potential energy surface or the reaction pathway.

In the second part, I review previously reported state-resolved studies of gas-phase and gas-surface reactions. I found it useful to review some of the most significant examples of state-resolved gas-phase reactions because they have "shown us the way" to advance in the

understanding of the reactions mechanism by precisely controlling the initial vibrational state of the reactants and by monitoring the final state of products. The last section is dedicated to previous results in state-resolved gas-surface dynamics. In this context the dissociative chemisorption of CH_4 on metal surfaces has become a benchmark reaction for gas-surface reaction dynamics.

1.3   Gas-surface interactions

We define adsorption as a process where molecules from gas-phase become trapped on a solid surface. From the nature of the bond between the adsorbate and the surface we can distinguish two extreme cases of adsorption: physisorption, and chemisorption. In the physisorption process there is no direct bond formation between the adsorbed molecule and the surface, and the binding is through van der Waals forces. Conversely, a chemisorption process involves the creation of a chemical bond between the adsorbate and the surface as a result of the electron sharing between the molecular orbitals and the surface electron bands. In some cases the interaction with the surface will cause the weakening or even the breaking of one or more intramolecular bonds, in this case the adsorption process is defined as dissociative chemisorption[3].

The interaction between a surface and a molecule is described by its potential energy U, where the bound state corresponds to the local minima of U. The potential energy can be written as a function of the coordinates of the nuclei of the system using the Born-Oppenheimer approximation (BOA), which assumes that the motion of the nuclei is much slower than that of the electrons. For molecule-surface interactions, a diatomic molecule over a surface is the simplest case that we can consider. Under this condition, the potential energy can be written as $U(x, y, z, d, \gamma, \varphi, u_i)$, where (x, y, z) are the coordinates of the molecular center of mass relative to some point on the surface, d is the intramolecular bond length, γ is the polar angle of the bond with respect to the surface normal, φ the azimuth angle, and u_i the displacement of the surface atom i with respect to its unperturbed equilibrium position. U is typically referred to as a potential energy surface (PES)[4]. Since the full multidimensional PESs are computationally

demanding, gas-surface interactions are mostly discussed in terms of reduced dimensionality models.

Lennard-Jones[5] proposed, in 1932 for the first time, a simple model to describe the dissociative adsorption of a diatomic molecule. In the Lennard-Jones model, the PES is considered as a 1-dimensional potential $U(z)$ depending only on the molecule surface distance as shown in Figure 1.2.
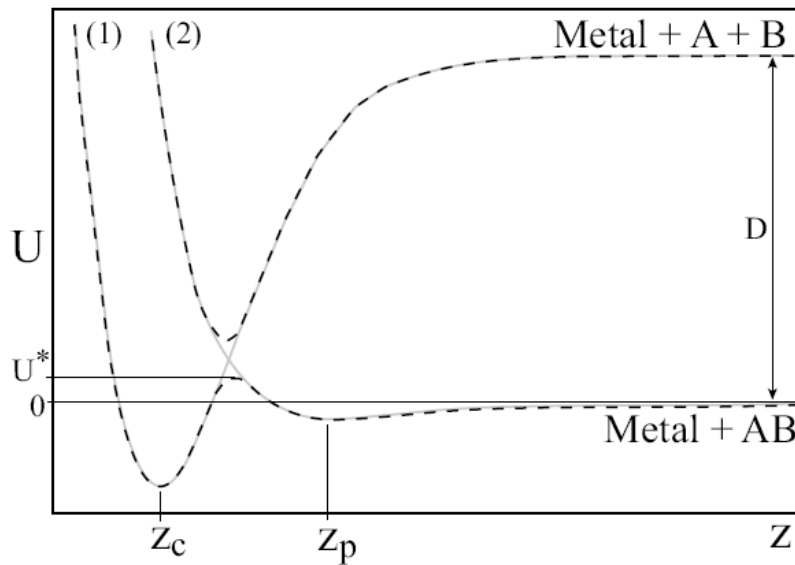

Figure 1.2 Lennard-Jones one-dimensional PES describing the dissociative adsorption of a diatomic molecule on a surface. The solid lines (1) and (2) represent the diabatic potential curves describing the interaction of the molecule AB as well as its constituent atoms with a metal surface. The dashed line are the adiabatic curves, the lower one represent the electronic ground state[5, 6].

The solid curve (2) gives the potential energy of a diatomic molecule AB as a function of the surface-molecule distance z. The minimum at z_p is the bottom of the physisorption well. Curve (1) is the potential of the molecule-constituent atoms which are chemisorbed on the surface at z_c. At large z, i.e. in the gas phase, the difference in energy between the two curves is the binding energy D of the molecule.

When the BOA holds, the electronic state of the system is not affected by the translational energy of the nuclei and the energy levels are not allowed to cross. Diagonalization of the potential described by the diabatic levels (1) and (2) produces two new PESs (dashed line) which are referred to as adiabatic curves. If V_1 and V_2 are the energy of the diabatic states 1 and 2, the

5

adiabatic levels have energy equal to $V_{\pm} = \frac{1}{2}\left[(V_1 + V_2) \pm \sqrt{(V_1 - V_2) + 4V_{12}^2}\right]$, where V_- indicates

the energy of the electronic ground state. The term V_{12} is a coupling term that indicates to what extent the state 1 (molecule-surface) mixes with the state 2 (atoms-surface). The BOA usually holds if V_{12} is large[7]. A molecule impinging on the surface with sufficiently high kinetic energy can overcome the barrier U^* and reach the bottom of the chemisorption well at z_c where the intermolecular bond is broken and two atom-surface bonds are formed.

However, PESs depending only on z are not realistic, since they do not describe the changing in the interatomic distances as the molecule approaches the surface. Thus, the next coordinate to include in the PES model is the interatomic distance r. Two dimensional PESs are usually visualized by means of contour plots, where equipotential lines are plotted as a function of the two coordinates z and r. An example of 2D PES surface is shown in Figure 1.3.
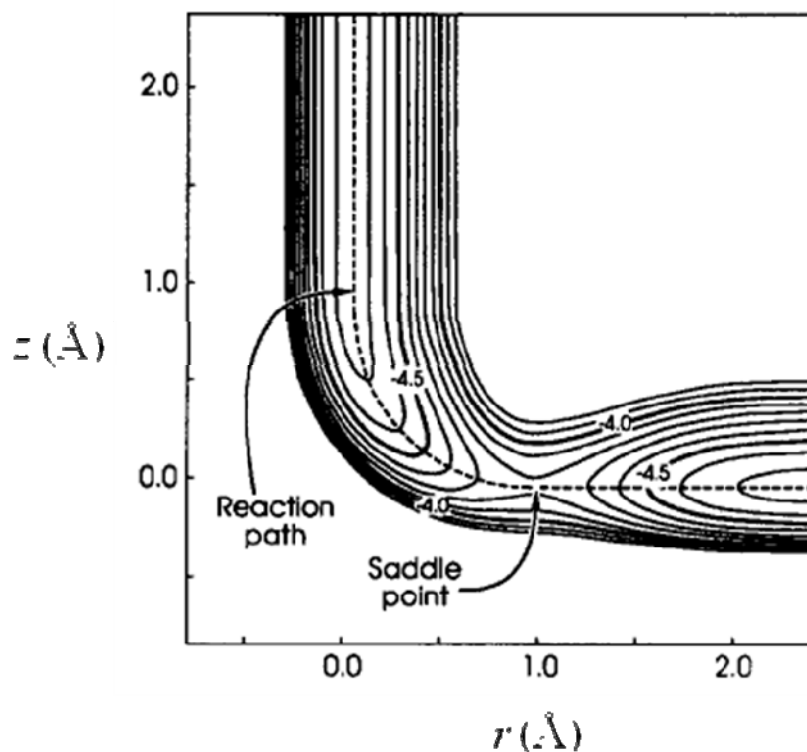
Figure 1.3 Two dimensional (z, r) PES used to model the interaction between H_2 and a metal surface[8]. z indicates the distance between the centre of mass of the H_2 molecule and the surface, and r is the H-H bond length. The dashed line identifies the reaction path, defined as the minimum energy path from the reactant (entrance valley) to the products (exit valley). The reaction path crosses the energy barrier at the saddle point of the PES.

The PES is constructed by calculating, with *ab initio* or semi-empirical methods, the total energy as a function of the coordinates *z and r* [9-11]. Two important features of a PES are indicated in Figure 1.3. The first one, the *reaction coordinate*, is the minimum energy path from the reactants to the products. The point where the reaction path crosses a saddle point on the PES can be identified as the *transition state* of the reaction and the difference in energy between the reagents and the transition state gives the energy barrier of the reaction[9].

Another key feature of the PES is the location of the transition state along the reaction path between the entrance and exit valleys. One can distinguish between an "early" or "attractive" potential, for which the transition state is located within the entrance valley, meaning along the *z* coordinate representing the separation between the molecule and the surface, and a "late" or "repulsive" potential, where the saddle point is located in the "exit valley", along the coordinate representing the elongation of the breaking bond. Polanyi's rules [8, 12] state that an early barrier is more readily surmounted by initial translational energy, on the other hand, a late barrier can be overcome more easily by vibrational excitation. The rapidly increasing computational power has recently allowed the calculations of full six-dimensional potential energy surfaces for dissociation of H_2 on metal surfaces[10, 13-15] and the results of such high-level calculations have largely confirmed the predictions made from these simples rules. However, it is considerably more challenging to incorporate all the internal degrees of freedom of a polyatomic molecule into full-dimensional *ab initio* calculations. In this context, the dissociative chemisorption of CH_4 on metal surfaces has become a benchmark for quantum reaction dynamics studies.

1.4   Bond- and mode- selective reactions in gas phase

Reactant excitation to specific vibrational quantum states combined with state resolved product detection makes possible to explore the role of vibrational energy, energy partitioning and internal energy redistribution in chemical reactions[16, 17].

Yoon *et al.*[18] explored the effect of the CH_4 stretch excitation on the reaction: $CH_4 + Cl \rightarrow CH_3 + HCl$. They prepared CH_4 in two isoenergetic vibrationally excited states, the symmetric stretch–bend combination (v_1+v_4) and the antisymmetric stretch–bend combination (v_3+v_4). Their results show that vibrational excitation of methane to the (v_1+v_4) state promotes the reaction more efficiently than excitation to the (v_3+v_4) state by a factor of 2. This observation is consistent with theoretical calculations that predict a stronger coupling of the symmetric stretching vibration to the reaction coordinate than the antisymmetric stretch[19-21].

Bechtel *et al.*[22] investigated the reaction between CD_2H_2 and a chlorine atom. They observed that excitation of the first C-H stretch overtone of CH_2D_2 leads to a preference for hydrogen abstraction over deuterium abstraction, whereas excitation of the first C-D overtone of CH_2D_2 reverses this preference. Reactions with CH_2D_2 prepared in a local mode state containing two quanta of C-H stretch in a single C–H oscillator ($|2000\rangle^-$) or in a local mode containing one quantum each in two C–H oscillators ($|1100\rangle$) lead to very different product state distributions, although the vibrational energy for each mode is nearly identical. The $Cl + CH_2D_2|2000\rangle^-$ reaction yields methyl radical products primarily in their ground state, whereas the $Cl + CH_2D_2|1100\rangle$ reaction yields methyl radical products that are C–H stretch excited. Their results are consistent with a simple spectator model and the observed bond selectivity in the $Cl + CH_2D_2$ reaction shows that the prepared vibrational motion remains localized during the timescale of the reaction.

Yoon *et al.* reported experimental and theoretical investigation on the reactivity of the symmetric (v_1) and antisymmetric (v_4) C-H stretching vibrations of monodeuterated methane (CH_3D) with photolytic chlorine atoms (Cl, $^2P_{3/2}$). Their results show that the symmetric C-H stretching vibration v_1 promotes the reaction seven times more efficiently than the antisymmetric C-H stretching vibration v_4 [23, 24]. Since the v_1 and v_4 modes have similar energies and vibrational motions that differ primarily by the phase of the C-H bond stretches, the difference in reactivity of the symmetric and antisymmetric C-H stretching vibrations could not be explained in terms of a spectator model and bond-specific reactivity as in the case of CD_2H_2[22]. Thus, they performed *ab initio* calculations of the vibrational energies and eigenvectors along the reaction coordinate and found that this difference arises from changes in the initially excited

stretching vibrations as the reactive Cl atom approaches. In the vibrationally adiabatic limit, the ν_1 vibration of CH_3D becomes localized into the vibrational excitation of the C-H bond pointing toward the Cl atom, promoting the abstraction reaction. On the contrary, the vibrational energy initially in the ν_4 state flows into the three C-H bonds pointing away from the approaching Cl atom and remains unperturbed during the reaction.

For the reaction: $CD_3H + Cl \rightarrow CD_3 + HCl$, Yan *et al.*[25] investigated the relative efficiency of vibrational energy compared to the translational energy. In their crossed molecular beam experiment, they tuned the translational energy of the reactants by changing the intersection angle between the Cl and the CD_3H beams. Their results show that excitation of the C-H stretching vibration is as efficient as the translational energy in promoting the H abstraction reaction. They also reported that thermal excitation of the CD_3H bending modes is only slightly more effective than translational energy.

In conclusion, this overview of state-resolved experiments on reactions in the gas phase shows that it is possible to control both the branching ratio between different channels and the reaction rate of a specific channel by preparing the reactant in a specific vibrational quantum state. Encouraged by these results on gas-phase reactions, scientists have extended state-resolved studies to gas-surface reactions, where a solid surface is one of the reactions partners. In the following section, I will review results on chemisorption of methane on metal surfaces, which has become the most important prototype system for studying the interaction of polyatomic molecules with a surface

1.5   State specific gas-surface reactions

The introduction of supersonic molecular beam techniques in surface science allowed the investigation of gas-surface reactions with better control of the initial translational energy and direction of the incident molecules[26, 27]. More recently, the addition of laser excitation in molecular beams has proven to be a powerful tool to precisely control the initial rotational and vibrational state of the reactant molecules. In this section, I review in chronological order the most important examples of state-specific reactivity measurements for gas-surface reactions.

In 1999, Juurlink *et al.*[28] demonstrated for the first time the feasibility of state-resolved sticking coefficient measurements. They reported the sticking probabilities of methane excited to $v = 1$ state of the antisymmetric C-H stretch vibration v_3. The v_3 excited molecules were found to be up to 1600 times more reactive than the molecules in $v = 0$ on a Ni(100) surface. Their results also show that the excitation of one quantum of v_3 (36 kJ/mol) is about as effective as an equivalent amount of translational energy in promoting the reaction. They estimated that methane excited to v_3 contributes less than 2% to the reactivity measured by hot-nozzle molecular-beam experiments [29] and suggest that vibrational modes other than v_3 must play a significant role in the vibrational activation of methane chemisorption on Ni(100).

In order to treat theoretically the vibrational activation of methane chemisorption, Halonen *et al.*[30] applied a vibrationally adiabatic approach to simulate the interaction of a vibrating CH_4 molecule close to a flat nickel surface. They predict that the vibrational energy of the symmetric and antisymmetric stretches becomes localized in the proximal and distal C-H bonds, respectively, during the adiabatic approach toward the surface, and based on this they suggest that $CH_4(v_1)$ should be significantly more reactive than $CH_4(v_3)$ in the adiabatic limit.

In 2001, Higgins *et al.*[31] reported the state-resolved reactivity of methane excited to the first overtone of the antisymmetric stretch $2v_3$ on Pt(111). It was found that the sticking coefficient of methane with 5.4 kJ/mol of normal translational energy increases by a factor of 30 upon vibrational excitation. They estimated that 72 kJ/mol of vibrational energy in the $2v_3$ state of CH_4 is approximately equivalent to 30 kJ/mol of normal translational energy. This corresponds to a vibrational efficacy of 40% compared to the translational energy.

In 2002, our group reported the sticking probability of methane excited to the $2v_3$ state on Ni(100)[32]. Our results showed that the vibrational energy in the $2v_3$ is about 90% as efficient as the translational energy in promoting the reaction.

In 2003, Beck *et al.*[33] reported that CD_2H_2 is 5.4 times more reactive when it is excited to the |20> local mode state than the |11> state, despite the fact that these two states are nearly isoenergetic. The increased reactivity of the |20> state relative to |11> state was rationalized in terms of their different vibrational amplitudes: the former contains two quanta of stretch vibration in a single C-H bond, whereas the latter contains one quantum in each of two C-H bonds. This was the first observation of mode-specific behavior for gas-surface reactions. In

10

2004, Smith *et al.*[34] measured the state-resolved sticking coefficient of $CH_4(\nu_3)$ on Ni(111) and observed that the ν_3 excitation is 25% more effective at promoting the dissociative chemisorption than is the translational energy. They argued that an efficacy higher than 1.0 can result either from lattice recoil, where some translational energy is lost to the motion of the surface, or from nonadiabatic dynamics, where $v = 0$ molecules cannot access the minimum TS energy.

In 2005, Juurlink *et al.*[35] performed state-resolved measurements on Ni(100) and Ni(111) for CH_4 excited to $v = 3$ state of the ν_4 bend vibration. They found that that $3\nu_4$ state was significantly less effective than the ν_3 C-H stretch at promoting the dissociative chemisorption of CH_4, even though $3\nu_4$ contains 30% more energy.

In the same year, Maroni *et. al.* [36] reported that the reactivity of CH_4 excited in its symmetric stretch ν_1 mode is about one order of magnitude higher than that of CH_4 excited to the antisymmetric stretch ν_3. In this case, the difference in reactivity between two isoenergetic vibrational states does not depend on the quantity of vibrational energy contained in each bond, but is determined by the symmetry of the vibrational state excited. This result confirms the prediction of the vibrationally adiabatic model proposed by Halonen *et al.*[30].

In my thesis work, I performed state-resolved measurements of the CH_4 sticking probability on two different crystallographic planes of platinum. The goal of these measurements is to probe the role of vibrations and surface structure in the dissociative chemisorption of methane. In particular, we compare the state resolved reactivity of several nearly isoenergetic vibrational quantum state of CH_4. For the Pt(110) surface, we also measured the polar and azimuthal angular dependence of the state-resolved sticking probability. Furthermore, we show that the corrugated structure of the surface allow us to obtain site specific information on the chemisorption probability. In conclusion, by providing stringent tests of available theoretical models[30, 37, 38], our measurements contribute to the progress in the understanding of gas-surface dynamics.

1.6   Outline of this thesis

In Chapter 2, I describe the experimental apparatus and methods that we use to study the reactivity of methane in vibrationally excited states.

In Chapter 3, I report the state-resolved reactivity of methane on Pt(111) as a function of the normal translational energy. Comparison is made between our results and previous reported measurement on the similar Ni(111) surface.

In the first part of Chapter 4, I describe our state-resolved reactivity measurements for ground state and vibrationally excited CH_4 on Pt(110)-(1×2). In the second part of the chapter, I show how we changed the polar and azimuthal angles of incidence to determine the reaction probability on select surface sites.

In Chapter 5, I summarize the most significant results of my work and I give an outlook for possible future experiments.

Chapter 2:   Experimental setup

2.1   Introduction

Our state-resolved sticking coefficient measurements are performed in a molecular beam/surface science apparatus designed to study the surface interactions of laser-excited molecules. Since the apparatus has been described previously in detail[39], I only summarize here the most important features. A pulsed molecular beam source is used to prepare a molecular beam of CH_4 with well defined kinetic energy. The translational energy of the beam is controlled by using different carrier gases (H_2, He and Ar) and by changing the seed/carrier gas ratio. To investigate the effect of vibrational excitation, we excite methane molecules to specific rovibrational states by intense infrared laser pulses. We perform timed exposures of the clean sample surface to a molecular beam of CH_4 with and without laser excitation under otherwise identical conditions. After the deposition, the laser-off and laser-on sticking coefficients are determined by detecting chemisorbed carbon by Auger Electron Spectroscopy (AES).

The experimental apparatus consists of four main parts:

1. Pulsed molecular beam source
2. Ultra high vacuum (UHV) surface science chamber
3. Pulsed infrared laser setup
4. Cavity ring-down spectroscopy setup

In this chapter, I will give a description of each subunit of the apparatus. For the components used in previous works of our group only a brief summary is presented and more detailed

descriptions can be found in the doctoral theses of Mathieu Schmid[40], Plinio Maroni[6] and Tung Thanh Dang[41].

2.2 Pulsed molecular beam source

Our pulsed molecular beam source is commercially available (Thermionics, MSC-9800) and consists of three differential pumping stages within a distance of 11 cm between the pulsed valve and the final beam collimation aperture as shown in Figure 2.1. The first chamber houses the pulsed solenoid valve and an electroformed nickel skimmer. A 1000 l/s turbo pump (Pfeifer, TMU 1000), backed by a 65 m^3/h mechanical pump, maintains the average pressure in the first chamber at about 5×10^{-4} mbar when the valve is operating at 20 Hz . The second and the third chambers, which provide for chopping and collimation of the molecular beam, are each evacuated by 500 L/s turbo pumps (Pfeifer, TMU 520) backed by dry membrane pumps. Typical pressures during operation of the valve are 4×10^{-6} and 9×10^{-8} mbar for the second and the third chambers, respectively. A manually operated isolation valve separates the second and the third pumping stage, so that the molecular beam source can be vented for servicing without breaking the vacuum in the UHV chamber.
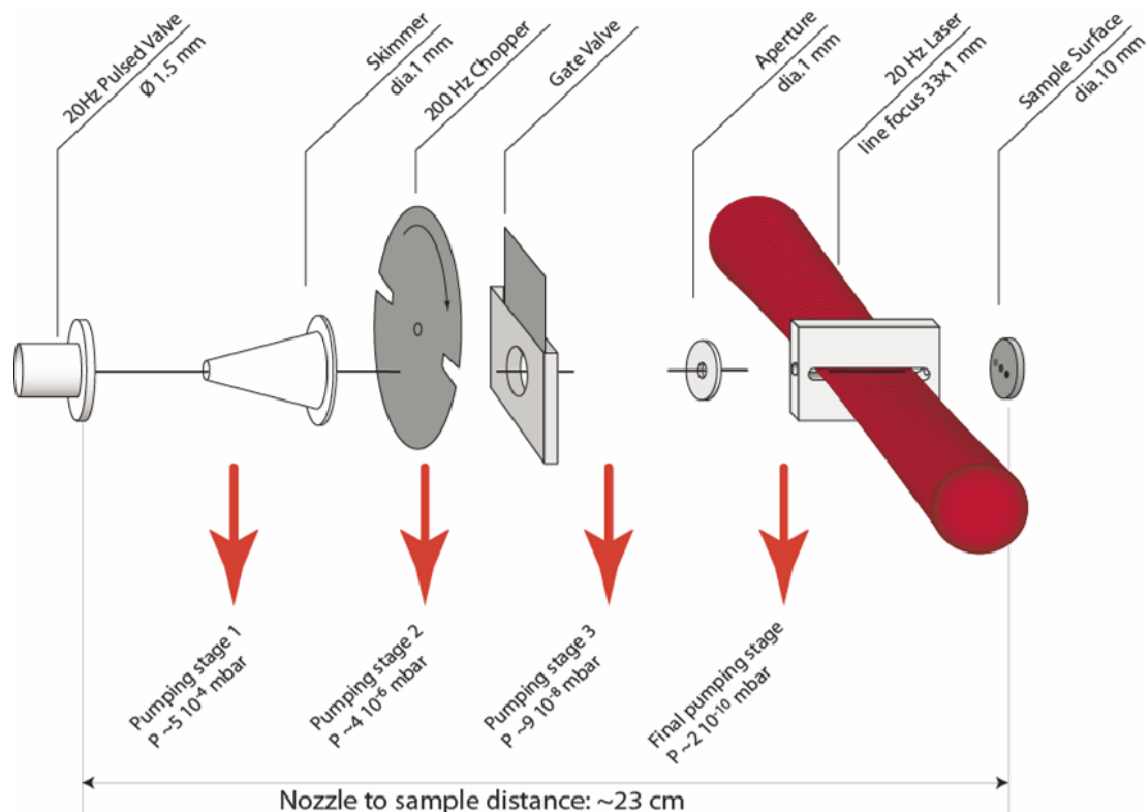
Figure 2.1 Schematic view of the molecular beam path[33]. A pulsed molecular beam is generated by expanding mixtures of methane through a temperature controlled solenoid valve with an open time of ~300 µsec. The beam pulses pass through a 1 mm diameter skimmer into the second differential pumping region where their duration is reduced to 30 µsec by a chopper wheel rotating at 200 Hz. After a further differential pumping stage, the beam pulses enter the UHV chamber through a 1 mm diameter aperture, traverse a laser beam alignment tool and impinge on a single crystal surface. The alignment tool serves to overlap the molecular beam with the laser beam, which is focused to a line by a cylindrical lens and crosses the molecular beam at 90°.

We use a solenoid valve with a large (1 mm) nozzle diameter to produce an intense supersonic expansion in the source chamber. The valve is mounted in a heater assembly and its temperature is measured by a thermocouple attached to the face plate. An electronic temperature controller (Omega) is used to maintain a stable valve temperature, typically, in the range of 373-473 K in order to prevent cluster formation and to control the molecular beam speed. At these low nozzle temperatures almost all the methane molecule are in the vibrational ground state, for this reason we consider our laser-off reactivity measurements a close upper limit to the ground state reactivity of methane.

We use Boltzmann statistics to calculate the fraction of methane molecules thermally excited to the fundamental vibrational modes as a function of the nozzle temperature:

$$\frac{n_i}{N} = \frac{g_i e^{-h\nu_i/kT}}{\sum_i q_i} ; \quad q_i = g_i e^{-h\nu_i/kT} \quad \textbf{(2.1)}$$

where $q = \sum_i q_i$ is the partition function (the sum is extended to all states up to 3060 cm^{-1}), g_i is the degeneracy, and ν_i is the frequency of the i-th vibrational state.

For the 323 K nozzle temperature used in the $E_n < 60$kJ/mol experiments, we get about 1% of the methane molecules in $v = 1$ of the ν_4 mode (see Table 2.1).

Table 2.1 Calculated fraction of thermally vibrationally excited CH$_4$ for the two nozzle temperatures applied in this work.The fractions of methane molecule in the $v = 1$ energy level of each vibrational mode are calculated from expression (2.1).

Mode	g_i	323K	373K
ν_1	1	3.6×10^{-6}	2.5×10^{-5}
ν_2	2	2.2×10^{-3}	5.4×10^{-3}
ν_3	3	4.2×10^{-6}	2.2×10^{-5}
ν_4	3	8.8×10^{-3}	1.9×10^{-2}

The valve is mounted on an x-y-z manipulator, which allows precise alignment of the valve position relative to the skimmer to maximize the gas throughput into the second pumping stage. The supersonic jet expansion, produced by the pulsed valve, is skimmed by an electroformed nickel skimmer (Beam Dynamic, model 1) with a 1 mm diameter aperture. To maximize the fraction of laser-excited molecules in the molecular beam pulse, we reduce the length of the molecular beam with a chopper wheel located in the second chamber. The 127 mm diameter chopper wheel rotates at 200 Hz driven by a water-cooled AC-synchronous motor (Globe 18A1003-2) and contains two pairs of opposing slits of 2 mm and 25 mm width. An optical trigger positioned at 180° from the molecular beam relative to the axis of rotation senses the passing of the chopper slits so that the solenoid valve can be synchronized with the help of a

delay generator to fire either through the small or through the large slit of the chopper wheel, resulting in molecular beam pulses of 26.6 μs or 334 μs, respectively. A controller drives the ac motor, senses the trigger signals, discriminates the long pulses from the short ones, and reduces the repetition rate of the trigger signal from 400 Hz to 20 Hz to coincide with the laser repetition rate.

The molecular beam enters the third chamber through the isolation valve. A replaceable 1 mm diameter aperture at the exit of the third chamber further collimates the beam as it enters the UHV chamber. Since the open time of the chopper wheel determines the duration of the pulse, the length of the gas pulses along the beam axis varies with the velocity of the molecules in the expansion. For the beam velocities in the range 700-3000 m/s and the open time ~30 μs of the small slit, we produce gas pulses with length between 2.1 and 9 cm. These pulses are sufficiently short to allow significant spatial overlap with a cylindrically focused laser beam perpendicular to the molecular beam axis. Since the fraction of molecules excited in the molecular beam depends on the ratio between the volume illuminated by the laser and the total volume of the molecular beam pulse, the production of short molecular beam pulses, which reduces the fraction of unexcited molecules hitting the surface, is critical to our experiments. If the gas pulses are too long and the fraction of excited molecules is small, the observed reactivity might be dominated by unexcited molecules.

To measure the velocity of our molecular beam, we use a quadrupole mass analyzer in combination with the chopper wheel for time-of-flight (TOF) measurements. For the TOF measurements, the sample surface is moved out of the molecular beam which then directly enters the ion source of a collinearly mounted quadrupole mass spectrometer. An aperture is inserted into the beam path in order to reduce the beam flux into the ion source of the mass spectrometer, which improves the time response by reducing pump out effects of the ion source. We record the arrival time distribution of the CH_4^+ ions (mass 16) using a multichannel scaler (Turbo-MCS, Ortec). For the analysis, we fit the measured time-of-flight data by a model function that is based on a flux-weighted Maxwell-Boltzmann distribution of velocities, convoluted with the experimentally determined chopper transmission function. For detailed description of our TOF measurement, see Plinio Maroni and Mathieu Schmid [6, 40].

2.3   Surface science chamber

Our custom-built UHV surface science chamber is pumped by a 1000 L/s turbo pump (Pfeiffer, TMU 1000P), backed by an oil free membrane pump (KNF N920, speed 1 m^3/h, base pressure < 1.5 mbar). The base pressure of UHV chamber after 48h bakeout at 120°C and several weeks of operation is 6×10^{-11} mbar.

The different components in the UHV chamber are arranged on three levels. The lowest level holds the vacuum gauges, a load lock for sample transfer without breaking vacuum in the main chamber, a fine focused ion gun for SIMS experiments (Omicron, ISE100) and a quadrupole mass analyzer with energy filter (Hiden, SIMS Probe) for detection in the SIMS measurements. The molecular beam enters the UHV chamber on the central level; this level also contains an on-axis quadrupole mass spectrometer (Hiden Analytical, HAL/3F RC 301) for TOF measurements and beam intensity monitoring. The top level holds the surface preparation and analysis tools: a sputter ion gun (Omicron, ISE10) for surface cleaning, a cylindrical mirror analyzer Auger system (Omicron, CMA 150) for surface composition analysis, and a reverse view LEED optics (Omicron, SPECTALEED) for surface structure determination.

The sample surface is mounted on a commercial four axis manipulator (Thermionics), providing translational motion along the vertical Z axis (400 mm travel, 12.7 μm resolution), X and Y displacements in the horizontal plane with ± 20 mm travel and 2.5 μm resolution. The manipulator includes rotation about the Z axis for control of the incident angle of the molecular beam as well as the orientation of the sample in front of the surface analysis tools. The X-axis and the Z-axis micrometer drives of the manipulator are equipped with stepper motors for automated motion of the sample via computer control.

The platinum crystal is mounted on a removable sample holder (platen) that attaches to the copper dewar-heater assembly of the manipulator. The platen can be transferred under vacuum from the UHV chamber into a load lock with a magnetically coupled rotary linear actuator. The sample temperature is measured with a K-type thermocouple spot-welded to the edge of the crystal. The sample is heated by electron impact from the back and cooled by heat conduction to the liquid nitrogen cooled dewar. The heating system is commercially available (Thermionics, STLC-TTC platen) and includes the power supply (SPS series) and the PID controller (Omron,

E5AK). For electron impact heating of the sample, a bias voltage up to 2000V can be applied to a filament located at the back of the grounded sample.

2.3.1 Surface preparation

We clean our samples by bombardment with energetic Ar^+ ions generated by a commercial ion gun (Omicron, ISE 10). We use high purity argon (PanGas, 99.999% pure) to generate a broad ion beam of 2-3 cm diameter at the sample position. We sputter the surface with a total current leaving the gun of 20 µA and an acceleration voltage of 1 kV. The partial pressure of Ar in the deposition chamber rises to 5×10^{-7} mbar during sputtering. We measured the current on the 19 mm sample platen to be 2 µA [40], this corresponds to an incident ion dose of 2.6×10^{14} ions/cm^2/min. Since we normally sputter the surface from 10 to 15 minutes we can calculate, knowing that the sputter yield of Pt is 1.542 (with 1 kV Ar^+ ions)[42], that we remove from 1.7 to 2.6 Pt ML from a Pt(111) surface.

After this preparation, we check the cleanliness and the structure of the surface by Auger and LEED measurements. The Auger spectrum shows that the surface prepared in this way is free, up to the Auger detection limit (1.6% ML of carbon on the surface), from contaminations (Figure 2.2) and a sharp pattern is obtained by LEED (Figure 2.3).
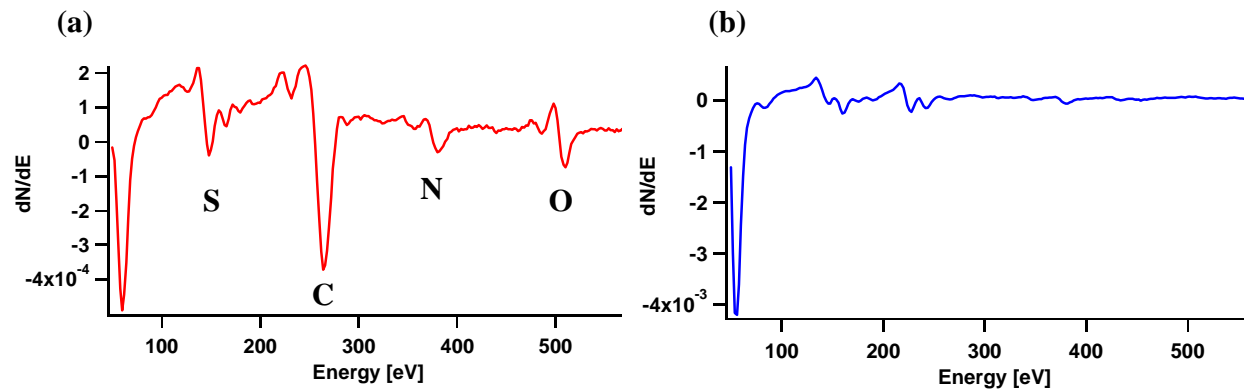
Figure 2.2 (a) Auger spectrum of the Pt(111) surface as introduced in the UHV chamber; **(b)** AES of the Pt(111) surface after a cycle of argon sputtering and annealing to 1200 K.

19
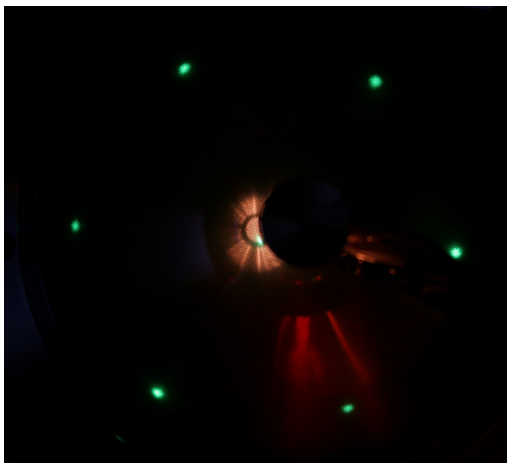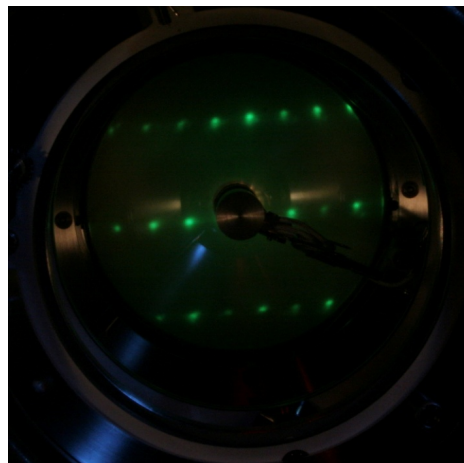
Figure 2.3 (a) regular hexagonal LEED pattern of the clean Pt(111) surface; **(b)** LEED pattern of the clean Pt(110) (1×2) surface.

2.3.2 King and Wells beam reflectivity measurements

In the King and Wells technique [43] (Figure 2.4) for measuring sticking coefficients via molecular beam scattering, an inert mica beam-flag in the UHV chamber is inserted into the molecular beam to block it from reaching the sample surface. The molecular beam is scattered by the inert flag and produces a pressure rise in the UHV chamber (P_0). A QMS monitors the partial pressure of the species of interest in the UHV chamber as a function of time. At t_0, the flag is opened and the molecular beam impinges an initially clean surface. Due to adsorption of the molecules, the crystal surface acts as a pump and a drop (ΔP) in the QMS signal is observed. The initial sticking coefficient can be determined by:

$$S_0 = \frac{P}{P_0} \qquad \textbf{(2.2)}$$

The advantage of this technique is that it directly gives the absolute sticking coefficient as the ratio of two partial pressure measurements without the need of calibration of the molecular beam flux or quantitative detection of adsorbate coverage on the surface. A disadvantage of the King&Wells method, as implemented in our setup, is the fact that sticking coefficients much below 1% cannot be detected due to limited signal-to-noise ratio of the QMS measurement. Since most of the sticking coefficients determined in this thesis are well below 1%, the more sensitive AES detection of the carbon reaction products (described below) is used for relative reactivity measurements. The AES measurements are then calibrated in absolute terms by comparison to King and Wells (K&W) measurements at high incident kinetic energy where the reactivity reaches or exceeds 1% [44] rather than using a carbon uptake curve to a known saturation coverage as done for the Ni(111) surface [39]. The reason for using a different calibration procedure stems from the fact that C on Pt(111) and Pt(110) can adsorb either in a carbidic or a graphitic phase with different saturation coverages [45, 46]. Now I will describe this calibration for reactivity measurements on the Pt(111) surface. For Pt(110)-(1×2), we have used the same procedure.
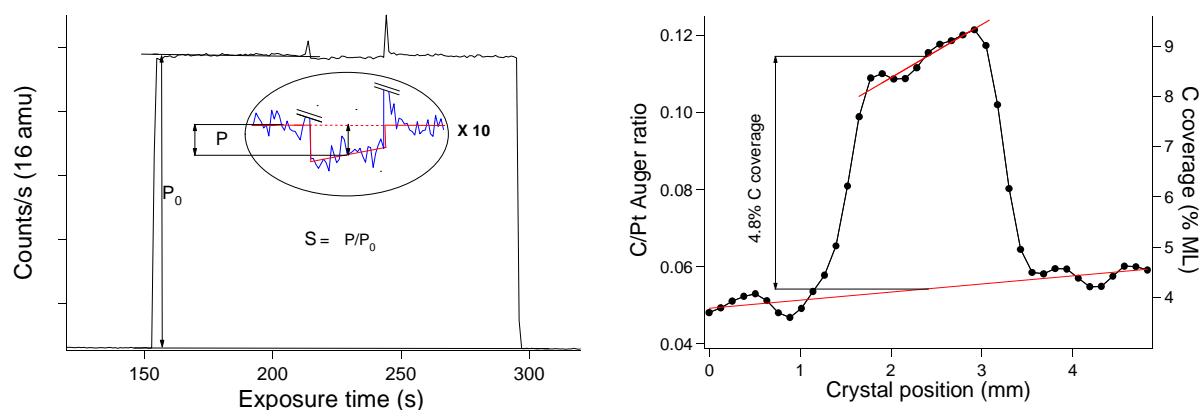
Figure 2.4 (a) Example of a King & Wells measurement of the CH_4 sticking coefficient on Pt(111) averaged over a 30 seconds deposition. Repeated measurements give an averaged sticking coefficient S = (0.98±0.16) $\times$ 10^{-2} which is used to calibrate the reactivity measurement via Auger detection of absorbed carbon. **(b)** AES analysis of carbon coverage resulting from a 30 seconds exposure under identical condition as in Figure 2.4 a. The C/Pt AES ratio is calculated from C(272 eV) and Pt(237 eV) Auger signals (average of 7 points around the peak center, with baseline subtraction). The change in the C/Pt AES ratio is related to a change in carbon coverage (in %ML), using the averaged K&W sticking coefficient and the calibrated exposure flux[47].

21

The limited sensitivity of the K&W method allows for sticking coefficient measurements above 5×10^{-3} in our setup. We therefore use a CH_4 beam at high kinetic energy (64 kJ/mol) and high nozzle temperature (473 K) to perform the Auger calibration. Under these conditions, we measure the sticking coefficient of CH_4 on a clean Pt(111) surface averaged over a 30 second deposition to be S = (0.98±0.16) × 10^{-2} with an estimated uncertainty obtained by repeated measurements (95% confidence). The relative uncertainty of 16% is included in all reactivity measurements using the calibrated C/Pt AES signals. Auger analysis of the carbon "spot" resulting from the same CH_4 molecular beam dose of the clean Pt(111) surface yields a C(272 eV)/Pt(237 eV) AES signal ratio of 0.062 (Figure 2.4 b). During the exposure, the incident CH_4 dose was monitored by a calibrated[40] mass spectrometer to be 4.9 ML in terms of Pt atom surface density (1.50×10^{15} cm^{-2} on Pt(111)). We use the sticking coefficient from the K&W measurement along with the measured flux to calibrate the C/Pt AES signal ratio in terms of Carbon coverage, i.e. $0.98 \times 10^{-2} \times 4.9$ ML = 0.048 ML for a C/Pt AES signal of 0.062.

Once calibrated, we use AES detection of C on Pt(111) to quantify the sticking coefficient in the range of incident energy of 10-64 kJ/mol with lower nozzle temperature (323 K and 373 K) for both laser-off and laser-on reactivity measurements. Even though the calculated $2\nu_3$ state-resolved sticking coefficients are well above the detection limit of the K&W technique, the low fraction of laser excited CH_4 in the molecular beam prevents the use of the K&W method for calibration of the laser-on sticking coefficients since our laser-on measurements probe the average sticking coefficient of all CH_4 molecules contained in the beam (excited and unexcited).

We calculate the initial sticking coefficients S_0, from the measured C/Pt AES signal ratios of typically 0.05-0.1 (corresponding to 4-8% ML coverage) detected at the end of a deposition experiment. In the calculation of S_0, we correct for the nonlinearity in carbon uptake using experimentally determined uptake curve for carbon on Pt(111) and Pt(110), produced by methane molecular beam exposure (Figure 2.5 and 2.6). We fit the uptake curves using a first-order Langmuir model:

$$\theta_C = 1 - A \times \exp(-B \times F)) \quad \textbf{(2.3)}$$

where θ_C is the carbon coverage, A = 1 ML is the saturation coverage of carbon on platinum, B (1/ML) is a fitting parameter and F is the methane exposure expressed in ML. Finally, from the derivative of the uptake curve we obtain the sticking coefficient $S(\theta_C)$ of methane on platinum as a function of the carbon coverage.
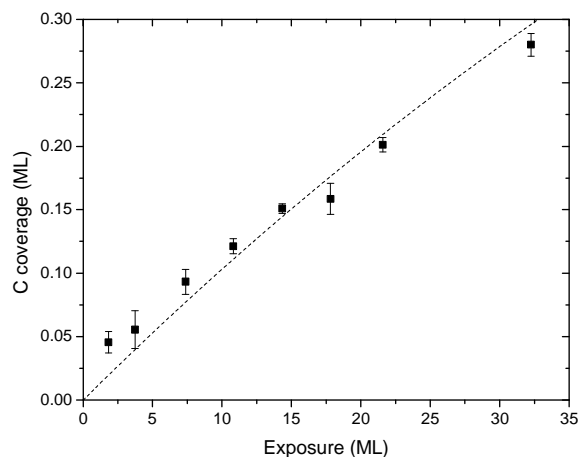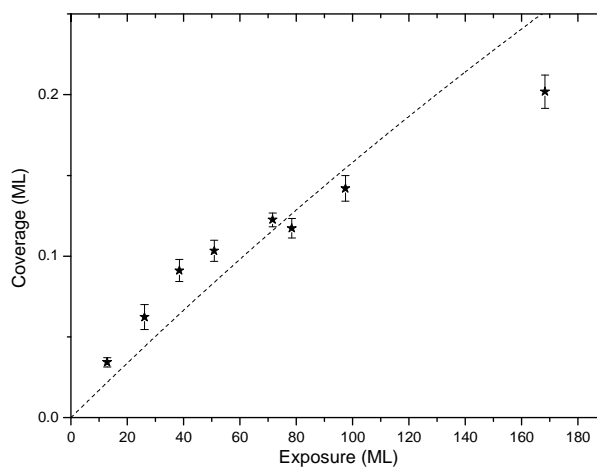

Figure 2.5 Carbon coverage as a function of the exposure for methane adsorption on Pt(111) at T_s = 600 K, E_t = 64 kJ/mol, T_n = 373 K. The dashed line corresponds to a first-order Langmuir fit to the experimental data.

Figure 2.6 Carbon coverage as a function of the exposure for methane adsorption on Pt(110-(1×2) at T_s = 400 K, E_t = 54 kJ/mol, T_n = 323 K. The dashed line corresponds to a first-order Langmuir fit to the experimental data.

23

2.4 Pulsed infrared laser and Cavity Ring-Down setup

The pulsed IR laser setup used in this experiment is shown in Figure 2.7.
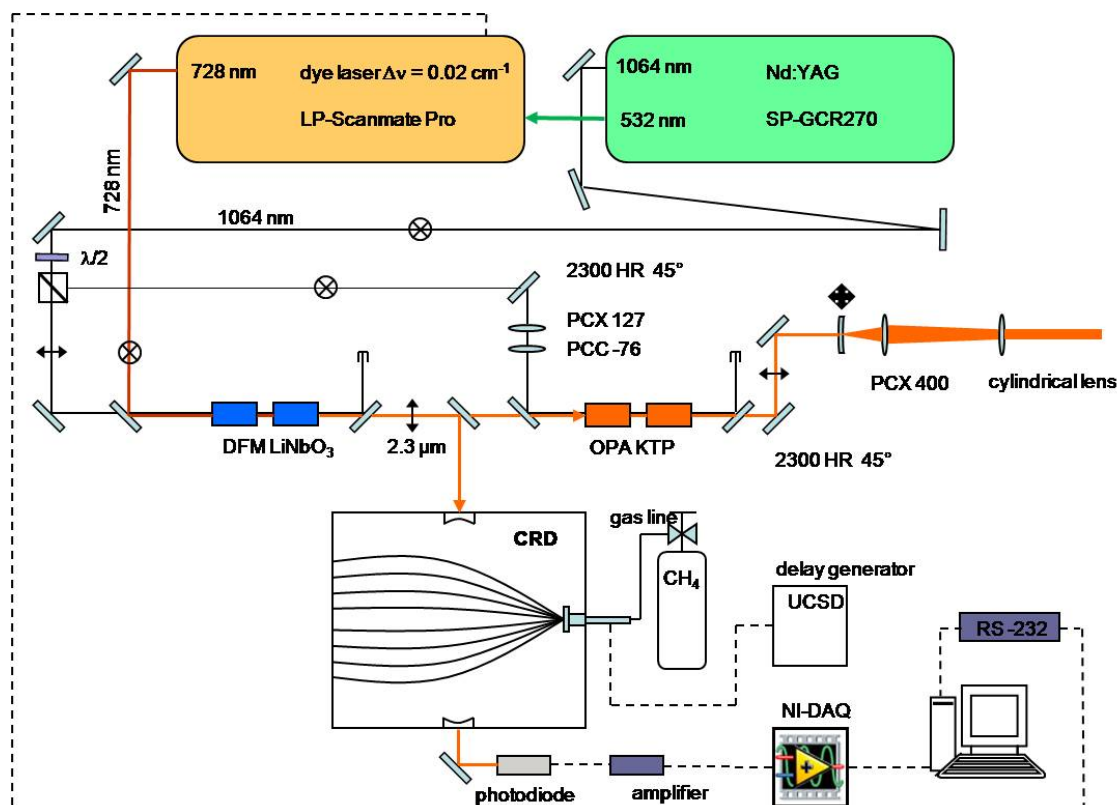
Figure 2.7 Laser setup used for the vibrational excitation of methane in the near-infrared octad region of methane (4200-4300 cm^{-1}).

The second harmonic of an injection-seeded single-mode Nd:YAG laser (Spectra Physics, GRC270, maximum output > 400 mJ/pulse at 532 nm, 8 ns pulse duration) is used to pump a tunable, narrow bandwidth (0.02 cm^{-1}) dye laser with intra-cavity etalon (Lambda Physik, ScanmatePro). The dye laser produces ~50 mJ pulses of vertically polarized output tunable in the range of 720 – 750 nm when operated with LDS 750. The 1064 nm Nd:YAG fundamental is split in two variable intensity beams by a combination of a half-waveplate and a polarizing beam splitter cube. The horizontal polarization part of the Nd:YAG fundamental is used to

perform difference frequency generation (DFG) with the output of the dye laser in a LiNbO$_3$ crystal (Castech) to produce 2-3 mJ of IR radiation, tunable in the vicinity of 2.3 μm. The crystal is installed in a commercial angle-tracking system (Inrad, AutoTracker II), allowing for continuous tracking of the IR radiation. After the DFG stage, the residual 1064 mn and ~730 nm are separated from the 2.3 μm by reflection with a dielectric mirror and a Germanium plate, respectively. 30% of the 2.3 μm output is directed to a cavity ring-down setup for acquiring jet absorption spectra and for tuning the laser in resonance with the desired molecular transition. The remaining 70% IR radiation at 2.3 μm is amplified in an optical parametric amplifier (OPA) system.

In the OPA, the 1064 nm vertically polarized beam reflected by the beam splitter is used as pump for the OPA stage. In order to increase the fluence on the KTP crystals, the pump beam diameter is reduced by a telescope. The OPA system consists of two 25 mm long KTiOPO$_4$ (KTP) crystals cut at $\theta = 54°$, $\phi = 0°$ and arranged in a walk-off compensated configuration [48]. The temperature of the crystals is stabilized to 40.0±0.1°C by two temperature controlled ovens. The KTP crystals are used in the oeo configuration, meaning that the pump beam(1064 nm) and the idler (1979 nm) beam have ordinary polarization (s-polarized with respect to plane of incidence and reflection), and the signal beam (2300 nm) has extraordinary polarization (p-polarized) [49]. To achieve the proper polarization directions, the KTP crystals are rotated about a vertical axis as shown in Figure 2.8.
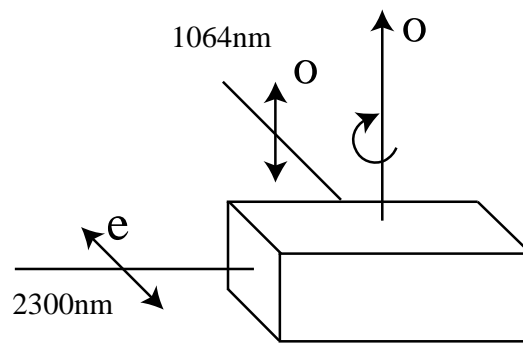
Figure 2.8 Light polarization direction and crystal rotation direction of our OPA system [41].

After the OPA stage, the 1064 nm pump radiation and the idler beam are separated from the amplified signal beam by two dichroic mirrors. By pumping the OPA with 500 mJ/pulse at 1064 nm, we can produce IR pulses at 2.3 μm with an energy of 100 mJ/pulse. The 2.3 μm beam is expanded by a telescope to a diameter of 40 mm, and a cylindrical lens with a focal length of 120 cm focuses the tunable IR beam to a line inside the UHV chamber where it is carefully overlapped with the molecular beam. An IR-sensitive video camera and an alignment tool installed on the molecular beam axis are used to center the IR beam in the molecular beam. The width and length of the line focus are measured by deflecting the IR beam before a deposition experiment and burning a piece of photosensitive paper at the correct lens-molecular beam distance. During the deposition experiment, the IR power transmitted through the alignment tool/instrument is monitored by a laser power meter. Simultaneously, we monitor the cavity ring-down time in a separate chamber to verify that the laser stays on resonance with the molecular transition throughout the deposition. A delay generator is used to synchronize the IR laser pulses with the molecular beam pulses in time.

To quantify our state-resolved sticking coefficients measurements, we need to determine the fraction of excited molecules, which depends on the population of the initial state of the pumped transition and the laser fluence (mJ/cm^2) crossing the molecular beam. To measure the rotational populations for a molecular beam of a specific mixture, we used the CRD setup to record rotationally resolved absorption spectra in a jet expansion that reproduces the expansion condition of our molecular beam source. The population of the initial state is determined by analyzing Q branch transitions intensities in the obtained ro-vibrational spectra. An example of a jet-cooled CRD spectrum of CH_4 and the calculation of initial state population will be presented in the following sections of this chapter.

The cavity ring-down vacuum chamber (base pressure 7×10^{-8} mbar), evacuated by a 2000 l/s diffusion pump (Balzers, DIF 200) and a mechanical forepump (Balzers, Duo35), is equipped with the same temperature-controlled solenoid valve as installed in the molecular beam source. A 85 cm long cavity is formed by two high reflective plano-concave mirrors with a radius of curvature r = 1 m. The longitudinal and transverse mode spacing of the cavity are 170 Mhz and 80 MHz, respectively. 30% of the DFG output at 2.3 μm (8 ns, 0.02 cm^{-1} FWHM) is directed towards the cavity and the transmitted intensity is measured as a function of time by a fast

InGaAs photodiode (Hamamatsu, G8373-01). The time-dependent transmitted intensity follows an exponential decay with ring-down time constant τ given by [50]:

$$\tau = \frac{d}{c(1-R+\sigma nl)} \qquad \textbf{(2.4)}$$

where d is the cavity length, c is the speed of light, σ is the adsorption cross section of the sample molecules, n is their number density, l is the length of the sample and R is the reflectivity of the mirrors. When the cavity is empty, the decay time is dominated by finite reflectivity of the mirrors. If an absorbing sample is introduced in the cavity, an additional loss arises and the ring-down time decreases. CRD spectra are obtained by monitoring the ring-down time as a function of laser frequency. Practically, the photodiode signal is recorded as a function of the laser frequency by a Labview program (see Appendix B) via a fast (10 Msample/sec) data acquisition card (National Instrument) and 20 traces are averaged to improve the signal to noise ratio. The ring-down time is then determined by fitting the averaged photodiode signals with an exponential decay function. With an empty cavity, we observed a ring-down time of about 40 μs, which corresponds to an effective reflectivity of 99.989%. The Labview program also allows us to stop a scan and hold the laser at a desired frequency while monitoring the ringdown time during deposition experiments with a laser excited molecular beam.

2.5 Methane Spectroscopy

2.5.1 Assignment of the $2\nu_3$, $\nu_1+\nu_4$ and $2\nu_2+\nu_4$ bands

The CH_4 molecule belongs to the tetrahedral point group T_d (see the character table in Appendix A) and has $(3N - 6) = 9$ internal degrees of freedom that can be described as four normal mode of vibrations (Figure 2.9): the symmetric C-H stretch ν_1, the symmetric bending vibration ν_2, the infrared active antisymmetric C-H stretch ν_3, and the infrared active bending vibration ν_4. The frequency, symmetry and degeneracy of the fundamental vibrational modes are summarized in Table 2.2.

Table 2.2 Energy (cm^{-1}), symmetry and degeneracy of the fundamental vibrational modes of methane.

Mode	Energy (cm^{-1})	Symmetry	Degeneracy
ν_1	2914.2	A_1	1
ν_2	1523.8	E	2
ν_3	3020.3	F_2	3
ν_4	1306.2	F_2	3

Because the frequency of the two stretching vibrations is approximately twice the frequency of the bending vibrations, the vibrational states are coupled by anharmonic stretch-bend resonances (Fermi resonance) and the vibrational eigenstates can be grouped into polyads of interacting states separated by ~1500 cm^{-1}. These polyads are commonly numbered by a polyad number $N = 2(\nu_1+\nu_3) + \nu_2 + \nu_4$, (some authors adopt different schemes) so that the (ν_2, ν_4) dyad is labeled with $N = 1$, the pentad (ν_1, ν_3, $2\nu_2$, $2\nu_4$, $\nu_2+\nu_4$) has $N = 2$, the following octad has $N = 3$, and so forth. Only the vibrational states of F_2 symmetry have allowed electric dipole transitions from the ground state and are infrared-active. These include the fundamentals of ν_3 stretching and ν_4 bending modes as well as their overtone and combination bands. The assignment of the fundamental [51-53], and overtone [54, 55] bands of ν_3 are known and the transition frequencies are tabulated for example in the HITRAN database[56]. In our state-

resolved reactivity measurements for methane, we identify specific ro-vibrational transitions by recording CRD spectra in the near infrared region of the octad band of CH_4 (3900 – 4400 cm^{-1}) and in the $2\nu_3$ region (~ 6000 cm^{-1}) and by comparison of the positions and relative intensities of the experimental peaks with the transition reported in the HITRAN [56] and in the STDS (*Spherical Top Data System*) [57] spectroscopic databases. In my experiments, I use the R(1) transition at 6004.69 cm^{-1} to prepare methane in the J = 2 rotational state of the $2\nu_3$ vibrational band, which belongs to the 14 vibrational bands of the N = 4 tetradecad. The widely used label $2\nu_3$ for this state is due to the largest normal mode contribution when the wavefunction is written in a normal mode basis. Calculations by Wang *et al.* [58] on the vibrational states of CH_4 up to 9000 cm^{-1} obtained the leading coefficients for the 6004.69 cm^{-1} state as 73% $2\nu_3$ and 15% $\nu_1+\nu_3$.
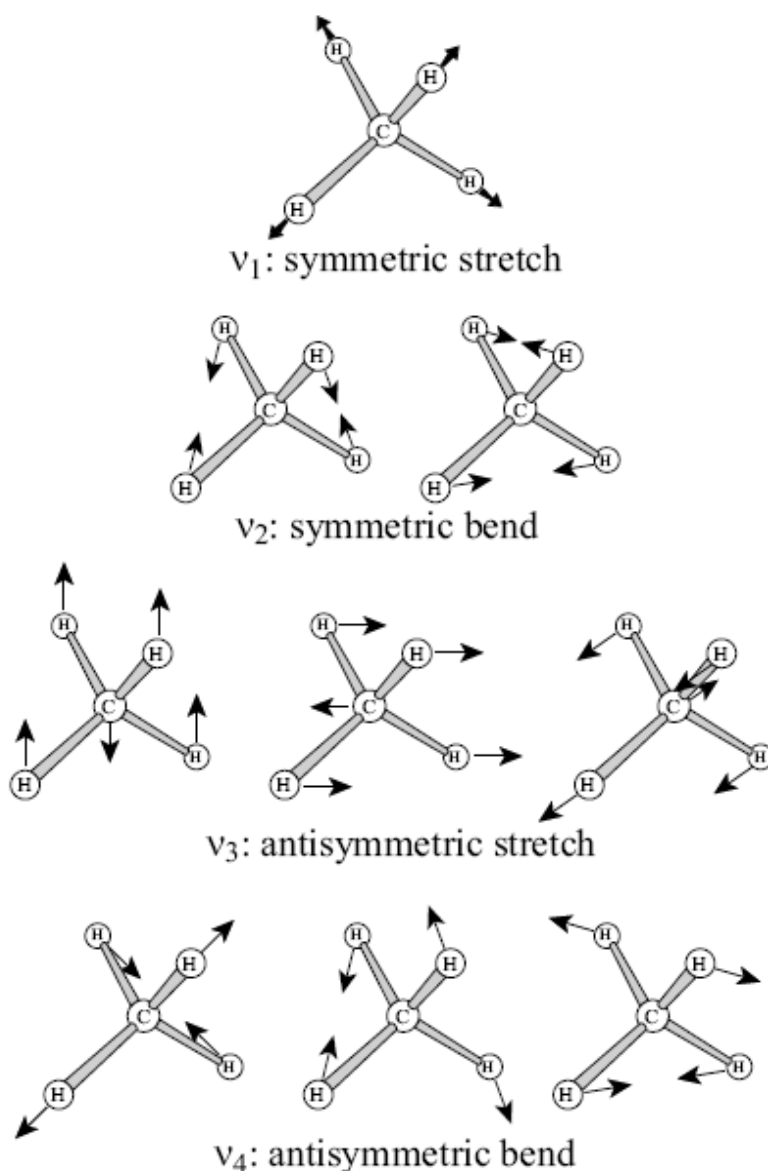
Figure 2.9 Representation of the CH_4 normal modes[6].

The two other states investigated in this work, $2\nu_2+\nu_4$ and $\nu_1+\nu_4$, belong to the $N = 3$ polyad which is comprised of 8 members (octad) in the range of 3900 -4400 cm^{-1}. Due to the congestion of the rovibrational states in this spectroscopic region (see Figure 2.10) the transitions of the octad system of $^{12}CH_4$ and his isotopomers have been only recently completely assigned by Hilico and coworkers[59]. Figure 2.11 shows CRD spectra of jet-cooled CH_4 in the $\nu_1+\nu_4$ and $2\nu_2+\nu_4$ band region. The band origins for transitions leading to the octad states with their normal

mode labels are reported in Table 2.3. In fact, Wang *et. al.* [58], showed that the states labeled $\nu_1+\nu_4$ and $2\nu_2+\nu_4$ contain respectively 93% of $\nu_1+\nu_4$ and 2% of $3\nu_4$ and 99% of $2\nu_2+\nu_4$ and 1% of $\nu_1+\nu_4$. Therefore, the labels R(1) $\nu_1+\nu_4$ and R(1) $2\nu_2+\nu_4$ are well adapted to describe the CH_4 rovibrational transitions that we have excited in this work.
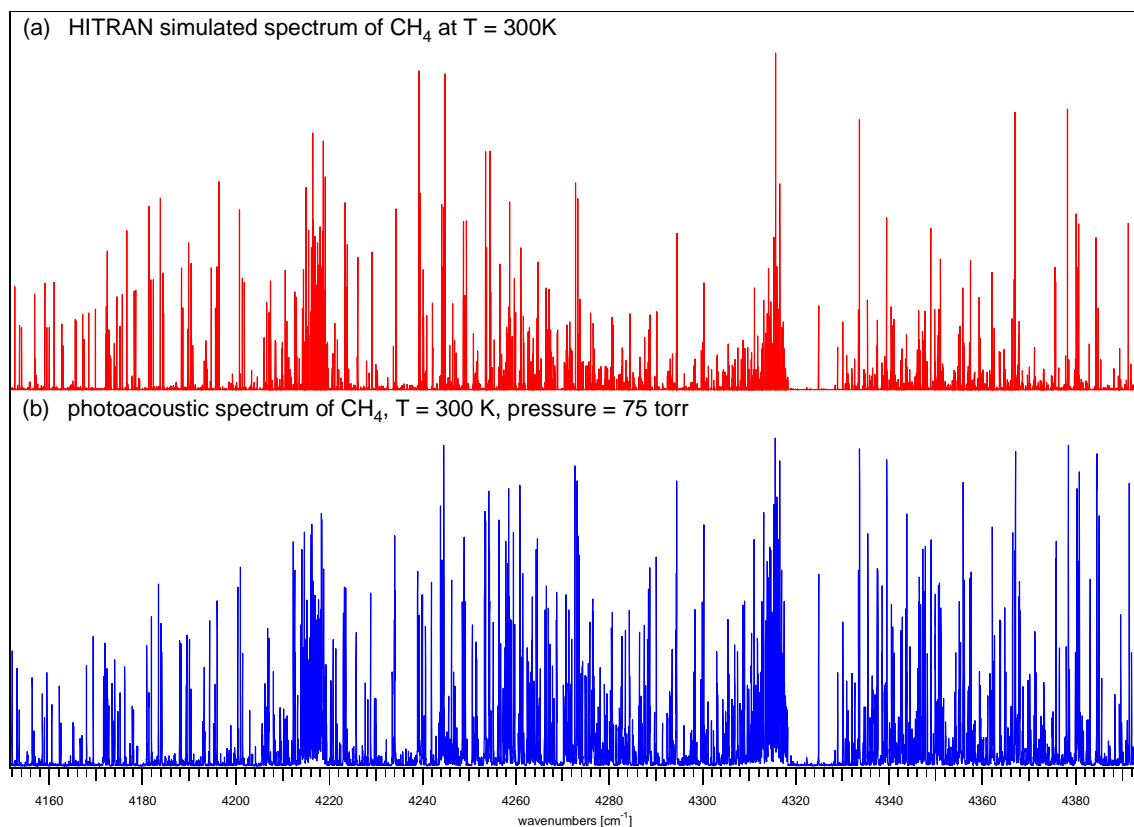
Figure 2.10 (a) HITRAN simulated spectrum of $^{12}CH_4$ in the 4150 – 4400 cm^{-1} region of the octad system. (b) Photoacoustic spectrum of methane (P = 75 torr, T = 300 K) in the same spectral region. The differences in the relative intensity of the lines between the simulated spectrum and the photoacoustic spectrum may be due to possible saturation of the transitions.
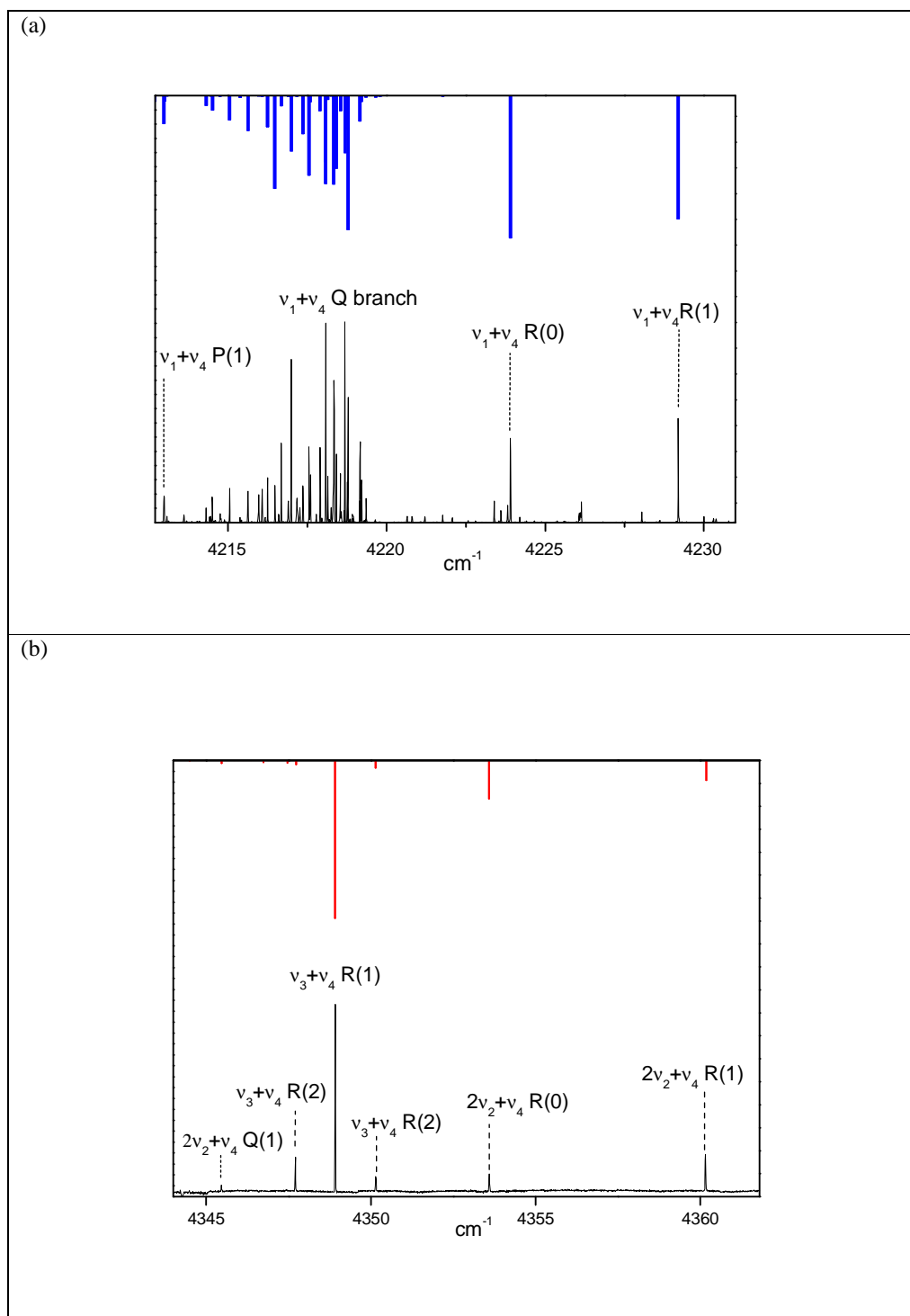
Figure 2.11 CRD spectra of jet-cooled CH_4 in the 4220 cm^{-1} and 4350 cm^{-1} regions. (a) Q and R branch of the $\nu_1 + \nu_4$ band; (b) R branch of the $2\nu_2 + \nu_4$ band . In this work we excite the R(1) ro-vibrational transition of the $\nu_1 + \nu_4$ and $2\nu_2 + \nu_4$ band, which populates a level with rotational angular momentum quantum number J=2.

32

Table 2.3 Summary of the octad system of methane as reported by Hilico *et al.*[60]

Band	Subband symmetry	Band Origin (cm^{-1})
$\nu_1 + \nu_2$	E	4435.1207
$\nu_1 + \nu_4$	F_2	4223.4615
$\nu_2 + \nu_3$	F_1	4537.5505
	F_2	4543.7630
$\nu_3 + \nu_4$	A_1	4322.6890
	E	4322.1978
	F_1	4322.5768
	F_2	4319.2107
$3\nu_2$	A_1	4595.4597
	A_2	4595.2799
	E	4592.0088
$3\nu_4$	A_1	3909.1898
	F_1	3920.5235
	F_2	3870.4870
	F_2	3930.9210
$2\nu_2 + \nu_4$	F_1	4363.5917
	F_2	4348.7078
	F_2	4378.9774
$\nu_2 + 2\nu_4$	A_1	4133.0236
	A_2	4161.9081
	E	4104.6175
	E	4151.0043
	F_2	4128.7283
	F_2	4142.8629

2.5.2 Determination of the CH_4 rotational level population

In this section, we describe our experimental determination of the population of rotational states arising from rotational cooling in a supersonic expansion, as determined by cavity ringdown spectroscopy. Because nuclear spin states do not interconvert in a supersonic expansion [6, 40, 41, 61] the rotational populations of three different spin species (ortho, para, meta I=0, 1, and 2) relax within the stack of rotational levels corresponding to their own spin species.

The molecular wave function ψ can be expressed as a linear combination of the electronic ψ_e, vibrational ψ_v, rotational ψ_r and nuclear spin ψ_{ns} wave functions:

$$\psi = \psi_e \cdot \psi_v \cdot \psi_r \cdot \psi_{ns} \qquad (2.5)$$

Since we are concerned with the electronic and vibrational ground states ($\Gamma(\psi_e) \otimes \Gamma(\psi_v) = A_1$), only the symmetries of the rotational wave functions and the spin states have to be considered. For molecules belonging to the T_d group, Hippler *et al*[62]. report the frequency of occurrence G of the symmetry species for a given J:

$$G(J,A,\rho) = \frac{1}{24}(2J+1+3(-1)^J+(-1)^{\rho+J}(6+g_1(J))+g_2(J)),$$

$$G(J,E,\rho) = \frac{1}{24}(4J+2+6(-1)^J-g_2(J)), \qquad (2.2)$$

$$G(J,F,\rho) = \frac{1}{24}(6J+3-3(-1)^J+(-1)^{\rho+J}(6-g_1(J)))$$

where:

$$g_1(J) = 6(-1)^J\left[\text{Sin}\left(\frac{1}{2}J\pi\right)+\text{Cos}\left(\frac{1}{2}J\pi\right)\right],$$

$$g_2(J) = 8\left[3^{-1/2}\text{Sin}\left(\frac{2}{3}J\pi\right)+\text{Cos}\left(\frac{2}{3}J\pi\right)\right],$$

$\rho = 1$ for A_2 or F_1, and $\rho = 2$ for A_1 or F_2.

For a correct interpretation of the transition intensities, we have to consider the statistical weights of the starting levels of the transition we excite. I have already considered the degeneracy of the rotational levels $(G(J,\Gamma,\rho))$, now I will show how we have calculated the nuclear-spin statistic weight. The four hydrogen nuclear spins $(I = 1/2)$ of methane generate a set of $2^4 = 16$ spin states, and depending on the total spin momentum I $(I = 0, 1, 2)$,we can have three methane spin-isomers: para-methane (E) is a nuclear singlet with $I = 0$; ortho-methane (species F) has a total nuclear spin $I = 1$ and a degeneracy of 3 (nuclear spin triplet) and meta-methane (species A) has a total spin $I = 2$ and a degeneracy of $2I + 1 = 5$ (quintet).

The nuclear spin weight for the allowed state is determined by multiplying the symmetry representation of the rotational wave function with that of the nuclear spin isomers. Using the irreducible representations of the T_d point group (Appendix A), we can observe that the nuclear spin weights for the rotational wave functions are $g_I = 5$ for the A_1 and A_2 rotational levels, $g_I = 2$ for the E rotational levels and $g_I = 3$ for the F_1 and F_2 rotational levels. These results show that the rotational state with $J = 0$ (A_1 symmetry) is allowed only for meta isomer, $J = 1$ (F_1 symmetry) for the ortho isomer, and $J = 2$ (E $+F_1$ symmetries) is populated by both ortho and para isomers.

In order to calculate the rotational populations in the methane molecular beam, we assume that during the cooling process in a supersonic expansion, spin species do not inter-convert[6, 40, 41]. In the case of CH_4, we can consider the 3 different spin species as if they were different species that cool down during the expansion with 3 different sets of rotational levels.

In general a rotational state J can be populated by different spin species, e.g. the rotational state J = 2 is populated by the ortho- and para-methane spin isomers. Therefore, the fractional population of the rotational level J at a given temperature T, in a jet expansion, will be given by the sum of the fractional populations of each spin species contained in the rotational state J. This can be expressed with the following equation:

$$p(J, T) = \chi_{meta} \sum_{\Gamma_{meta}=A_1,A_2} G(J,\Gamma_{meta})g_I(\Gamma_{meta})(2J+1)\exp\left(\frac{E(J,\Gamma_{meta})}{kT}\right)/Q_{meta}(T)$$

$$+\chi_{para} G(J,E)g_I(E)(2J+1)\exp\left(\frac{E(J,\Gamma_{meta})}{kT}\right)/Q_{para}(T) \qquad (2.6)$$

$$\chi_{ortho} \sum_{\Gamma_{ortho}=F_1,F_2} G(J,\Gamma_{ortho})g_I(\Gamma_{ortho})(2J+1)\exp\left(\frac{E(J,\Gamma_{ortho})}{kT}\right)/Q_{ortho}(T)$$

where G(J, Γ) is the frequency of occurrence of the irreducible representation Γ in the rotational level J (see equation 2.2), (*J*, Γ) is the energy of the state (*J*, Γ) , $Q_{meta}(T)$, $Q_{para}(T)$ and $Q_{ortho}(T)$ are the rotational partition functions at temperature T of the spin species *meta*, *para*, and *ortho*, respectively. χ_{meta}, χ_{para} and χ_{ortho} indicate the high-temperature limit molar fractions of the spin species. At room temperature, the number of populated rotational states is sufficiently large that the average density of occupied states of a given spin species corresponds to the sum of the dimensions for all the levels giving rise to a particular spin isomer.

For the meta-methane: [A₁] + [A₂] = 2, for para-methane: [E] = 2, and for ortho-methane: [F₁] + [F₂] = 6. The molar fraction of different spin species at room temperature is given by the product of the nuclear spin weight g_I with the density of occupied state for each species:

$\chi_{meta} = 5/16,$

$\chi_{para} = 2/16,$ **(2.7)**

$\chi_{ortho} = 9/16.$

Q_{meta}, Q_{para} and Q_{ortho} are the rotational partition functions for the different spin isomers and can be written as:

$$Q_{meta}(T) = \sum_J \sum_{\Gamma_{meta}=A_1,A_2} G(J,\Gamma_{meta})g_I(\Gamma_{meta})(2J+1)\exp\left(-\frac{E(J,\Gamma_{meta})}{kT}\right),$$

$$Q_{para}(T) = \sum_J G(J,E)g_I(E)(2J+1)\exp\left(-\frac{E(J,E)}{kT}\right), \qquad (2.8)$$

$$Q_{ortho}(T) = \sum_J \sum_{\Gamma_{meta}=F_1,F_2} G(J,\Gamma_{ortho})g_I(\Gamma_{ortho})(2J+1)\exp\left(-\frac{E(J,\Gamma_{ortho})}{kT}\right)$$

The energies of the rotational levels are given by:

$$E\,(J) = B_i\,J\,(J+1) - D_i\,J^2\,(J+1)^2 \qquad \textbf{(2.9)}$$

where B_i is the rotational constant of the i-th vibrational state. Equation 2.6 includes the centrifugal distortion effects, D_i the centrifugal constant corresponding to the vibrational state i. The fractional populations of the J = 0, 1, and 2 rotational levels are shown as a function of the rotational temperature in Figure 2.11.
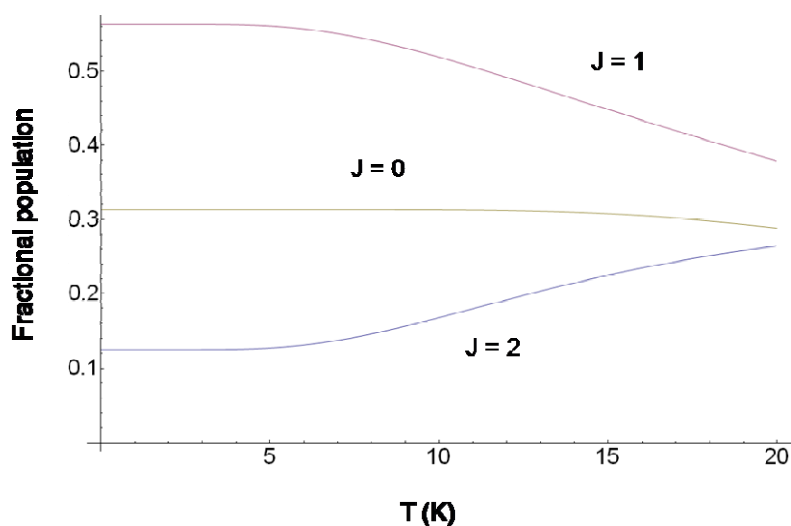
Figure 2.12 Fractional populations of the J = 0, 1, and 2 rotational levels as a function of the rotational temperature after a supersonic expansion.

We determine the initial population in the molecular beam from the Q branch transitions in the CRD spectrum of CH_4. (an example is shown in Figure 2.13).
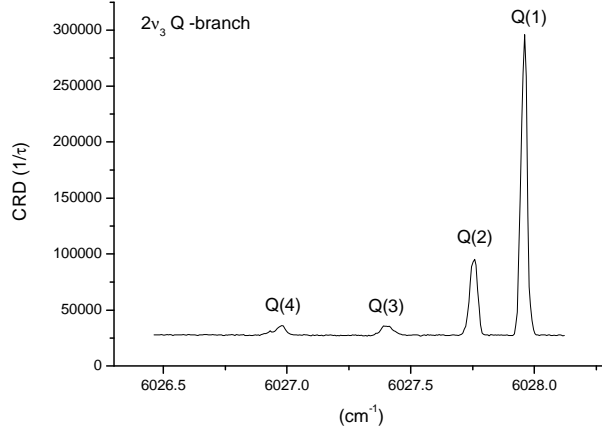
Figure 2.13 CRD spectra of a jet-cooled 25% CH_4 in H_2 mixture ($T_n = 300$ K) in the Q branch region of the $2\nu_3$ vibrational state. Comparing the intensities of the rovibrational transitions Q(1) and Q(2), we can estimate a rotational temperature $T_r = 10$ K.

The intensity of rotational transitions are approximately given by:

$$I \propto p\left(J'', t\right) A\left(J'', J'\right) \qquad \text{(2.10)}$$

where $p(J'', \Gamma)$ is the population of the initial state. $A(J'', J')$ is the rotational Hönl-London factor:

$$A\left(J'', J'\right) = \frac{2J'+1}{2J''+1} \qquad \text{(2.11)}$$

where J'', and J' are the angular momentum quantum numbers of the ground and excited states, respectively. For the Q branch transitions, J'' and J' are identical, and the transition intensities scale directly with the population of the initial level. We measured the CRD spectra at the same or a similar nozzle temperature used for the sticking coefficient measurements. The calculated rotational temperature and initial population in the $J = 1$ rotational level of the ground state are given in Table 2.4.

Table 2.4 Fractional initial population f_{pop} in the level J = 1 of the ground vibrational state.

Mixture	T_n (K)	T_r (K)	f_{pop}
1% CH_4/H_2	373	6.3	0.56
1% CH_4/H_2	323	10.5	0.51
6% CH_4/H_2	323	5.5	0.56
12% CH_4/H_2	323	4.0	0.56
25% CH_4/H_2	323	10	0.52
100% CH_4	323	13.7	0.47
30% CH_4/Ar	323	19	0.40

2.5.3 Determination of the excited state population

Now that we know the fractional populations of the ground rovibrational state in our molecular beam, we want to determine the maximum fractional population $f_{exc,\max}^{laser}$ that can be transferred by our IR pump laser to a selected vibrationally-excited state. For IR transitions, the rotational selection rules are:

$\Delta J = 0, \pm 1$

These selection rules give rise to the P ($\Delta J = -1$), Q ($\Delta J = 0$) and R ($\Delta J = +1$) branch structure of the $F_2 \leftarrow A_1$ vibrational bands in T_d. For laser excitation with linearly polarized light, the usual selection rule for the quantum number m describing the orientation of J with respect to the laser polarization (which is fixed in the lab frame) must also be satisfied:

P,R branch: $\Delta m = 0$

Q branch: $\Delta m = 0, m \neq 0$

Because linearly polarized light can induce only transitions for which $\left\langle J''m'',10 \middle| J'm' \right\rangle^2 \quad 0$, and in the absence of rapid re-orientation (via collisions) of J in a molecular beam, excited levels with $m = J'$ are not populated for R-branch excitation. Hence, the total degeneracy of the states involved in the laser excitation step is the same for the ground state and the excited state (see Schmid[40]). Knowing these selection rules and the degeneracy of the initial and excited state, we can calculate $f_{exc,max}^{laser}$:

R branch: $\quad f_{exc,max}^{laser} = \dfrac{2J''+1}{2(2J''+1)} = 50\%$

Q branch: $\quad f_{exc,max}^{laser} = \dfrac{2J'+1}{2(2J''+1)} \leq 50\%$

P branch: $\quad f_{exc,max}^{laser} = \dfrac{2J'+1}{2(2J''+1)} \leq 50\%$

where J'' is the rotational quantum number of initial state and J' is the rotational quantum number of excited state. In order to excite a maximum fraction of molecules in the jet, for our laser-excitation experiments we select the R(1) transition to prepare methane in the $2\nu_3$, $\nu_1+\nu_4$ and $2\nu_2+\nu_4$ vibrational states. In order to determine the degree of saturation f_{sat} of the optical transitions, we have used the same method described by Schmid [40] and Dang[41], measuring the apparent sticking coefficient of vibrationally excited methane as a function of laser energy. Figure 2.14, 2.15 and 2.16 show the reactivity of CH_4 excited via the R(1) transition of the $2\nu_3$, $\nu_1+\nu_4$ and $2\nu_2+\nu_4$ bands as function of average laser power.
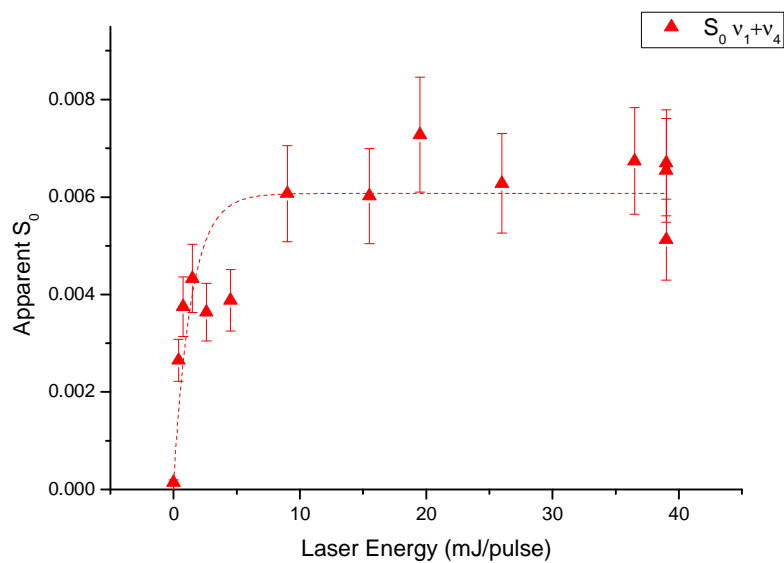
Figure 2.14 Laser fluence dependence of the methane (E_n = 33 kJ/mol) sticking coefficient after excitation of the $\nu_1+\nu_4$ mode.
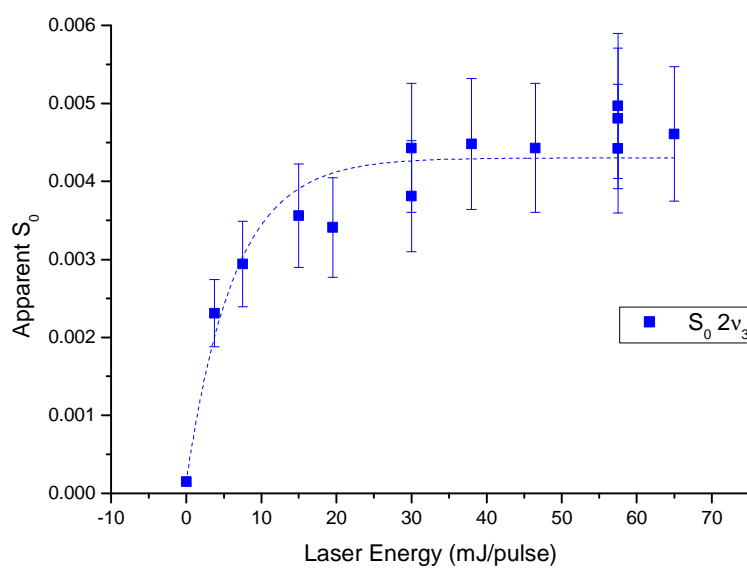
Figure 2.15 Laser fluence dependence of the methane (E_n = 33 kJ/mol) sticking coefficient after excitation of the $2\nu_3$ mode.
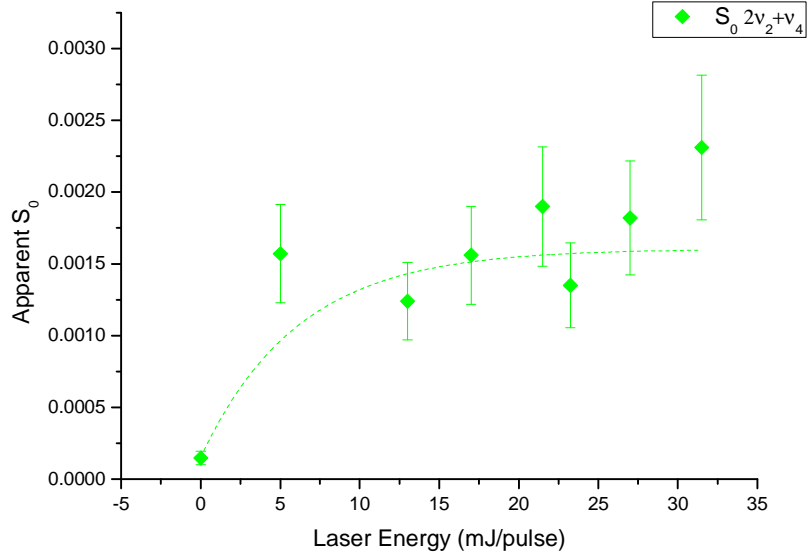
Figure 2.16 Laser fluence dependence of the methane (E_n = 33 kJ/mol) sticking coefficient after excitation of the $2\nu_2+\nu_4$ mode.

The extent to which an infrared transition can be saturated by incoherent optical excitation can be calculated from the Einstein coefficient B_{12} of the transition, the degeneracies of the lower and upper state g_1 and g_2, respectively, the radiation density ρ and the interaction time t between the radiation and the sample. The fractional saturation f is given by the following equation:

$$f = 1 - \exp\left(-\rho\left(\frac{g_1 + g_2}{g_2}\right)B_{12}t\right) \qquad \textbf{(2.12)}$$

In our experiment the interaction time corresponds to the laser pulse duration (10 ns), and for R(1) transition the degeneracies are calculated asfollows[40]: all J levels are (2J+1) fold degenerate for the 2J+1 different orientations of J in the laboratory frame. Additionally, the effective nuclear spin weights 5 : 2 : 3 for the A, E, and F levels apply. As showed above, the levels with m=J are not populated in the excited state, hence, in the vibrational ground state, the total degeneracy of the (J = 1) level (F_2) is (3 x 3) = 9. In the excited state, the total degeneracy of the (J = 2) level (F_2) is (3 x 3) = 9.

42

The expression 2.12 is based on the "rate-equations" description of a two-level system, which neglect the effects of the laser coherence. For coherent excitation with an ideal single-mode laser, the excitation process is described by the optical Bloch equations. If the relaxation is slow compared to the excitation rate, then the excited state population does not approach the saturation value predicted by eq. 2.12, but it oscillates periodically between 0 and 1 with the Rabi frequency given by:

$$\Omega_{\text{Rabi}} = \frac{\mu_{12} E_0}{\hbar} \qquad \textbf{(2.13)}$$

where μ_{12} is the transition dipole moment obtained from the Einstein coefficient B_{12} and E_0 is the electric field strength of the laser in the excitation region. Using an ideal laser with the proper pulse duration, one could produce a so-called π pulse, which completely inverts the initial population and leaves all molecules in the excited state. However, the less than ideal coherence properties of our pulsed dye laser, which typically operates on at least two longitudinal modes, and the variation of the laser intensity across the focus make this π-pulse excitation over the entire focal volume impossible. In fact, the spatial variation in our laser intensity, when integrated over several Rabi cycles, effectively averages the excited state population so that the produced fraction of excited molecules is consistent with the value predicted by equation 2.12. We determine f by fitting our data to the equation 2.12, the fitting result are reported in Table 2.5.

Table 2.5 Fractional saturation of the rovibrational transitions excited in this work and B_{12} Einstein coefficients from HITRAN database[56].

rovibrational transition	fractional saturation f (%)	HITRAN B_{12} [m^3/(J s^2)]
R(1) $\nu_1 + \nu_4$	99.999 ± 0.001	1.67×10^{15}
R(1) $2\nu_3$	99.904 ± 0.098	2.90×10^{14}
R(1) $2\nu_2 + \nu_4$	99.420 ± 2.038	2.32×10^{14}

The results reported in Table 2.5 show that we can saturate the R(1) transitions to the three vibrationally excited state studied here If we apply equation 2.12, using the Einstein coefficients of the HITRAN database, we can compare the fractional saturation we have determined from the fluence dependence curves with the degree of saturation predicted by the theory. For R(1) $2\nu_2 + \nu_4$, $B_{12} = 2.32 \times 10^{14}$ [m^3/(J s^2)] (Table 2.5); knowing the energy and the duration of our IR laser pulses, we can calculate (using eq. 2.12) a theoretical fractional saturation $f_{theory} = 92.5$ %. This result is in good agreement with the experimental observation that we can saturate all the transitions we have excited, especially the R(1) $2\nu_3$ and the R(1) $2\nu_1 + \nu_4$ that have higher cross-sections than the R(1) $2\nu_2 + \nu_4$.

2.6   Calculation of fraction of excited molecule

Our determination of the fractional excitation for a particular experiment is summarized here. The calculation is based on the expression for S_0 reported by Juurlink[28]:

$$S_0^{exc} = \frac{S_0^{laser-on} - S_0^{laser-off}}{f_{exc}} + S_0^{v=0} \qquad \textbf{(2.14)}$$

where $S_0^{laser-on}$ is the average sticking coefficient with laser excitation and $S_0^{laser-off}$ is the average sticking coefficient without laser excitation which as are determined by AES measurement. From Table 2.1 we know that $S_0^{laser-off}$ is a very close upper limit to $S_0^{v=0}$, but, in order to calculate S_0^{exc} with equation 2.14, we have to determine f_{exc}.

As reported by Schmid[39], we can express f_{exc} as the product:

$$f_{exc} = f_{overlap} f_{exc}^{laser} \qquad \textbf{(2.15)}$$

where $f_{overlap}$ is the fraction of the molecular beam pulse that is illuminated by the laser beam and f_{exc}^{laser} is the fraction of irradiated molecules that are promoted to the upper state.

The $f_{overlap}$ is determined by dividing the length of the laser line focus by the length of the molecular beam pulse. We have determined the former to be ~2.7 cm by burning a photosensitive paper and measuring the length of the mark on the paper. The latter is calculated from the speed of the molecular beam and the opening time of the chopper wheel.

The f_{exc}^{laser} is decomposed into three terms:

$$f_{exc}^{laser} = f_{pop} f_{exc,\max}^{laser} f_{saturation} \qquad \textbf{(2.16)}$$

where f_{pop} is the fractional population of the initial state of the excited transition, $f_{exc,\max}^{laser}$ is the maximum fractional population that can be transferred to the upper vibrational state and the $f_{saturation}$ is the degree of saturation of the optical transition.

The f_{pop} is calculated from the rotational population of the beam measured from the cavity ring-down spectra. The second term $f_{exc,\max}^{laser}$ is calculated from the degeneracy of the initial state involved in the optical transition, taking into account the selection rules for our linearly polarized laser. As described in section 2.5.3, for R branch transitions:

$$f_{exc,\max}^{laser} = \frac{2J''+1}{2(2J''+1)} = 0.5 \qquad \textbf{(2.17)}$$

45

The last term, $f_{saturation}$, is determined experimentally by recording the laser power dependence of the laser-on signal (see section 2.5.3). Examples of actual f_{exc} obtained in these experiments are reported in Table 2.6.

Table 2.6 Examples of fractional excitation f_{exc} obtained in these experiments for excitation of the R(1) transition of the $2\nu_3$ vibration. The definition of all the parameters reported in the table is given above in the text.

mixture	E_n (kJ/mol)	$f_{overlap}$	f_{pop}	$f_{sat.}$	$f_{exc,max}^{laser}$	f_{exc}^{laser}	f_{exc}
1% CH_4/H_2	63	0.32	0.56	0.99	0.50	0.28	0.09
25% CH_4/H_2	22	0.63	0.52	0.99	0.50	0.26	0.16
100% CH_4	10	0.77	0.47	0.99	0.50	0.23	0.18

Chapter 3: State-Resolved reactivity of CH$_4$ on Pt(111)

3.1 Outline

The first part of this chapter (sections 3.1, 3.2 and 3.3) gives a summary of previous experimental results on the activated chemisorption of CH$_4$ on Pt(111). In the second part (sections 3.4 and 3.5), we describe state-resolved reactivity measurements for CH$_4$ in v = 0 (ground-state) and in the vibrationally excited states $2\nu_3$, and $\nu_1+\nu_4$. Finally, we compare our measurements for CH$_4$ on Pt(111) with results for CH$_4$ on Ni(111) obtained previously in our laboratory by Mathieu Schmid and Plinio Maroni[6, 40].

3.2 Introduction and previous results

Transition metal based catalysts are used in steam-reforming [63, 64] of natural gas, a process which converts CH$_4$ and H$_2$O into H$_2$ and CO. The key step in this reaction is the dissociative chemisorption of CH$_4$ on the catalyst surface. Despite the numerous experimental investigations, the microscopic details of this dissociative chemisorption reaction are not yet completely understood. In order to advance the understanding of this prototype reaction, significant efforts [6, 28, 31, 33-35, 40, 47, 65-67] have been made during the last twenty years to perform more and more detailed experimental studies which seek to determine the dependence of the methane sticking coefficient on the different forms of energy involved in the reaction: translational energy and internal energy of the incident molecule and thermal energy of the surface.

In one of these experiments, Luntz and Bethune[67] used molecular beam techniques to probe the effect of translational energy on the sticking probability of CH$_4$ on Pt(111) and found a near-

exponential increase in reactivity with increasing normal kinetic energy (Figure 3.1). Luntz and Bethune also investigated the effect of the surface temperature and the vibrational energy of the incident CH_4 on its reactivity on the Pt(111) surface. They measured the effect of varying T_s on S_0 and found an Arrhenius activation energy of ~16kJ/mol for variation of the surface temperature (Figure 3.1 a). Using two different carrier gases (H_2 and He) and nozzle temperatures (300 and 680 K), they prepared CH_4 in molecular beams with identical kinetic energy but different vibrational energy content. They observed a 2-fold higher reactivity for the hot CH_4/He mixture as compared to the cooler CH_4/H_2 mixture (Figure 3.1 b).

(a)   **(b)**
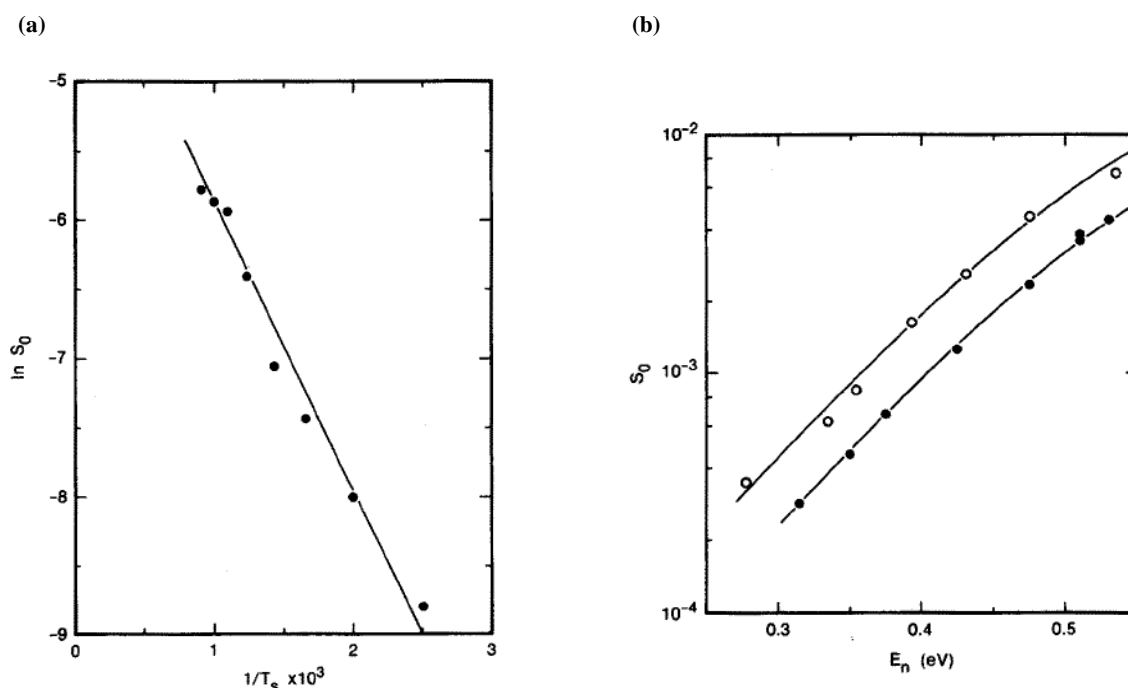
Figure 3.1 (a) Arrhenius plot of the variation of $ln(S_0)$ with $1/T_s$ for CH_4 on Pt(111), En = 41 kJ/mol. The line corresponds to an activation energy of 16 kJ/mol; **(b)** S_0 of CH_4 on Pt(111) as a function of the translational energy of the molecules, for two nozzle temperatures. T_s = 800 K. The solid points are for T_n = 300 K, the open points are for T_n = 680 K[67].

Luntz *et al.* reported that the energy added in all the thermally populated vibrational levels is about as efficient as the normal translational energy for promoting the reaction. However, experiments with thermally prepared vibrationally excited molecules cannot tell if there are specific vibrational modes that are more efficient in activating the reaction than others or if each

vibrational state contributes according to its energy. This question about the presence or absence of mode specificity in methane chemisorption can only be answered by state resolved experiments, with molecular beams of CH_4 prepared in specific ro-vibrational states.

In order to obtain more detailed information about the chemisorption process, Higgins *et al.* performed the first quantum state resolved reactivity measurement for methane on Pt(111)[31]. The authors used a tunable cw color-center laser in a resonant build-up cavity to excite methane to the first overtone of the antisymmetric C-H stretch ($2\nu_3$) mode and probed the reaction products by thermal energy atomic scattering (TEAS). This detection technique monitors the specular reflection of a thermal helium beam from the Pt(111) surface using a mass spectrometer and makes use of the large cross section for inelastic scattering from any adsorbed species on the surface to detect changes in adsorbate coverage with very high sensitivity. Using CH_4/He mixtures for their experiments, Higgins *et al.* determined sticking coefficients from the initial slope of the decay curves of the He specular intensity versus exposure. They reported a 30-fold reactivity enhancement upon excitation of the $2\nu_3$ state at incident normal kinetic energy of 5.4 kJ/mol[31] much lower than what is produced by an equivalent amount of translation energy. In order to quantitatively compare the effect of translation and $2\nu_3$ vibration, they introduced a vibrational efficacy parameter $\eta_{2\nu_3}$ as:

$$\eta_{2\nu_3} = \frac{\Delta E_n}{E_{2\nu_3}} \qquad \textbf{(3.1)}$$

where ΔE_n is the amount of normal translational energy required to achieve the same increase in reactivity for CH_4 in the ground state as observed for the addition of $\Delta E_{2\nu_3} = 72$ kJ/mol of vibrational energy by excitation of the $2\nu_3$ state. It was found that 72 kJ/mol of vibrational energy in the $2\nu_3$ excited CH_4 is equivalent to 30 kJ/mol of normal translational energy. This corresponds to a vibrational efficacy of ~40%. In their paper, it was pointed out that a vibrational efficacy different from 1 is inconsistent with a statistical reaction mechanism as it was proposed by Ukraintsev *et al.* [38].

3.3   The Pt(111) surface

Figure 3.2 (b) shows a LEED pattern obtained in our surface science chamber of a well ordered Pt(111) surface after 15 minutes of argon sputtering (1.5 kV, 20 µA) and 2 minutes annealing at 1200 K. The platinum crystal has a face-centered cubic structure (FCC). Every atom on the surface is in contact with 9 neighbors, 6 on the same plane and 3 on the layer immediately below. Since every atom on the top layer occupies an equivalent position, the Pt(111) surface can be considered to be "atomically flat". The surface density of the (111) plane is 1.5×10^{15} atoms/cm^{-2} and the lattice spacing between two nearest neighbor atoms is 2.27 Å [68, 69].

(a)   **(b)**
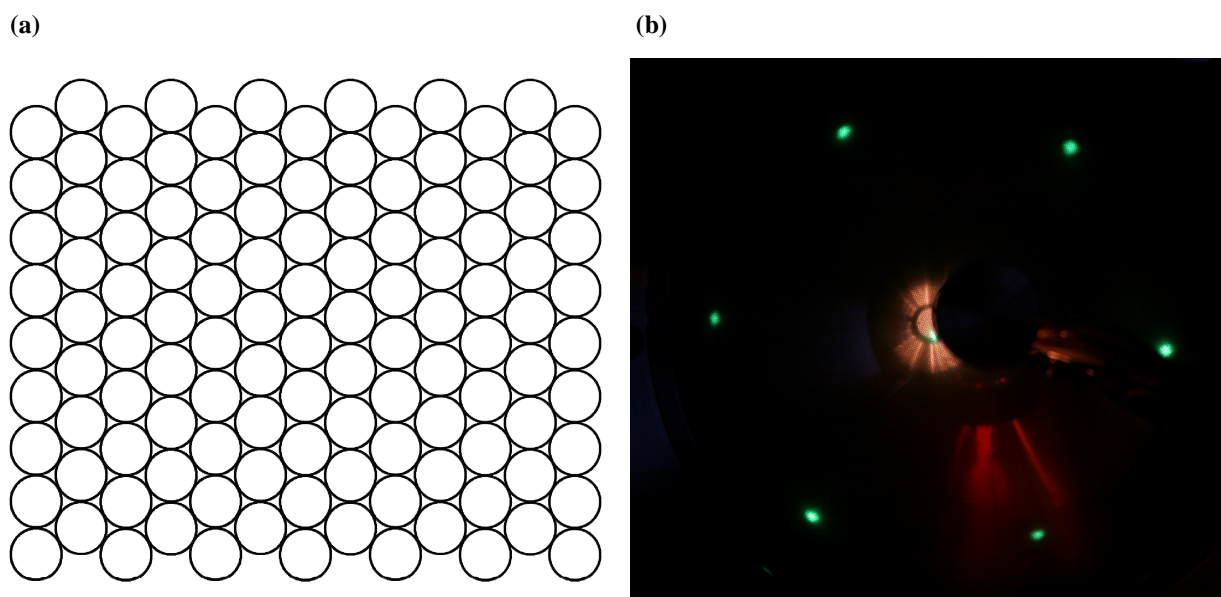
Figure 3.2 (a) Schematic illustration of the Pt(111) surface; **(b)** LEED pattern of a clean and well-annealed Pt(111) surface.

3.4   CH$_4$ ground state reactivity on Pt(111)

We measured the reaction probability of CH$_4$ as a function of the translational energy as described in Chapter 2. We varied the kinetic energy of the incident molecules by using mixtures

of methane with different carrier gas and concentration (Table 4.1), keeping the nozzle temperature constant (T_n = 323 K) for all the kinetic energies up to 54 kJ. At the low nozzle temperatures used for these experiments (323-373 K), only 1% of the molecules is thermally excited to the v=1 levels and the data represent nearly the upper limit to the ground-state sticking coefficient S_0(v = 0). Figure 3.3 shows the laser-off reactivity for CH_4 on Pt(111) as a function of kinetic energy for normal incidence. A near exponential increase in reactivity, by 4 orders of magnitude, is observed when the incident kinetic energy is raised from 10 to 64 kJ/mol.
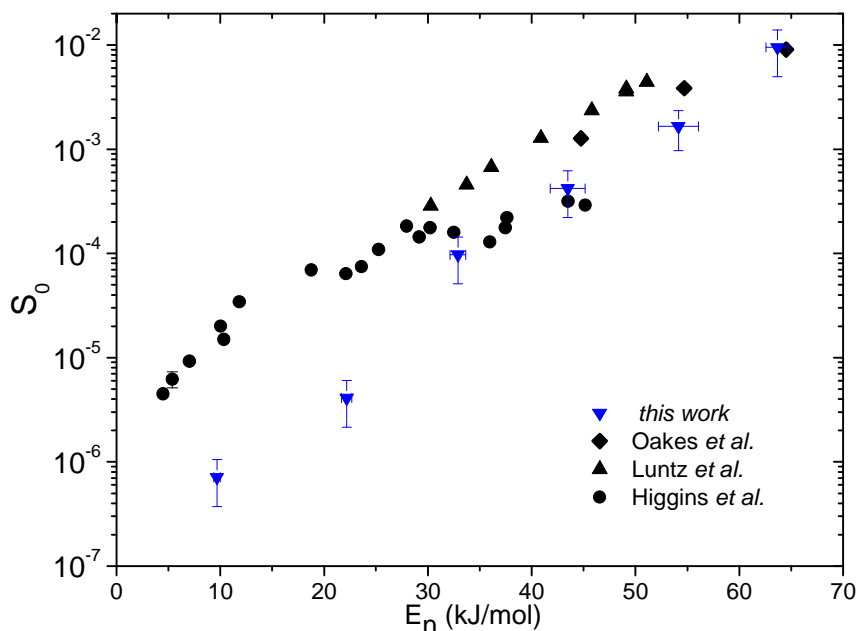
Figure 3.3 Laser-off reactivity of CH_4 on Pt(111) as a function of normal kinetic energy (E_n): (▼) this work, T_s = 600 K, T_n = 323-373 K; (▲) Luntz *et al.*, T_s = 800 K, T_n = 300 K; (◆) Oakes *et al.*, T_s = 550 K, T_n = 500-1000 K; (●) Higgins *et al.*, T_s = 575 K, T_n = 295-1073 K.[31, 47, 67, 70]

For comparison, we include in Figure 3.3 the results of several previous studies of CH_4 sticking coefficients on Pt(111)[31, 67, 70]. We observe significant deviations between our measurements and the data sets reported by different groups[31, 67, 70]. Some of the differences can be attributed to different surface and/or nozzle temperatures used in the various studies. The data reported by Luntz *et al.* were recorded at a surface temperature of 800 K, whereas we used

51

T_s = 600 K. If we consider the experimentally observed surface temperature dependence of the methane sticking coefficient reported by Luntz *et al*.[67], our results are in reasonable agreement. Taking into account the difference in T_n and T_s, the data reported by Oakes *et al.* are also consistent with our data at high kinetic energy.

On the other hand, the data reported by Higgins *et al*.[31] were recorded at similar surface temperature (575 vs 600 K) but show a significantly higher reactivity and smaller slope with increasing kinetic energy than our results. Higgins *et al*. varied the nozzle temperature from 295 to 1073 K to increase the normal kinetic energy of the CH_4 in He beam from 5 to 44 kJ/mol and of the CH_4 in H_2 beam from 22 to 52 kJ/mol. In their measurements, Higgins *et al*. used a continuous molecular beam, whereas we employed a pulsed molecular beam with higher instantaneous gas flux. To exclude the possibility that this higher instantaneous flux of CH_4 in H_2 could lead to a transient passivation of the Pt(111) surface by the adsorption of hydrogen, we repeated a number of laser-off reactivity measurements with a continuous beam produced by a pinhole nozzle of 30 μm diameter with no significant difference in the results (Table 3.1).

Table 3.1 Reaction probability of CH_4 on Pt(111), T_s = 600 K.

	E_n (kJ/mol)	S_0
CH_4/H_2 *continuous beam*	19 ± 0.5	$1.5 \pm 0.7 \times 10^{-6}$
CH_4/H_2 *pulsed beam*	22 ± 0.5	$1.8 \pm 0.8 \times 10^{-6}$

We also compared the reactivity of a pulsed beam of 25% CH_4 in H_2 to that of a beam of 3% CH_4 in He at identical nozzle temperatures and very similar kinetic energies and detected no significant difference in reactivity. Finally, our reactivity measurement at E_n = 10 kJ/mol is obtained with a pure beam of CH_4, which excludes hydrogen passivation from the carrier gas but which shows no deviation from the trend of lower sticking coefficients as compared to those observed by Higgins *et al*. We can therefore only speculate about the reasons for the discrepancy between our results and those of Higgins *et al.* The high sensitivity of the TEAS method used by Higgins *et al*. and the fact that the sticking coefficients were measured for very low coverages (<1% ML) could cause their measurements to be influenced by surface defects. The reactivity at step edges and kink sites, which are present on a single-crystal surface in concentrations

52

depending on the miscut, sample preparation, and history, is known to be significantly higher than that on terraces, [71] which could lead to a higher (averaged) sticking coefficient measured at low incident energy where the reactivity on the terraces is still exceedingly low. We can also observe that Higgins *et al*. have used a sample with 0.3° miscut, three times higher than the miscut of our crystal (0.1°), this could explain the presence of higher concentration of steps in their sample and the higher reactivity at low kinetic energy comparatively to our measurements.

Finally, we point out that all the measurements performed by Higgins *et al.* were collected at 45° incidence and reported as a function of the calculated normal energy component. The scaling procedure applied by Higgins *et al.* is legitimate because, as it was observed by Schoofs *et al.*[72], methane adsorption probability on Pt(111) follows approximately normal energy scaling.

3.5   Reactivity of vibrationally excited CH_4 on Pt(111)

3.5.1 Introduction

In this section, we describe the results of our state-resolved sticking coefficient measurements of CH_4 on the Pt(111) surface. With our tunable pulsed infrared laser setup[47], we excited the R(1) ro-vibrational transition of the $2\nu_3$ and $\nu_1+\nu_4$ states of CH_4. As discussed in Chapter 2, the $2\nu_3$ state label indicates the first overtone of the antisymmetric C-H stretch and the $\nu_1+\nu_4$ state is a combination of symmetric stretch (ν_1) and antisymmetric bend (ν_4) vibrations. We obtain the state resolved reactivity from the difference in average reactivity with and without laser excitation. We will also compare the state-resolved S_0 measurements for $2\nu_3$ on Pt(111) with previous results for the same state on Ni(111). The observed differences in reactivity are discussed in terms of difference in barrier height and transition state location on the two surfaces.

3.5.2 State-resolved reactivity of CH_4 ($2\nu_3$) on Pt(111)

Figure 3.4 shows state-resolved sticking coefficients for $CH_4(2\nu_3)$ as a function of incident translation energy E_n at normal incidence. The deposition time of a "laser-on" experiment varies from 10 min at $E_n = 63$ kJ/mol to 9 hours at $E_n = 10$ kJ/mol. It was verified that the "laser-on" measurements are not affected by artifacts by performing "blank-test" experiments in which we intentionally tuned the laser out of resonance with the transition or by timing the laser pulse after the gas pulse has passed through the alignment tool. In both cases we did not observe any detectable reactivity enhancement relative to S_0(laser-off)
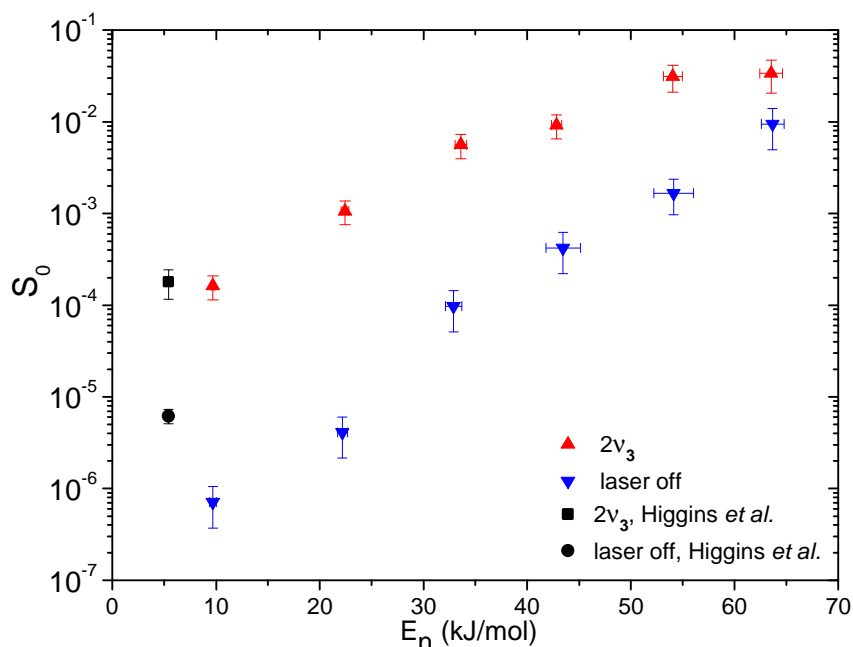
Figure 3.4 Sticking coefficients as a function of incident kinetic energy (normal incidence) for dissociative chemisorption of CH_4 on Pt(111). (▼) Laser-off data giving an upper limit for $S_0(v = 0)$, (▲) state-resolved sticking coefficients for $2\nu_3$, J = 2. For comparison, we also show the data obtained by Higgins *et al*., (■) $2\nu_3$, J = 1, 2, (●) laser-off.

The error bars reported in Figure 3.4 have been calculated from the statistical error of the measurement and the error coming from the calibration procedure (see Chapter 2). The statistical

error represents the 95% of confidence limit of the measurements and it has been calculated by student T-statistics of repeated measurements at the same kinetic energy.

Figure 3.4 shows that vibrational excitation to $2\nu_3$ enhances the chemisorption probability of CH_4 on Pt(111) over the full E_n range spanned by our measurements. This observation, in agreement with the previous results of Luntz and Bethune[67] and Higgins *et al.*[31], suggests that both the normal translational and the vibrational energy of the molecules contribute to overcome the reaction barrier. Experimental limitations prevented us from measuring "laser-on" S_0 at higher and lower kinetic energies. For the higher kinetic energies, the difference in reaction probability between unexcited and laser-excited molecules decreases rapidly, making the "laser-on" peak too difficult to detect above the "laser-off" background; for lower kinetic energy, the reactivity of the laser-excited beam is too low to produce a detectable carbon signal even after 9 hours of deposition. At $E_n = 10$ kJ/mol, the lowest incident energy investigated here, we observe a 300-fold increase in reactivity upon $2\nu_3$ excitation. Higgins *et al.* reported a factor of 30 enhancement at the same total kinetic energy but for an incidence angle of 45°, corresponding to a normal energy of 5.4 kJ/mol, primarily because their laser-off measurement of S_0 is higher (Figure 3.4). Because T_s (575 and 600 K) and T_n (298 and 323 K) for the two measurements are nearly identical, we can only speculate that their laser-off measurement reflects at least in part the reactivity at step edges or other defects and that the reaction at these sites is less strongly activated by $2\nu_3$ excitation.

3.5.3 Comparing the effect of stretch and bend excitation on the reactivity of CH_4 on Pt(111)

In this section, we discuss the question of mode specificity, i.e. if methane chemisorption on Pt(111) depends on the particular vibrational motion of the incident CH_4 before the impact with the surface. To answer this question, we compare the state-resolved reactivity measured for the $2\nu_3$ state with that for another vibrational state that can be prepared by our pulsed IR laser system. By tuning the IR excitation laser to 4229 cm^{-1}, we can excite the R(1) transition of the $\nu_1+\nu_4$ stretch-bend combination band of methane and measure the state-resolved reactivity for

this state. Figure 3.5 shows a comparison of the reactivity of CH_4 on Pt(111) for the $2\nu_3$ and $\nu_1+\nu_4$ vibrational states, as a function of the translational energy E_n of the incident molecular beam.
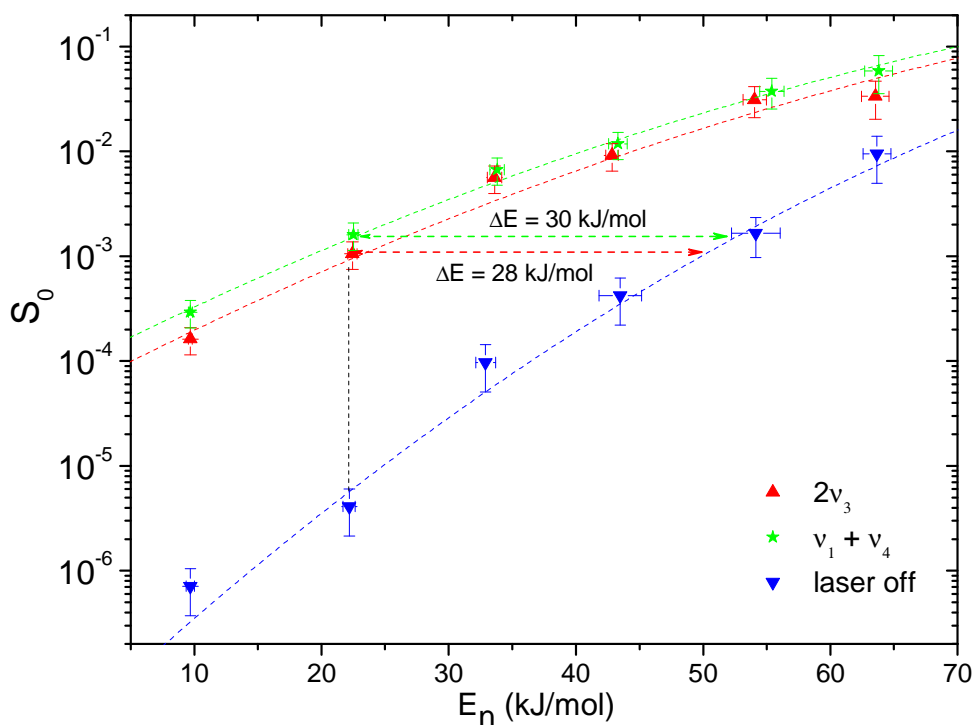
Figure 3.5 Sticking coefficients as a function of incident kinetic energy (normal incidence) for dissociative chemisorption of CH_4 on Pt(111) ($T_s = 600K$). ($\blacktriangledown$) Laser-off data, ($\star$) $\nu_1+\nu_4$, ($\blacktriangle$) $2\nu_3$. The horizontal dashed arrows indicate the amount of normal kinetic energy which produces the same increase in reactivity as the vibrational excitation. The dashed curves are "S"-curve fittings (equation 3.3) of the laser-off points.

Although the $2\nu_3$ state is 21 kJ/mol higher in energy than the $\nu_1+\nu_4$ state, we observe a very similar increase in methane chemisorption probability for the two states. In Table 3.2, we report the vibrational efficacy for the $2\nu_3$ and $\nu_1+\nu_4$ states measured at $E_n = 22$ kJ/mol, where both states enhance the reaction probability by ~300 times. We find the vibrational efficacy of the $\nu_1+\nu_4$ state to be ~ 60% higher than $\eta_{2\nu_3}^{Pt(111)}$ (Table 3.2).

Table 3.2 The vibrational efficacy[34] is a parameter that compares the effect of vibrational and translational energy on the reaction probability (eq. 3.1). The vibrational efficacies on Pt(111) are calculated at kinetic energy of 22 kJ/mol.

CH_4 State	Vibrational Energy (kJ/mol)	Vibrational Efficacy, η
$2\nu_3$	71.4	39%
$\nu_1+\nu_4$	50.5	60%

From this observation, we can draw a first important conclusion: the interaction between the gas phase molecule and the surface does not induce a rapid mixing of the initially prepared eigenstate via intramolecular energy redistribution (IVR). In fact, even at the lowest speed used (1100 m/s) in this work (E_n = 10 kJ/mol), it take only about 200 fs to traverse the typical interaction region with the surface (~2 Å). From this simple estimate, we estimate that surface induced IVR is incomplete on a timescale of 200 fs.

Furthermore, we observe that the vibrational efficacies of both the $2\nu_3$ and $\nu_1+\nu_4$ states on Pt(111) are much lower than unity. This suggests that the energy available in the vibrational states may not be fully available to overcome the reaction barrier, in contradiction with the statistical model of Ukraintsev *et al.*[38]. In fact, in the statistical models it is assumed that the internal rotational and vibrational energy of the molecule is simply added to the total pool of energy available for overcoming the reaction barrier. Vibrational efficacies different than unity, as well as different efficacies for different vibrational states (state specificity), are hence inconsistent with statistical models of the reaction mechanism.

3.5.4 Surface induced perturbation

Excitation of a molecular eigenstate of methane, in a collision-free environment such as a supersonic molecular beam, has the effect of preparing the molecule in a stationary state[73]. However, the time independent nature of the excited molecular eigenstate changes dramatically

as the molecules approach the surface and the interaction with the surface induces a perturbation in the molecular energy levels. It was suggested[74] that the effect of a strong perturbation was to randomly scramble the initial vibrational excitation via fast surface induced IVR. As we will discuss in the next section, this is one of the fundamental assumption of statistical models of gas-surface reactions.

Another possibility is that the perturbation induced by the surface, will instead gradually redistribute the vibrational energy initially localized in the excited eigenstate. For the gas phase reaction CH_3D + Cl, the evolution of the vibrational eigenstates of CH_3D, as the molecule approaches the Cl atom, has been investigated by Yoon *et al.*[24] using Møller-Plesset perturbation theory calculations. They found that the perturbation induced by the approaching Cl atom preferentially converts the symmetric C-H stretch into motion of the H atom pointing toward the incoming Cl. Conversely, the antisymmetric stretch is converted into motion of H atoms away from the incoming Cl atom. This model can explain qualitatively the fact that the abstraction of H atoms by Cl is 7 times more probable from CH_3D molecules with the symmetric C-H stretching vibration excited than for ones with the antisymmetric C-H stretch excited, even though these two states have nearly the same energy[24]. In the remainder of this chapter, we attempt to explain the higher vibrational efficacy for $\nu_1+\nu_4$ compared to $2\nu_3$. We suggest that preparing different initial states and measuring their reactivity is a way to probe to what extent the excited vibrational state maps onto the reaction coordinate[16].

Here the reaction coordinate is defined as the motion that carries the system across the barrier on the PES[9]. At the saddle point, the molecule is in the transition state configuration and the reaction coordinate coincides with the vibrational mode of the transition state with an imaginary frequency (the transition state normal mode)[75]. It is useful to describe this specific "reactive" motion at the TS in a normal mode basis:

$$q_{TS} = \sum_{i=1}^{3N-6} C_i q_i \qquad \textbf{(3.2)}$$

where q_{TS} is the reaction coordinate expressed as linear combination of the 3N-6 molecular normal modes q_i.

We propose that the excitation of a molecular eigenstate that maps onto the reaction coordinate will be the most energetically efficient way to promote the reaction by vibrational excitation.

In the following, we compare our state-resolved measurements with the predictions of existing theoretical models of CH_4 chemisorption. Our results are in qualitative agreement with predictions of adiabatic vibrational calculations[30] and ten-dimensional wave packet simulations[37] which do not assume a statistical mechanism. Finally, we suggest that our results can be rationalized by observing that the calculated transition state structure reported by Psofogiannakis *et al.*[75] indicates that both elongation and bending of the breaking C-H bond are involved in the chemisorption process.

3.5.5 Microcanonical Unimolecular Rate Theory (PC-MURT)

In the statistical PC-MURT model developed by the group of Harrison [38, 45, 74, 76-79], it is assumed that the incident methane forms a transient collision complex consisting of CH_4 and *s* immediately adjacent surface atoms, where *s* is an adjustable parameter of the theory. This hot physisorbed complex, treated to be adiabatically isolated, can undergo competitive unimolecular decay (chemisorption) or intact desorption of CH_4 into the gas phase.

The chemisorption probability is determined from the unimolecular dissociation and desorption rates, calculated according to the Rice-Ramsperger-Kassel-Marcus (RRKM) theory. RRKM theory postulates that the energy of the reaction complex is rapidly and randomly redistributed amongst all the degrees of freedom and that this energy redistribution is much faster than the reaction rate.

The MURT model proposed by Bukoski and Harrison[74] has three adjustable TS parameters that can only be fixed by simulating available experimental results:

s, the number of surface atoms interacting with the molecule in the adsorption complex;

ν_D, the frequency of C-H stretch vibration that constitutes the reaction coordinate;

E_0, the energy barrier for the reaction.

As a consequence of the assumption of fast IVR, the MURT model predicts the reactivity to scale with the total molecular energy, independently of the initially excited vibrational state.

59

Bukoski *et al.*[74, 78, 79] claim that the MURT model successfully simulates several experimental data sets relative to molecular beam deposition of CH_4 on Ni(100) and Pt(111).

Our results, however, are not consistent with this statistical model, since we observe that the CH_4 reaction probability is strongly dependent on the initial vibrational quantum state. From our results we can deduce, in contrast with the assumptions of the model, that the interaction with the metal surface does not induce complete IVR before the reaction occurs.

3.5.6 Vibrationally adiabatic model

Halonen *et al.*[30] performed four-dimensional variational calculations to model the energy redistribution in the methane stretching vibrational states as the molecule adiabatically approaches a flat metal surface. To make these calculations feasible, several approximations were made by the authors. First, the H-C-H angle is considered constant, i.e. bending motions are neglected. Second, the molecular orientation is fixed with one C-H bond pointing to the surface. Finally, the interaction between the surface and the molecule is modeled with a London-Eyring-Polanyi-Sato (LEPS) potential and occurs only via the unique C-H bond which is pointing towards the surface. Their results show that the symmetric stretch energy is lowered as the molecule approaches the surface due to the fact that v_1 vibrational state adiabatically correlates with the localized vibration of the weakened C-H bond pointing to the metal surface.

By contrast, the energy of the antisymmetric stretching mode v_3 remains nearly unchanged as the molecule approaches the surface. In fact, the v_3 state correlates with vibrations of the CH_3 group pointing away from the surface, therefore, when the v_3 excited methane molecule approaches the surface, the vibrational energy is "quarantined" into the CH_3 group.

Landau-Zener semiclassical analysis was used to calculate the characteristic velocities (Massey velocities) from which the crossing probability of the initially excited states can be estimated. For the fundamental manifold, a crossing between the v_1 and v_3 states was identified at 2.6 Å from the surface with a characteristic Massey velocity of 1440 m/s, whereas for the overtone manifold, the avoided crossings that involves the $2v_3$ state and the v_1+v_3 combination

state were identified at 2.45 Å from the surface, with a Massey velocity of 610 m/s ($E_n \sim 3$ kJ/mol).

It is suggested that, when the speed of the molecules is much higher than 610 m/s, the initial identity of the $2\nu_3$ vibrational state would be lost as a result of the non-adiabatic crossing to the $\nu_1+\nu_3$ state. Since the calculated Massey velocity are comparable with the typical CH_4 approach velocities sampled in this and previous molecular beam experiments[28, 31, 32, 35, 36, 80], the authors indicate that both adiabatic and nonadiabatic pathways are possible. In particular, they suggest that the large reactivity enhancement observed for excitation of one quantum[28] and two quanta[31] of CH_4 (ν_3) antisymmetric stretch vibration could be explained by non-adiabatic crossing between vibrational states.

In the kinetic energy range of our experiment (> 10 kJ/mol), the speed of the molecules approaching the surface exceeds (up to 4 times) the Massey velocity estimated for the $2\nu_3$ state. If the assumptions of the model proposed by Halonen *et al.* are valid, we should expect that the mixing of the $2\nu_3$ state with the $\nu_1+\nu_3$ state by non-adiabatic crossing, will enhance the reaction probability as much as excitation of the $\nu_1+\nu_4$ state, since both vibrations contain one quantum of symmetric stretch. Indeed, we measured very similar reaction probability after excitation of the $2\nu_3$ and the $\nu_1+\nu_4$ vibrations, hence our results seem to confirm the prediction of this vibrationally adiabatic model.

3.5.7 Wave packet simulation

Milot and Jansen[37, 81, 82] used a multiconfigurational time dependent Hartree method (MCTDH), with a potential energy surface based on earlier density functional theory (DFT) calculations by the same group[83], to perform wave packet simulations of methane scattering on Ni(111), including all nine internal vibrations.

Milot *et al.* found that, in the configuration of three C–H bonds pointing towards the surface, the translational energy loss in inelastic scattering depends on the vibrational state of the incident molecule following the trend: $\nu_1 > \nu_3 > \nu_4 >$ ground state (Figure 3.6).

Even though the authors did not attempt to describe the chemisorption process itself, the scattering simulations give indications for the role of vibrational excitation in the dissociation of methane. In fact, their calculations show that initial vibrational excitation favors translational kinetic energy transfer toward intramolecular vibrational energy[81, 82]. Meaning that the energy lost during the inelastic scattering process is transferred to vibrational stretching modes at the turnaround point.
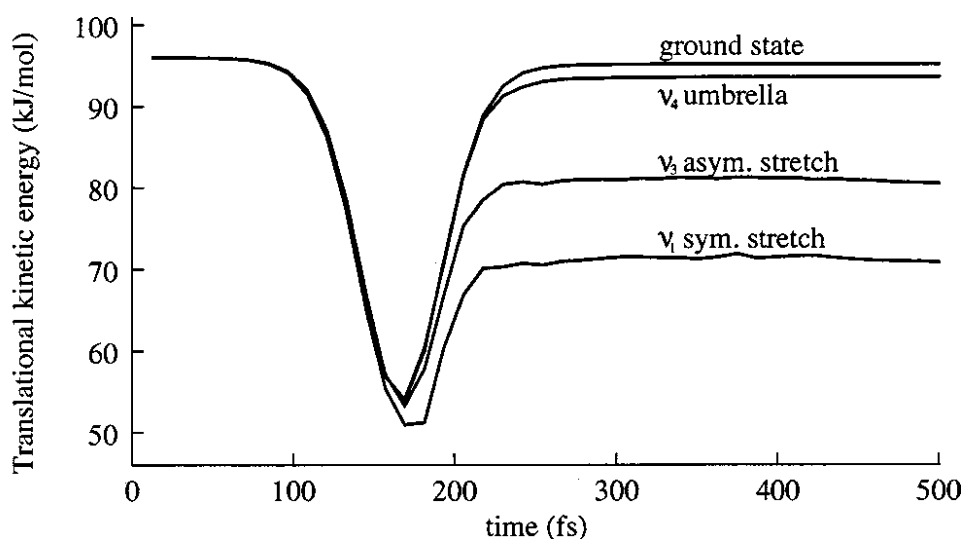
Figure 3.6 Translational kinetic energy versus time for a CH_4 molecule with three bonds pointing towards the surface. (Milot *et al.*[82]). The inelastic scatter component (the initial minus the final translational energy) shows the following trend for the initial vibrational excitations of the modes: $v_1 > v_3 > v_4 >$ ground state.

Based on this inelasticity, and observing that vibrational excitation of the v_1 mode produces spreading of the wave packet along a single C–H bond, the authors suggested that the v_1 symmetric stretch should be more effective than the antisymmetric stretch v_3 in promoting the CH_4 dissociation on a Ni(111) surface. While the PES used in these calculations is chosen for modeling the CH_4/Ni(111) interaction, their conclusions can also be applied to the dissociation of methane on the similar Pt(111) surface. Indeed, we found that the higher vibrational efficacy of the $v_1 + v_4$ with respect to the $2v_3$ confirms the qualitative trends indicated by these simulations.

3.5.8 Transition state structure

Psofogiannakis *et al.* [75] performed density functional theory calculations (using B3LYP and PW91 functionals) to determine the energy and the geometry of the CH_4 transition-state complex on a Pt(111) surface simulated by a 25-atom Pt cluster (Figure 3.7). Their calculation predicts that, at the TS, the C atom of methane is located 2.20 Å on top of a Pt atom and the H atom 1.57 Å from the C atom and is bridge-bonded to the underlying Pt atoms. The C-H dissociating bond is significantly stretched relative to its equilibrium configuration (1.09 Å) and bent towards the nearest bridge site. From the bond lengths given in Figure 3.7, we calculated that the angle $H - \hat{C} - Pt$ between the Pt-CH_3 bond and the breaking C-H bond is ~54°.
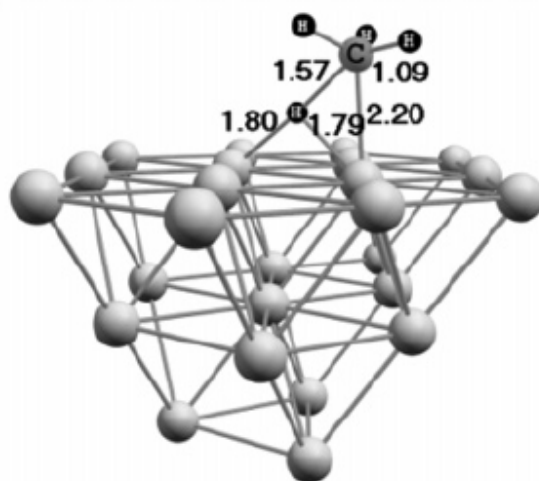
Figure 3.7 Transition state for the reaction $CH_4 \rightarrow CH_{3\ (ads)} + H_{(ads)}$ on a Pt_{25} cluster calculated with the B3LYP functional. (Psofogiannakis *et al.*[75]). Bonds lengths and distances in the figure are in Å.

In our experiments, we observed that vibrational excitation of CH_4 increases the chemisorption probability up to 300 times. Such vibrational activation of a reaction is typically associated with a "late" barrier[12] which corresponds to a transition state structure for which the dissociating bond is significantly stretched. Electronic structure calculations by Psofogiannakis *et al.* confirm that the breaking C-H bond at the transition state is very elongated (1.57 Å).

It is more difficult to deduce the possible contribution of bending vibrations from the "static" transition state structure. If the only outcome of the reaction was the breaking of one H_3C-H bond, than one would expect that bending vibrations would not influence significantly the reaction probability. However, the TS structure is more complex and involves simultaneous breaking of one C-H bond and formation of one Pt-H and one H_3C-Pt bond. One can imagine that for some impact orientations, for example when one of the C-H bonds of CH_4 is pointing towards the surface, a pure stretching vibration would not be the best way to enhance the reaction probability. In fact, while this configuration is optimal for the Pt-H bond formation, it is clear that no C-Pt bond can possibly be formed on the H_3C---H---Pt coordinate. Therefore, we suggest that, in this and in similar configurations, the excitation of a bending mode could contribute in "*moving the hydrogen atom out of the way*"[84] and favor the formation of the H_3C-Pt bond.

To conclude, since the dissociating C-H bond in methane at the TS is both stretched and bent from its equilibrium geometry, one can speculate that the most efficient way to enhance the dissociation will be to provide energy in both stretching and bending vibrations. Indeed, in this work we have observed that the $\nu_1+\nu_4$ state has a much higher vibrational efficacy than the $2\nu_3$ state.

3.6 Comparison between the state-resolved reactivity of CH4($2\nu_3$) on Pt(111) and Ni(111)

Figure 3.8 shows a comparison of our state-resolved sticking coefficient measurements (for laser-off and for $2\nu_3$) on Pt(111) with the results obtained previously in our laboratory for the same vibrational states on Ni(111).
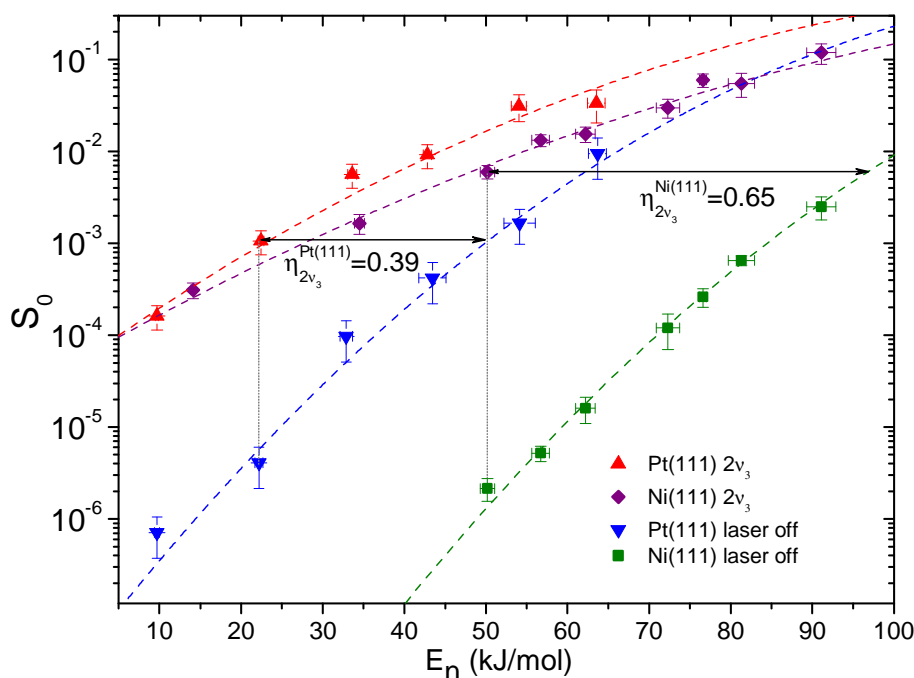
Figure 3.8 Comparison of the $2\nu_3$ and laser-off reactivity for Pt(111) (T_s = 600 K) and Ni(111) (T_s = 475 K): (▲) $2\nu_3$, Pt(111); (▼) laseroff, Pt(111); (◆) $2\nu_3$, Ni(111); (■) laser-off, Ni(111). Dashed lines are "S"-shaped curves, fitted to the laser-on and laser-off data and used to determine the difference in average barrier height ΔE_a between Pt(111) and Ni(111). The vibrational efficacies $\eta_{2\nu_3}$ for Pt(111) and Ni(111) are calculated at the incident kinetic energies indicated by the vertical dotted lines. The horizontal arrows indicate the amount of normal kinetic energy, which produces the same increase in reactivity as the excitation into the $2\nu_3$ vibrational state.

Two main differences for methane dissociation on the two metals are evident. (1) The ground-state reactivity of CH_4 on Ni(111) is approximately 3 orders of magnitude lower than on Pt(111), and (2) there is a a much stronger enhancement in reactivity upon $2\nu_3$ excitation for dissociation Ni(111). The lower laser-off reactivity for Ni(111) at a given incident kinetic energy is consistent with a higher barrier for methane dissociation on Ni(111) as compared to Pt(111). Although barrier heights reported in the literature vary over a considerable range, comparative studies treating both metal surfaces at the same level of theory found a higher barrier for Ni(111) than for Pt(111)[85, 86]. Here, we use our laser-off results for Pt(111) and Ni(111) to estimate the difference in barrier height between the two surfaces. Because our two data sets were recorded at different surface temperatures (600 K for Pt(111) and 475 K for Ni(111) to facilitate comparison with previous studies[34, 35, 84]), we correct the laser-off data for Pt(111) using the experimentally determined surface temperature dependence of S_0 by Luntz $et\ al.$[67]. Then, "S-curves", initially proposed by Luntz[87], are fitted to the data points to parametrize the variation of the laser-off sticking coefficients with kinetic energy E_n:

$$S_0(E,\nu)=\frac{A(\nu)}{2}\left(1+\text{erf}\left(\frac{E_n-E_0(\nu)}{W(\nu)}\right)\right) \quad \textbf{(3.3)}$$

where E_0 is the average barrier height, W is the width of a Gaussian distribution of barrier heights, and A is the asymptotic value of S_0 at high E_n. Fixing A = 1, we determine E_0 and W as fitting parameters by least-squares fits of eq. 3.2 to the laser-off data for Pt(111) and Ni(111).

These fits yield similar values for W on both metals ($W_{CH_4/Pt(111)} \approx W_{CH_4/Ni(111)} \approx 31\ (\pm\ 2\ \text{kJ/mol})$, reflected in the parallel rise of the S-curves in Figure 3.8. When compared to that of Pt(111), the fit for Ni(111) gives a higher average barrier height $E_{0,Ni(111)}$ by 28 ± 8 kJ/mol (Figure 3.9). Such a difference in barrier height is in good agreement with the comparative theoretical study by Anderson $et\ al.$[85] who found a higher reaction barrier on Ni(111) than on Pt(111) by 21 kJ/mol.
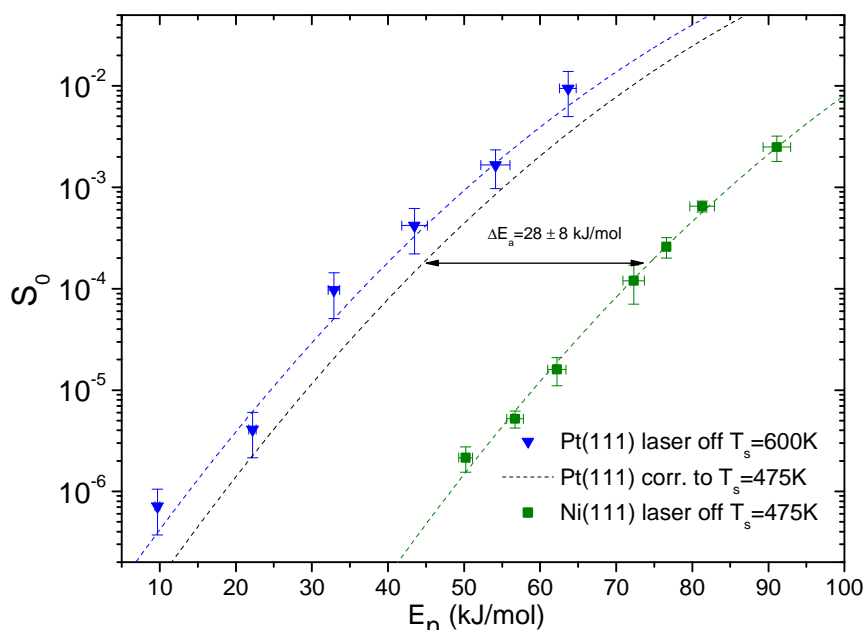
Figure 3.9 Comparison of the laser-off reactivity for Pt(111) (T_s = 600 K) and Ni(111) (T_s = 475 K): (▼) laseroff, Pt(111); (---) "S-curve" fitting to the Pt(111) laser-off data; (---) estimated reactivity for Pt(111) at T_s = 475 K using the T_s dependence reported by Luntz *et al.*[67].; (■) laser-off, Ni(111); (---) "S-curve" fitting to the Ni(111) laser-off data (T_s = 475 K). The horizontal arrow indicate the difference in average barrier height ΔE_a between Pt(111) and Ni(111) at 475 K.

We would like to add some comment on the different energy barrier for CH_4 dissociation on these two metal surfaces. In an effort to understand which physical properties of a surface determine its chemical reactivity, Nørskov[88, 89] developed a theoretical model based on the interaction between the metal d-band and the molecular orbitals of the adsorbing molecules. In particular, he proposed that the particular electronic configuration of the Pt surface, with the center of the d-band closer to the Fermi level energy, would explain the higher reactivity of platinum with respect to nickel, copper and gold. We speculate on the possibility that the favorable electronic structure of Pt may possibly be at the origin of the observed lower energy barrier for the CH_4 dissociation on this metal.

In addition to the much lower ground-state methane reactivity on Ni(111) as compared to Pt(111), we also observe a much greater reactivity increase on Ni(111) than on Pt(111) upon $2\nu_3$

excitation. At the low reaction probability of $S_0 \approx 2 \times 10^{-6}$, where the reaction is still "starved for energy" on both surfaces, the addition of 72 kJ/mol of $2v_3$ vibrational energy increases the reactivity to only 5×10^{-4} for the lower barrier system $CH_4/Pt(111)$, while for the higher barrier system $CH_4/Ni(111)$ the reactivity increases to 1×10^{-2}.

This difference in the degree of vibrational activation between Ni(111) and Pt(111) is also reflected in their different vibrational efficacies η_{2v_3}. In Figure 3.8, we have indicated the $2v_3$ efficacies for the two surfaces, calculated at incident energies where we measure similar laser-off reactivities, of the order of 3×10^{-6} for both surfaces.

The stronger effect of $2v_3$ excitation on Ni(111) is reflected by a higher efficacy $\eta_{2v_3}^{Ni(111)} = 0.65$, nearly twice the value for Pt(111), $\eta_{2v_3}^{Pt(111)} = 0.39$. Such an increased vibrational efficacy is typically associated with a "late" barrier on the reactions potential energy surface (PES) according to the well known Polanyi rules [12] and corresponds to a transition state structure for which the dissociating bond is significantly stretched at the transition state. The presence of a late barrier in the PES is confirmed by a recent *ab initio* calculations performed by Nave and Jackson [90] (Figure 3.10), who have also investigated the local distortion of the surface lattice at the transition state and the role of surface harmonic oscillation in lowering the effective barrier to dissociation.
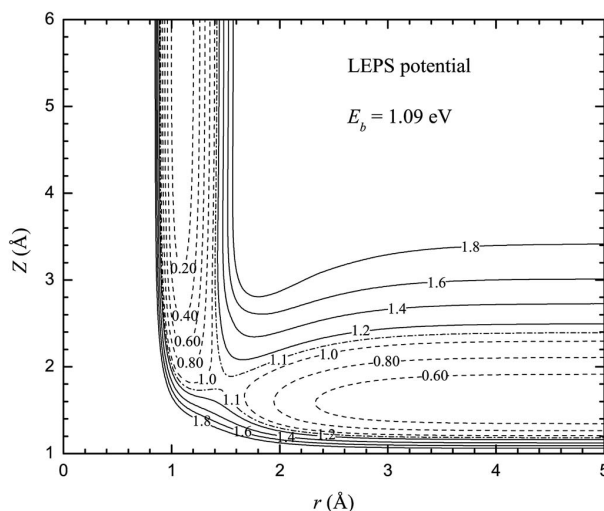
Figure 3.10 Nave *et al.*[90], London-Eyring-Polanyi-Sato (LEPS) contour plot of the potential $V_0(Z, r)$ of the dissociative chemisorption of CH_4 on Ni(111) surface. Energy contours are in eV. The transition state is located at $Z = 1.82$ Å, $r = 1.47$ Å, $E_{TS} = 1.087$ eV.

Calculated transition state structures are consistent with this interpretation and predict the methane molecule on the top site above a surface metal atom for both Pt(111) and Ni(111), but with the reactive C-H bond more elongated on Ni(111)[83, 85, 91, 92] than on Pt(111)[75, 85]. The proposed difference in barrier location (later on Ni(111) than on Pt(111)) is also consistent with previous results reported by Luntz and Bethune[67], who reported an averaged vibrational efficiency β_v (where $\beta_v = \partial\left(Ln(S_0)\right)\big/\partial\left(\langle Ev\rangle\right)$) of all thermally populated states in a hot nozzle beam to be 4 times higher for Ni(111) than for Pt(111).

3.7 Summary

We measured the state-resolved sticking probability of methane excited to the $\nu_1+\nu_4$ and $2\nu_3$ state on the Pt(111) surface. A very similar reactivity enhancement with respect to ground state molecules is observed upon excitation of the $\nu_1+\nu_4$ and the $2\nu_3$ states, although the last vibration contains ~40% more energy.

The different efficacies of these vibrational states is inconsistent with the predictions of the PC-MURT model proposed by the group of Harrison[38, 45, 74, 76-79], since in this statistical model it is assumed that complete IVR occurs upon impact with the surface. On the contrary, our results show that memory of the initially excited state is preserved until the molecules reach the transition state.

Vibrationally adiabatic calculations[30] predict a larger increase in reactivity upon excitation of the symmetric stretch vibration compared to the antisymmetric stretch. In particular, they suggest that the ν_1 mode adiabatically correlates with the localized excitation in the unique C-H bond pointing towards the surface. Conversely, the ν_3 vibration correlates to a state where the vibrational energy is quarantined in the three C-H bonds pointing outwards the surface.

Similarly, wave packet simulations performed by Milot *et al.*[37, 81, 82] suggest that initial vibrational excitation of methane asymmetric ν_3 stretch will enhance the dissociation, but that the excitation of the ν_1 symmetric stretch mode will be more effective.

We observe that the qualitative predictions of both the "*dynamic*" models proposed by Halonen *et al.*[30] and by Milot *et al.*[37, 81, 82] are in qualitative agreement with our results, since we measured a much higher vibrational efficacy for the $\nu_1+\nu_4$ state, containing one quantum of symmetric stretch vibration, compared to the $2\nu_3$ state.

Alternatively, we could suggest that the higher efficacy of the $\nu_1+\nu_4$ state is consistent with a transition state structure in which the breaking C-H bond is at the same time stretched and bent. This conjecture is partially confirmed by Psofogiannakis *et al.*, since they indicate that the real reaction coordinate is "*not very well represented*" by a pure C-H elongation[75].

Chapter 4: State-resolved reactivity of CH_4 on Pt(110)-(1×2)

4.1 Outline

This Chapter is structured in three parts. In the first part (sections 4.1 and 4.2), I summarize the previous experimental results on the activated chemisorption of CH_4 on Pt(110)-(1×2). In the second part (sections 4.4 and 4.5), I describe our state-resolved S_0 measurements for ground state and vibrationally excited CH_4. In the last part (section 4.6), I show how we have changed the polar and azimuthal angles of incidence to measure the reaction probability on select surface sites.

4.2 Introduction and previous results

In early bulb experiments, where there is thermal equilibrium between the surface and the gas phase molecules, Luntz *et al.*[93] and Sun *et al.*[94] observed that the adsorption probability of methane on Pt(110) strongly increases with surface temperature.

Two previous molecular-beam studies [95-98] reported that, for $E_t > 10$ kJ/mol, CH_4 chemisorbs dissociatively on Pt(110)-(1×2) via a direct-activated process in which the translational energy of the incident molecules contributes to overcome the reaction barrier. In addition, for lower translational energy ($E_t < 10$ kJ/mol), Walker and coworkers observed that CH_4 adsorbs via a precursor-mediated mechanism in which increasing E_t decreases the reaction probability.

McMaster *et al.*[95] applied supersonic molecular-beam techniques to measure the sticking probability of CH_4 as a function of incident translational and vibrational energy. They found that

71

the chemisorption of methane is activated by the translational energy and estimated an average reaction barrier of 123 kJ/mol. They probed the effect of vibrational energy by increasing the nozzle temperature of the beam source from 610 to 800 K and found that, within the limits of their experimental error, the vibrational energy did not affect significantly the reaction probability. They also observed that increasing the surface temperature from 500 to 900 K did not influence the sticking probability. McMaster and Madix have also investigated how the initial sticking probability of methane changes as a function of the incident polar angle θ, for two different azimuthal orientations. When they positioned the surface such that the tangential velocity component of the beam was incident along the atomic rows, the dissociation of methane exhibited normal energy scaling. When the azimuthal orientation was rotated 90°, such that the tangential velocity component of the beam was directed perpendicular to the atomic rows, the initial dissociation probabilities of methane exhibited less than normal energy scaling.

They suggested that, when the molecules hit perpendicularly the atomic rows on the surface, the parallel component of the molecular momentum contributes to the chemisorption. They failed to rationalize the observed different reactivity of the two azimuthal orientations in terms of local-normal energy scaling.

Walker and King [97] performed a series of molecular-beam experiments in which they investigated the role of translational and vibrational energy in promoting the adsorption. They controlled the energy of the CH_4 in two ways: by seeding methane in different carrier gases at constant nozzle temperature, they could change the incident translational energy of CH_4 without varying the internal energy of the molecules and by changing the nozzle temperature they altered both the translational and the internal energy of methane. Figure 4.1 shows the variation of S_0 with incident translational energy E_t in the range 20 E_t 680 meV and at nozzle temperature T_n varying between 300 T_n 800 K at a surface temperature of 400 K.
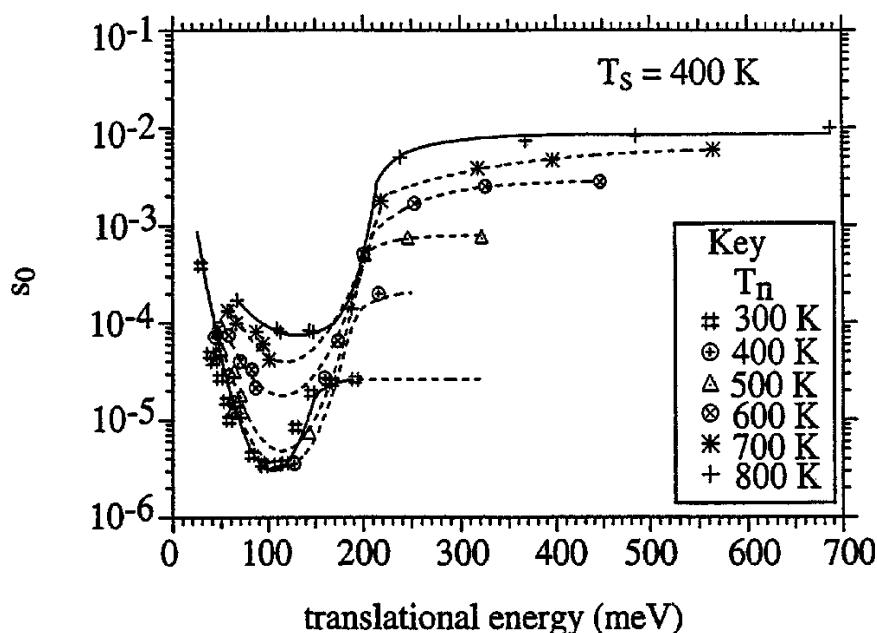
Figure 4.1 Dependence of S_0 on incident translational energy for methane dissociative adsorption on Pt(110)-(1×2) at T_s = 400 K, normal incidence, 20<E_t<680 meV, 300<T_n<800 K.[97]

At E_t > 100 meV, S_0 rises sharply with increasing translational energy, a behavior normally associated with a direct-dissociation channel. From their data, Walker and coworkers estimate an activation energy for the dissociation of CH_4 on Pt(110) of 21 kJ/mol, at T_n = 300K, T_s = 400K.

At low incident energy, E_t < 100 meV, S_0 decreases with increasing translational energy. Such behavior is indicative of a precursor-mediated adsorption mechanism, where the methane molecules are trapped into a weakly bound precursor state before dissociating or desorbing. Seets *et al.* reported similar observations for methane adsorption on Ir(111)[99] and Ir(110)[100, 101] at low kinetic energy (E_t < 15 kJ/mol). Walker and King observed that vibrational energy, provided to the molecules by increasing the nozzle temperature from 300 K to 800 K, enhances the reaction probability over the full E_t range investigated. In summary, there are only two previously attempts to investigate the effect of vibrational energy for CH_4 chemisorption on Pt(110) with controversial results: McMaster could not measure any appreciable vibrational enhancement, but Walker observed an increase (up to 30 fold) in the sticking coefficient as the nozzle temperature was varied from 300 to 800 K. For this reason, the initial goal for our Pt(110) state-resolved reactivity measurements was to test the effect of vibrational excitation over a wide range of translational energies.

73

4.3 The Pt(110)-(1×2) surface

The structures of the reconstructed (110) surfaces of Pt has been object of considerable debate because the (1×2) reconstruction, observed with LEED, RBS and other surface diffraction techniques, can be explained by two theoretical models of the surface, called "missing row" and "sawtooth" geometries[102, 103].

Recently, several theoretical[103-106] and experimental[107-111] studies clarified that the Pt(110)-(1×2) surface (Figure 4.2) has a missing row structure in which alternate rows of closed-packed atoms in the top atomic layer are missing [106, 112].

(a)   **(b)**
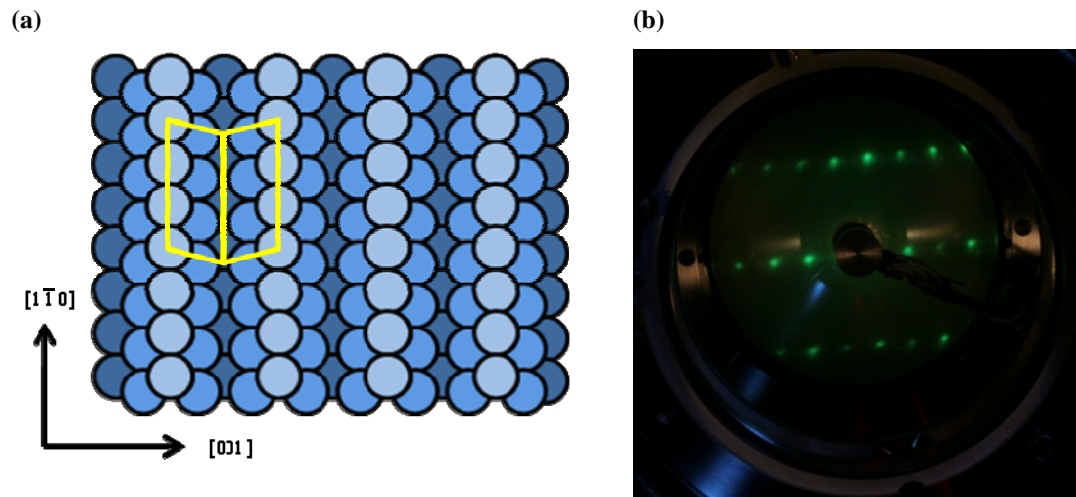
Figure 4.2 (a) Schematic illustration of the Pt(110)-(1×2) surface. The different colors are used to indicate the top first, second and third layer of Pt atoms. The yellow lines indicates the orientation of the (111) and (11$\bar{1}$) microfacets; **(b)** LEED pattern of the Pt(110)-(1×2) surface after ion-sputtering and annealing.

When viewed in the surface plane along the [1$\bar{1}$0] direction (Figure 4.3), the surface appears as a series of troughs consisting of (111) and (11$\bar{1}$) planes, with a three atomic-rows periodicity along the [001] direction.
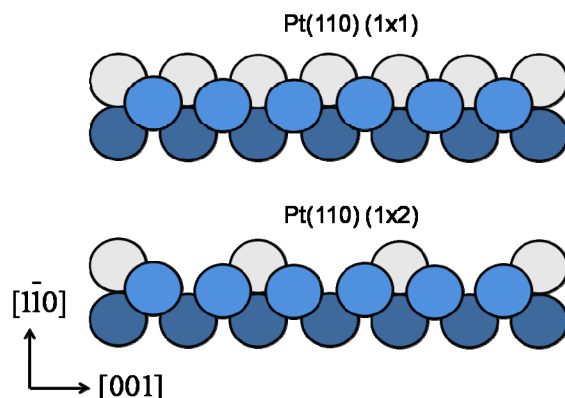
Figure 4.3 Cross-sectional view of the Pt(110) (1x1) unreconstructed surface and of the Pt(110)-(1×2) reconstructed surface.

The (111) microfacets on Pt(110)-(1×2) surface are tilted approximately 35° from the surface normal [109]. At a surface temperature above 1100 K an order-disorder phase transition is reported to occur yielding the (1x1) structure.

4.4   CH$_4$ ground state reactivity on Pt(110)-(1×2)

We performed reactivity measurements for ground state CH$_4$ as a function of the translational energy using timed depositions of molecular beams of well defined E$_t$, and detecting the carbon coverage on the surface with AES. We calibrated the AES signal in terms of C coverage by comparison to King & Wells measurements (see Chapter 2).

The kinetic energy of CH$_4$ molecular beam is determined using the time of flight (TOF) technique. We have varied the speed of the incident molecules preparing mixtures with different carrier gas and concentrations, keeping the nozzle temperature constant (323 K) for all the kinetic energies up to 54 kJ, and only the point at 63 kJ has been measured at higher (373 K) T$_n$. The kinetic energy of CH$_4$ for the different mixtures are shown in Table 4.1.

Table 4.1 Kinetic energy of different CH_4 mixtures in our experiments.

Seed gas (%)	Carrier gas	Nozzle temperature(K)	CH_4 normal energy(kJ/mol)
10	Ar	323	3.9±0.2
100	/	323	9.7±0.3
25	H_2	323	22.4±0.5
12	H_2	323	32.8±0.5
6	H_2	323	40.8±1.9
1	H_2	323	54.0±0.9
1	H_2	373	63.5±1.1

Figure 4.4 shows the laser-off reactivity measurements for CH_4 on Pt(110)-(1×2) as a function of the kinetic energy for normal incidence (E_n) for a surface temperature of 400 K. At the nozzle temperatures used in this experiment (323-373 K), these data represent a close upper limit to the reaction probability for methane molecules in the ground-state (S_0, $v = 0$).

Every S_0 reported in Figure 4.4 is obtained by averaging several measurements and the error bars include contributions from statistical (95% of confidence limit) and calibration errors (details on the error evaluation are given in Chapter 3 of this thesis and in the work of Bisson *et al.*[47]).
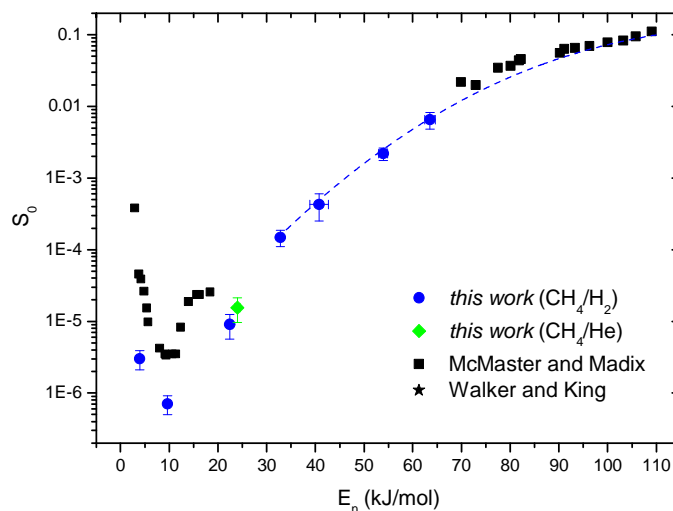
Figure 4.4 Laser-off reactivity of CH_4 on Pt(110)-(1×2) as function of normal kinetic energy (E_n): (●) this work, T_s = 400 K, T_n = 323 – 373 K; (◆) this work, CH_4/He mixture; (★) Walker and King, T_s = 400 K, T_n = 300 K [96]; (■) McMaster and Madix, T_s = 550 K, T_n = 610 – 860 K [95]. The dashed blue curve is a S-curve fitting of our laser-off data from 22 to 63 kJ/mol, the agreement between the experimental data point and the fitting curve is good in this range of kinetic energy since only the direct-adsorption pathway is dominant. The S-curve has been drawn up to 110 kJ/mol to show that our data are in substantial agreement with the data of McMaster and Madix. [95].

We observe a nearly exponential increase of the sticking coefficient with incident translational energy for E_n > 10 kJ/mol, where the reaction probability increases from 7×10^{-7} at E_n = 10 kJ/mol to 6×10^{-3} at E_n = 63 kJ/mol. This strong translational energy dependence of the sticking coefficient indicates that CH_4 reacts with the Pt(110)-(1×2) surface via a direct mechanism, in which the molecule dissociates immediately on impact with the surface. For incident translational energy lower than 10 kJ/mol, we observe an increase in reaction probability in reducing E_n from 10 to 4 kJ/mol. This observation, in agreement with the results reported by Walker and King, confirms the existence of a precursor-mediated adsorption pathway in the kinetic energy range below 10 kJ/mol. For comparison, I have included in Figure 4.4 data obtained in previous molecular-beam studies on methane adsorption on Pt(110)-(1×2) by McMaster [95] and Walker [96].

The data reported by McMaster and Madix have been measured at a surface temperature of 550 K, somewhat higher than the 400 K used in our experiments. Since our measurements and

those of McMaster have been taken in a different E_t range, we cannot compare them directly. Nevertheless, we observe that the two sets of data follow the same trend and can be fitted by a common S-curve. For $E_n < 20$ kJ/mol, we observe reactivities which are about one order of magnitude lower than those reported by Walker *et al.* This discrepancy is perhaps due to the fact that Walker and coworkers have used a single crystal surface with 1° miscut from the (110) plane[97], 10 times higher than the miscut of our Pt(110) sample (0.1° from the (110) plane). Since the step density on surface scales with the miscut angle and since all measurements performed by Walker *et al.* have been done at very low coverage (< 1% ML[97]) it is conceivable their measurement may be influenced by reactivity on the step sites. It is well known [47] that the reactivity at step edges and kink sites is significantly higher than that on terraces.

I chose to perform the reactivity measurements at a surface temperature of 400 K because it is well above the desorption temperature of H_2 (260-310 K) from Pt(110)-(1×2), as reported by several authors[113, 114], and it is sufficiently low to exclude significant carbon diffusion effects. Furthermore, with this choice of surface temperature, we can compare our results with previously published molecular beam experiments by Walker *et al.* and McMaster *et al.*, that were performed at similar temperature, 400 K and 550 K respectively (Figure 4.4). In order to exclude H passivation of the surface in our experiments as a possible reason for the discrepancy between the reactivities measured in our work and that of Walker, I compared the reactivity of a pulsed beam of 25% CH_4 in H_2 to that of a beam of 3% CH_4 in He at identical nozzle temperature and at very similar kinetic energies (22 and 24 kJ/mol) and detected no significant difference in reactivity (9×10^{-6} and 1.5×10^{-5}).

4.5 Reactivity of vibrationally excited CH₄ on Pt(110)-(1×2)

4.5.1 Introduction

In this section, I will describe the results of our quantum state resolved sticking measurements of CH_4 on the Pt(110)-(1×2) surface for several vibrationally excited states. Using a tunable pulsed infrared laser setup, we have excited CH_4 to the vibrational states $2\nu_3$, $\nu_1+\nu_4$ and $2\nu_2+\nu_4$, which according to the discussion given in Chapter 2, correspond to a C-H stretch overtone, stretch-bend combination, and a bending overtone band, respectively. All the state-selected measurements are performed by exciting the R(1) ro-vibrational transition which populates a level with rotational angular momentum quantum number J = 2. We checked that the excitation of all three vibrational states is saturated by recording saturation curves (reported in Figures 2.14, 2.15 and 2.16). In these series of experiments, the exposure time varies from a few minutes at high translational energy (E_t = 63 kJ/mol) to several hours at $E_t \leq$ 10 kJ/mol.

The goal of these measurements is to probe the role of methane vibrations on its chemisorption reaction on Pt(110). In particular, we want to test for mode specificity in this gas-surface reaction by comparing the state resolved reactivity of several nearly isoenergetic vibrational quantum state of CH_4. Our measurements are important because they constitute a stringent test of available theoretical models for methane chemisorption such as the MURT model developed by Harrison *et al.*[74, 76, 78, 79] which was claimed to be consistent with all previous thermally average reactivity measurements using molecular beam as well as bulb methods.

4.5.2 Results and discussion

Our measurements of the sticking coefficient of CH_4 on Pt(110)-(1×2) without laser excitation (methane in the vibrational ground state), and upon excitation of the $2\nu_3$, $\nu_1+\nu_4$ and $2\nu_2+\nu_4$ states, are shown in Figure 4.5 as function of incident translation energy E_n at normal incidence.
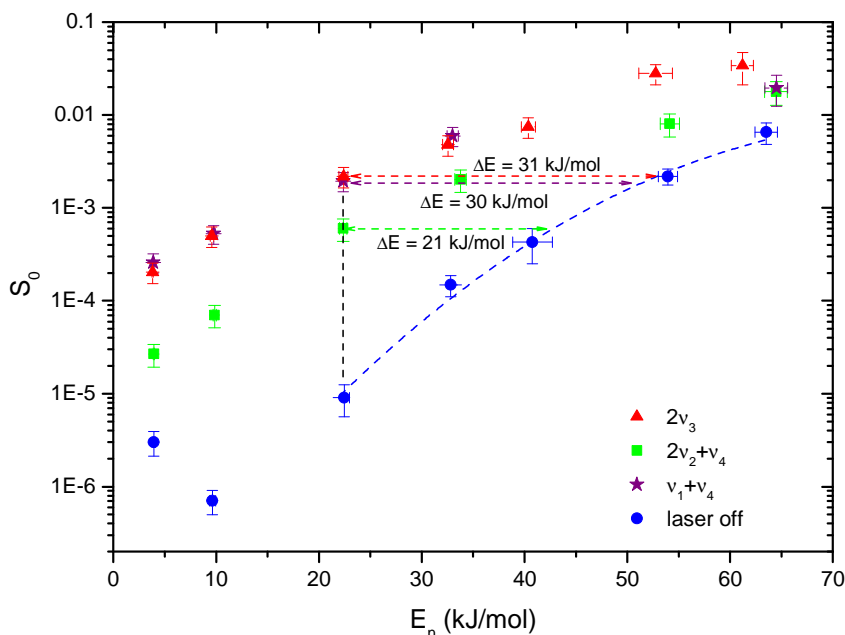
Figure 4.5 Sticking coefficients as a function of incident kinetic energy (normal incidence) for dissociative chemisorption of CH_4 on Pt(110)-(1×2) (T_s = 400K). (▲) $2\nu_3$, (■) $2\nu_2+\nu_4$, (★) $\nu_1+\nu_4$, (●) laser-off data. The horizontal dashed arrows indicate the amount of normal kinetic energy which produces the same increase in reactivity as the vibrational excitation. The dashed blue curve is an S-curve fitting of our laser-off data from 22 to 64 kJ/mol used to interpolate between the data points.

Our measurements show that, in the E_t range investigated, vibrational excitation enhances the dissociation probability of methane on Pt(110)-(1×2). The reactivity enhancement relative to the ground state varies considerably with the incident kinetic energy. For example, at E_n = 33 kJ/mol, the sticking coefficient of the $2\nu_3$ and $\nu_1+\nu_4$ state is ~30 times higher than the correspondent laser-off measurement, while, at 10 kJ/mol, we observe an enhancement of the reaction probability of up to 3 orders of magnitude. Within the kinetic energy range used for our measurements, we observe that the excitation of the modes $2\nu_3$ and $\nu_1+\nu_4$ produces the same increase in reaction probability. To compare the effect of the vibrational and translational energy on the reaction probability, we measured how much translational energy in the ground state produces the same increase in the reactivity as the vibrational excitation (horizontal dashed lines in Figure 4.5). For the $2\nu_3$ and $\nu_1+\nu_4$ excitation, we estimate that ~30 kJ/mol of kinetic energy

80

added to the ground state, at $S_0 = 9\times10^{-6}$, brings its reactivity to the same level of the excited vibrational states. However, since these two modes have different energies (71.4 kJ for the $2\nu_3$ mode, and 50.5 kJ for the mode $\nu_1+\nu_4$), the $\nu_1+\nu_4$ state has 40% higher efficacy than the $2\nu_3$ mode (Table 4.2).

Table 4.2 The vibrational efficacy[34] (equation 3.1) is a parameter that compare the effect of vibrational and translational energy on the reaction probability. The vibrational efficacies of the different states on Pt(110) are calculated at kinetic energy of 22 kJ/mol, where we measured the maximum vibrational enhancement.

State	*Vibrational Energy (kJ/mol)*	*Vibrational Efficacy*
$2\nu_3$	71.4	43%
$2\nu_2+\nu_4$	52.2	39%
$\nu_1+\nu_4$	50.5	59%

   We can see that for all the three vibrational states we have excited in this work, the vibrational energy is not as effective as the translational energy in promoting the dissociation of CH_4 on Pt(110). As Higgins *et al.*[31] and Schmid *et al.*[32] pointed out, a vibrational efficacy lower than unity is inconsistent with statistical model of the reaction mechanism. We also measured a factor of 7 difference in reactivity between the nearly isoenergetic $\nu_1+\nu_4$ and $2\nu_2+\nu_4$ states. This is an indication that the chemisorption of CH_4 on Pt(110) is "state-specific"[6, 36]. Our results confirm in part the results of the theoretical studies of Milot and Jansen[37, 81, 82]. Milot et al. applied nine-dimensional wavepacket simulations to investigate the role of the vibrational excitation in the scattering of CH_4 from a flat metal surface, and found that initial vibrational excitation in CH_4 increases the dissociation probability, with the largest enhancement associated to excitation of C-H stretching motion, in particular in the symmetric mode ν_1. We can also exclude that the role of the vibrational activation of methane on Pt(110) reaction could be explained by a simple "deformation model" mechanism, as the one proposed by Lee *et al.* [84, 115] because in that case the pure bending vibrational state $2\nu_2+\nu_4$ would have a higher efficacy than the $\nu_1+\nu_4$ state.

81

Anghel and coworkers reported a theoretical study on the mechanism of CH_4 chemisorption on Pt(110)-(1×2) [116]. They modeled the surface with a six-layer Pt slab and obtained the transition state energy and geometry using hybrid eigenvector-following method with variational eigenvector refinement and tangent space minimization[116]. At the transition state, the carbon atom of methane is located over the Pt(110)-(1×2) ridge atop atom site (Figure 4.6 a). They calculated an energy barrier of 40 kJ/mol for the lower energy pathway. Upon dissociation, the resulting CH_3 moiety was also found to reside preferentially at the ridge atop site. They found that the location of the H atom immediately after dissociation can be either onto the bridge site between two ridge atoms or onto the bridge site between a ridge atom and a second-layer atom, but they found that the reaction barrier is independent by adsorption site of the dissociated H atom[116].

(a)   **(b)**
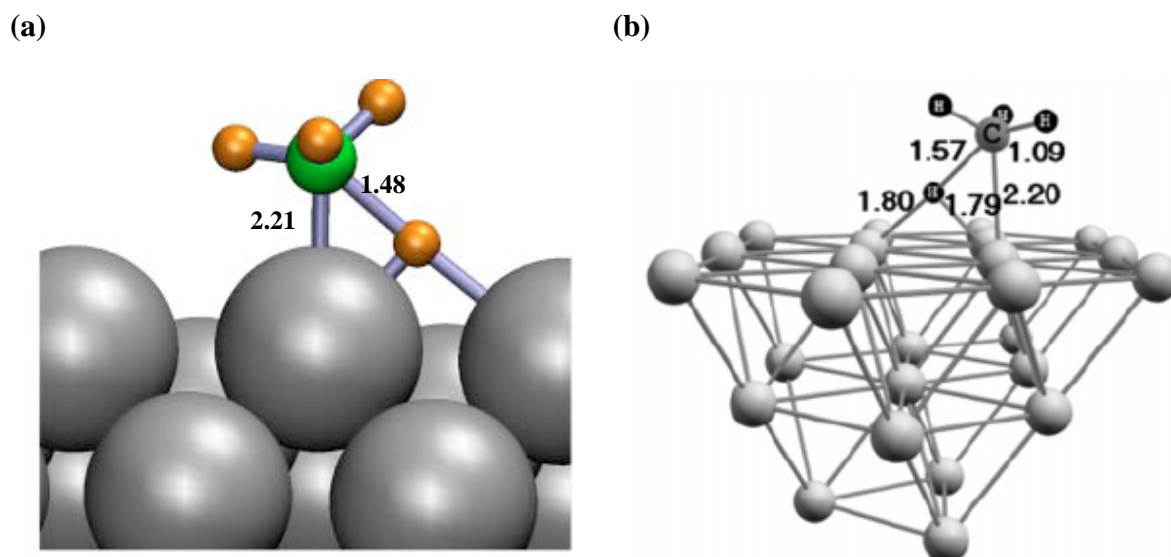
Figure 4.6 (a) CH_4 TS structure on six layers Pt slab that models the Pt(110)-(1×2) surface (Anghel *et al.*[116]). **(b)** TS structure on Pt(111) calculated by DFT with B3LYP functional. A Pt_{25} cluster serves as model of the real Pt(111) surface. (Psofogiannakis *et al* [75]). Bonds lengths and distances in the figures are in Å.

It was found that the transition state structure for the dissociation of methane on Pt(110)-(1×2) involves simultaneous stretch and bend of the breaking C-H bond. In our experiments we observed that the $\nu_1+\nu_4$ state has higher efficacy than both the $2\nu_2+\nu_4$ and $2\nu_3$ states, hence, our

82

results confirm that, at the TS, the dissociating C-H bond is at the same time elongated and bent with respect to its equilibrium geometry.

4.5.3 Vibrational activation in the precursor-mediated pathway region

Vibrational excitation of methane enhances the reaction probability over the entire kinetic energy range investigated in this study (4 kJ/mol<E_n<63 kJ/mol). However, the presence of a precursor-mediated reaction pathway at low kinetic energy (E_n < 10 kJ/mol) is not visible in the excited state curves, since the reactivity of the vibrationally excited molecules always decreases as the translational energy is decreased.

We suggest that at E_n = 4 kJ/mol both reaction pathways are possible: the direct activated and the precursor mediated. At E_n = 4 kJ/mol, we estimate that 90% of the ground state reactivity can be accounted for by a precursor mediated mechanism. This estimation is based on the difference between the observed $S_0(E_n = 4$ kJ/mol$) = 3\times10^{-6}$ and the extrapolation of the reactivity at this kinetic energy if only the direct chemisorption mechanism were present $S_{0,direct} = 2\times10^{-7}$. For calculating the last quantity we fit the sticking coefficient of the v = 0 molecules from E_n = 10 to 63 kJ/mol with a "S-curve" and extrapolate the result of the fitting to 4 kJ/mol (Figure 4.7).

Conversely, the sticking coefficient of the vibrationally excited molecules at 4 kJ/mol is close to the prolongation to the "S-curve" fitting of the laser-on points measured at higher kinetic energies, where the direct adsorption is dominating (Figure 4.7). We therefore suggest that, at this translational energy, the vibrational excitation increases the probability of the molecules to dissociate via a direct adsorption mechanism and does not enhance significantly the probability of precursor mediated chemisorption.

The lifetimes of excited vibrational states of physisorbed CH_4 have not been measured, but for CO on Pt(111) the vibrational lifetimes are ~2 ps. This extremely short vibrational lifetime is probably due to efficient electron-hole pair generation[117]. In the case of methane on Pt(110), the lifetime of the CH_4 molecular precursor-state on the Pt surface has been estimated by Walker and King [96] from the depth of the physisorbed well (~20 kJ/mol[97]) to be ~10 ps at T_s = 400 K. Since the time-scale of the vibrational relaxation on a metal surface is comparable with the lifetime of the physisorbed molecules, we suggest that the initially excited molecules undergo partial or complete relaxation when they are trapped in the physisorption well prior to

dissociation. Therefore we suggest that the vibrational excitation of methane in the gas phase does not affect the precursor mediated chemisorption probability. By contrast, for the chemisorption of SiH_4 on $Si(100)$, it was found that vibrational excitation enhances the reaction probability also in the precursor mediated pathway[41]. This result was explained by the fact that semiconductors have a finite band-gap (for Si ~1.12 eV) that prevents efficient e-h pair generation, therefore the lifetime of the vibrationally excited SiH_4 on $Si(100)$ is longer than the physisorbed precursor lifetime.
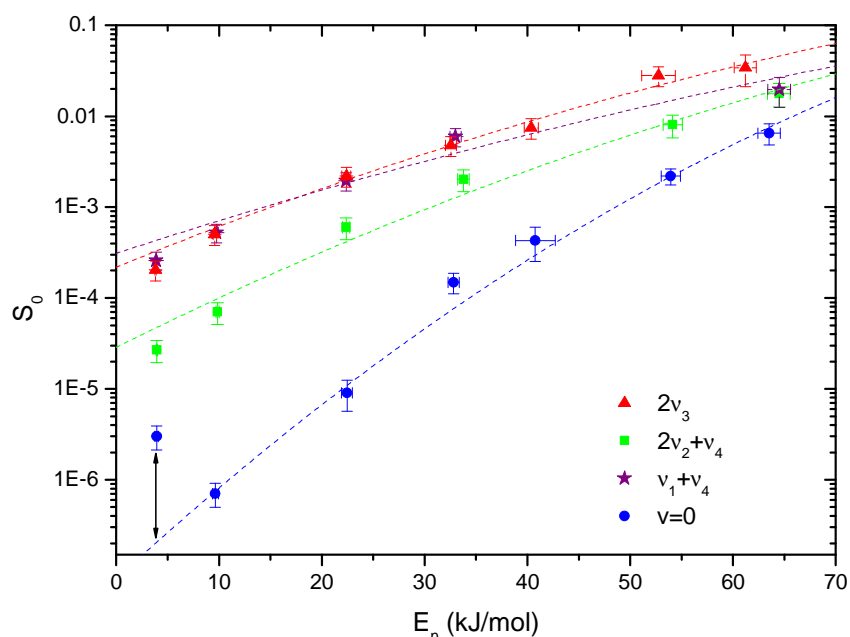
Figure 4.7 Sticking coefficients as a function of incident kinetic energy (normal incidence) for dissociative chemisorption of CH_4 on $Pt(110)$-(1×2) ($T_s = 400K$). ($\bullet$) v=0, ($\blacktriangle$) $2\nu_3$, ($\star$) $\nu_1+\nu_4$, ($\blacksquare$) $2\nu_2+\nu_4$. The vertical black arrow is an estimation of the increase in reactivity due to the presence of the precursor mediated mechanism at low translational energy. The dashed curves are "S-curve" fitting of our laser-on and laser-off (v=0) data from 10 to 64 kJ/mol prolonged to $E_n = 4$ kJ/mol.

4.5.4 CH$_4$ reactivity on the (110) and (111) surfaces of Platinum

Now I will compare our reactivity measurements of ground-state and excited-state methane on the Pt(110) and Pt(111) surfaces (Figures 4.8).
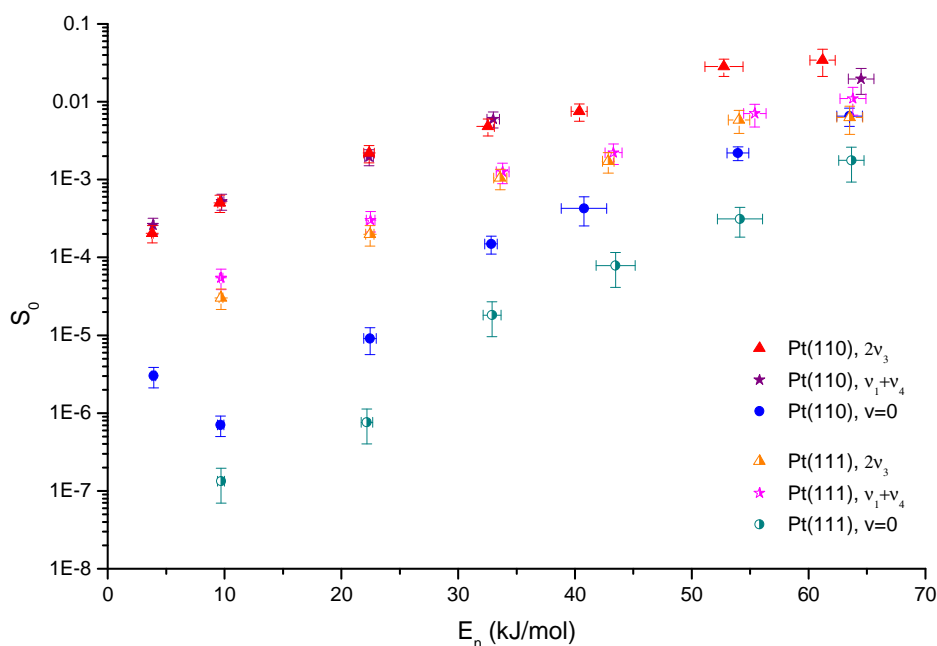
Figure 4.8 Comparison of the $2\nu_3$, $\nu_1+\nu_4$ and laser-off reactivity for Pt(111) and Pt(110)-(1×2) at T$_s$ = 400 K: (★) $\nu_1+\nu_4$, Pt(110); (▲) $2\nu_3$, Pt(110); (●) v = 0, Pt(110); (★) $\nu_1+\nu_4$, Pt(111); (△) $2\nu_3$, Pt(111); (◐) v = 0, Pt(111). The sticking coefficients of the two data-set were recorded at different T$_s$ (400 K for Pt(110) and 600 K for Pt(111)). We have used the T$_s$ dependence of Luntz *et al.* to correct for the higher T$_s$ of the Pt(111) data and extrapolate the reactivity at 400 K.

These two data-set were recorded at different surface temperatures (400 K for Pt(110) and 600 K for Pt(111)). In order to facilitate a direct comparison between the reactivity of methane on the two surfaces, in Figure 4.8 we have corrected that Pt(111) data-set using the temperature dependence of S$_0$ reported by Luntz *et al.*[67]. We observe that, over all the kinetic energy range investigated, the reactivity of ground-state methane on Pt(110) is about 5 times higher than on the Pt(111) surface.

The different reactivity of the two surfaces can be rationalized by analyzing their structure. The Pt(110) surface has a missing row reconstruction and the atop atoms on the rows are less coordinate than the second and third layer atoms. On the contrary, the Pt(111) surface is "flat" and densely packed, on this surface every atom has the same coordination number (CN = 9). Since it is well known that small Pt nano-clusters and Pt step sites have higher reactivity at the terrace atoms[31, 118], we suggest that the higher reactivity of the Pt(110) surface is consistent with the presence of low coordinated, highly reactive, atop atoms.

We compare now how the vibrational excitation of CH_4 affects its reactivity on these two surfaces. For both surfaces, we observe that the excitation of the $\nu_1+\nu_4$ and $2\nu_3$ states provides similar enhancement relative to the CH_4 ground-state reactivity. Furthermore, the vibrational efficacies (Table 4.2) of the $\nu_1+\nu_4$ and $2\nu_3$ states on Pt(110) are similar to what we have observed for the less corrugated Pt(111) surface ($\eta_{2\nu_3}^{Pt(111)} = 39\%$, $\eta_{\nu_1+\nu_4}^{Pt(111)} = 60\%$). This result points to a similarity in the transition state geometry of methane on these two surfaces. Comparison between the CH_4 TS structures on Pt(111) and on Pt(110) shows that the dissociating bond is similarly stretched and bent in the TS configuration, with the leaving H atom onto the bridge position between two adjacent Pt atoms (Figure 4.6). In our measurements we found the highest vibrational efficacy is obtained for the excitation of a stretch-bend vibration ($\nu_1+\nu_4$ state). Our results confirm that, at the TS, the dissociating C-H bond is at the same time elongated and bent with respect to its equilibrium geometry.

4.5.5 Conclusions

In conclusion, we show that our studies produce useful experimental information about the structure of the transition state for methane chemisorption on Pt(110)-(1×2)[116]. In particular, we found that the difference in reactivity between the $\nu_1+\nu_4$ and the $2\nu_2+\nu_4$ vibrational state implies that the C-H bond stretch has a substantial projection on the reaction coordinate.

Furthermore, our results have important implications for the theoretical treatment of the gas/surface process since "state-specific" reactivity is not consistent with statistical models of chemisorptions as the one proposed by the group of Harrison. In fact, in their MURT model,

Bukosky *et al.*[74, 78, 79] assume complete intramolecular redistribution of the initial vibrational energy as the CH_4 molecule temporarily resides in a local "hot precursor state" close to the surface. This model predicts a reactivity that scales with the total available energy, independent of the vibrational state excited, which is not consistent with our experimental observations. In contrast to the assumptions of the statistical models, our results show that the CH_4 reactivity clearly depends on the initially excited vibrational state and that its interaction with the surface does not cause complete intramolecular energy redistribution (IVR) before the reaction occurs. We can roughly estimate that a CH_4 molecule approaching the Pt(110) surface with a speed of 2000 m/s will travel 100 fs to fly through the interaction region (about 2Å). Our results show that the IVR does not occur on a timescale of 100 fs.

The similar efficacies of the $\nu_1+\nu_4$ and $2\nu_3$ states on the Pt(110) and Pt(111) suggest similarity in the CH_4 TS structure upon these surfaces. *Ab initio* calculations, performed by Psofogiannakis *et al.*[75] and Anghel *et al.* [116], confirm this hypothesis.

4.6 Angle dependence of the CH_4 reactivity on Pt(110)-(1×2)

4.6.1 Introduction

Angular dependent scattering and reactivity measurements yield information on the gas/surface potential energy surface[7, 119]. For example, Dürr and Höfer[120] have measured the dissociation probability of H_2 on Si(001) as a function of both polar and azimuthal angle of incidence. They find a strong angle dependence of the H_2 reaction on Si(001), which depends if the incident H_2 approaches parallel or perpendicular to the silicon dimer dangling bonds. For the same polar angle, the sticking coefficient is higher when the molecules hit the surface along the direction of the dangling bonds[120]. In this work, we measured the initial sticking coefficient of CH_4 on Pt(110)-(1x2) as a function of the polar angle (θ) and the azimuthal angle (φ) of incidence. As I will discuss in the next section, shadowing effects, caused by the highly corrugated structure of Pt(110) surface, allow us to obtain site specific information on the

chemisorption probability. In this introductive part I will describe how we performed the angular dependence measurement and how the azimuthal angle and polar angle of incidence are defined.

The polar angle is measured with respect to the surface normal as shown in Figure 4.9, and was varied from $0°$ to $70°$. The azimuthal angle is measured with respect to the missing row direction of the surface. Two azimuthal orientations of $\varphi = 0$ and $90°$ have been studied. For $\varphi = 0$ the molecular beam is incident parallel to the missing-rows and therefore parallel to the main corrugation of the surface (// orientation). For $\varphi = 90°$, the molecular beam is incident perpendicular to the missing rows ($\perp$ orientation) and shadowing effects due to the corrugation of the surface can be expected when θ is increased. The polar angle θ was varied by rotating the crystal about the $[1\bar{1}0]$ (for $\varphi = 90°$) or $[001]$ direction (for $\varphi = 0°$). The azimuthal angle was changed remounting the crystal to its support and checking the alignment with LEED. The azimuthal alignment was measured to be $\pm 5°$.
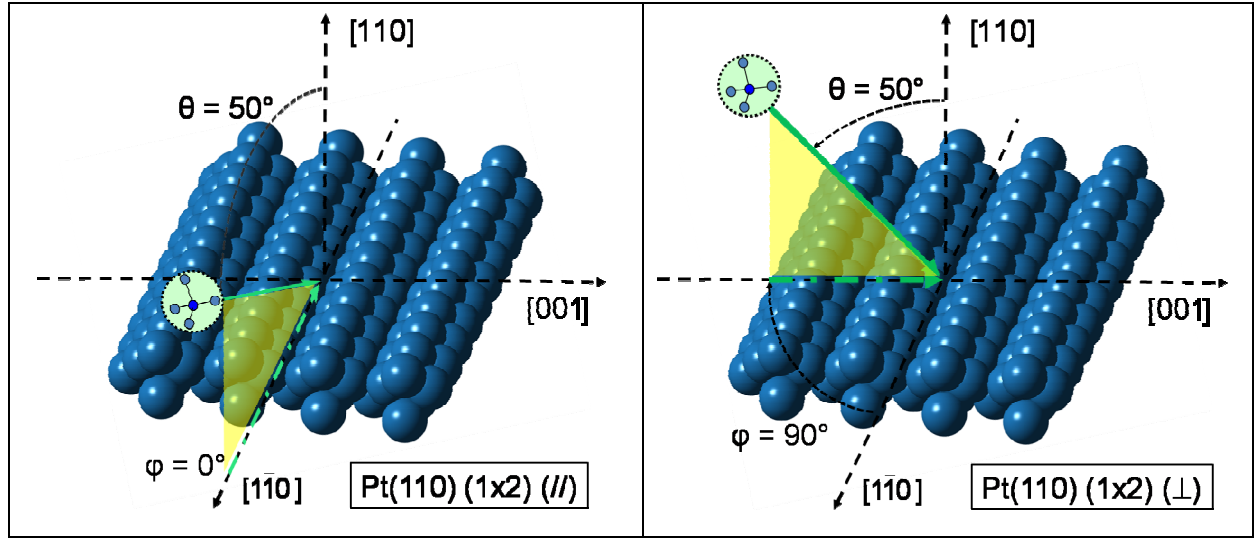
Figure 4.9 Schematic illustration of the Pt(110)-(1×2) surface at the azimuthal orientations used in our experiments. For beams incident on the Pt(110)-(1×2) (//), the molecular beam strikes the surface parallel to the $[1\bar{1}0]$ atomic rows as the polar angle θ is increased. For Pt(110)-(1×2) (⊥), the molecular beam is incident to the surface in the plane given by the direction [110] and [001], transversally to the missing atoms troughs that cross the surface. The azimuthal angle φ is defined as the angle between the $[1\bar{1}0]$ direction and the projection of the incident direction (indicated in the figure with a green dash-dot line) on the surface plane.

For the determination of the sticking coefficient as a function of angle of incidence > 0° we have to take into account that the molecular beam will react with a surface area A = $f(\theta)$ that increases with the angle of incidence θ. From geometric analysis of the system composed by our molecular beam and the surface (Figure 4.10 a and b), the carbon spot area A can be approximated by the area of an ellipse with a minor axis a = 2 r (where r indicates the radius of the carbon spot) and major axis b, that varies as a function of the angle θ, and it is given by the expression:

$$b \; = \; \frac{a}{\cos(\theta)} = \frac{2\,r}{\cos(\theta)} \quad \textbf{(4.1)}$$

From eq. 4.1 we can calculate the area A of the carbon spot on the surface:

$$A = 4r^2 / \cos(\theta) \qquad \textbf{(4.2)}$$

89
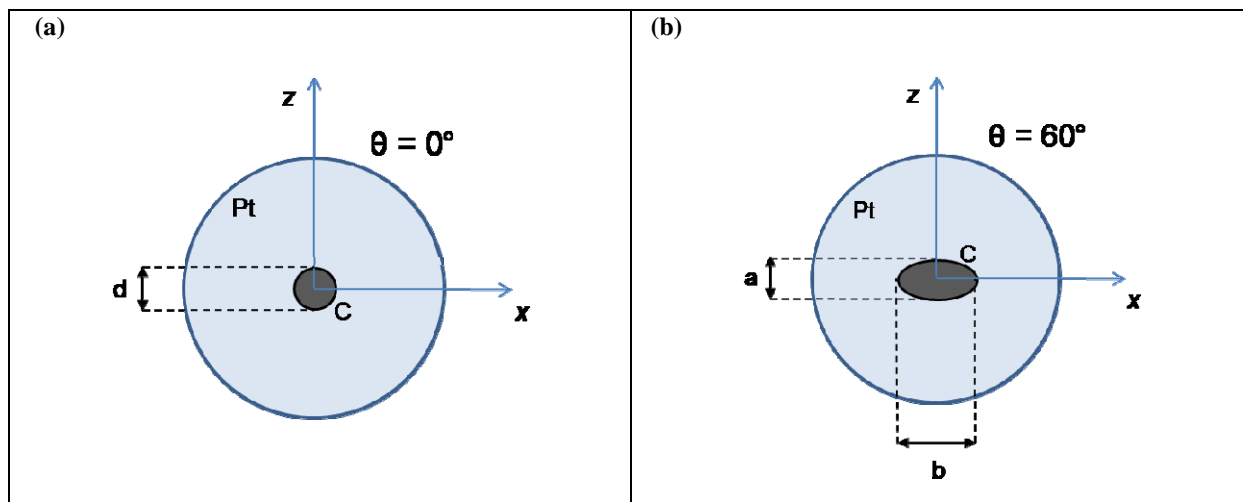
Figure 4.10 Schematic representation of the carbon footprint on the Pt(110)-(1×2) surface after molecular beam deposition at an angle of incidence θ respect to the normal of the surface. x and z indicate the translational coordinate of motion of the crystal manipulator, with respect to the laboratory frame. At the end of the deposition the crystal is rotated towards the Auger spectrometer and the C coverage is measured performing an AES scan of the surface along the x and z directions. **(a)** When the CH_4 molecular beam is incident normally (θ = 0°) to the surface the carbon footprint on the surface is circular, with diameter d. **(b)** the molecular beam is incident to the surface with an angle θ = 60°: the C footprint is elliptical where a and b indicate the minor and major axis of the ellipse.

In order to verify that equation 4.1 can predict the real dimensions of the carbon footprint, we have performed AES scans in the x and z direction along the center of the carbon spot for several depositions at different θ. We found that a (the diameter of the spot in the z direction) does not change as θ is increased. In the x direction, the carbon spot becomes "stretched" as we increase the angle of incidence, and the dimensions a and b are related by equation 4.1. Figure 4.11 shows AES profiles along the x and z directions of a C coverage resulting from a deposition of a 12% CH_4/H_2 mixture at θ = 60° incidence (E_t = 32 kJ/mol). We can see that equation 4.1 well describe the relation between a and b since 3.3 mm ≈ 1.7 mm / cos(60°).
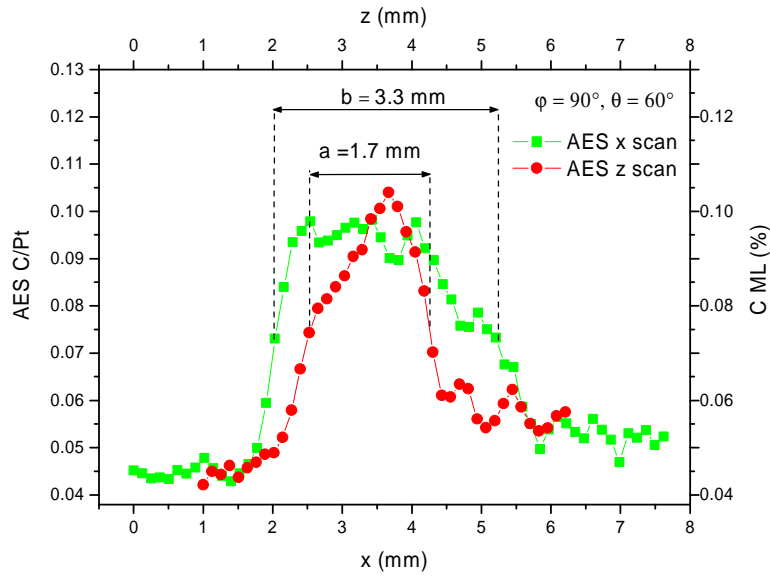
Figure 4.11 AES profiles along the *x* and *z* directions of a C coverage resulting from a deposition at $\theta = 60°$ incidence. $T_s = 400$ K, $E_t = 32$ kJ/mol.

After we have verified that the shape of the carbon spot can be described by an ellipse we can legitimately apply equation 4.2 to calculate the area of the spot when $\theta \geq 0°$.

4.6.2 Experimental results and discussion

4.6.2.1   Test for normal energy scaling

We measured the sticking coefficient of CH_4 in the $v = 0$ and in $2v_3$ state on the Pt(110)-(2x1) as a function of the polar angle (θ) and the azimuthal angle (ϕ) of incidence. We fixed the total incident kinetic energy (32 kJ/mol) and increased the angle of incidence θ. As θ is increased, the component of the translational energy normal to the surface changes. For CH_4 chemisorption on Pt(111)[95], as well as in many other direct activated chemisorption reactions[7], the sticking probability is found to scale with the normal component of the translational energy (normal energy scaling):

$$E_n = E_t \cos^2(\theta) \qquad \textbf{(4.2)}$$

However, in some case (H_2 on Si(100) and H_2 on Fe(110), for example) normal energy scaling is not observed experimentally [7, 119, 120], and the surface corrugation has been suggested to account qualitatively for the non-normal energy scaling . Xia and Engstrom suggested that, for corrugated surfaces, the translational energy should be scaled with respect to the local normal of the surface:

$$E_n = E_t \left[(1-\Delta_1) \cos^2(\theta) + 3\Delta_2 \sin^2(\theta) \right] \qquad \textbf{(4.3)}$$

$$(//)\, E_n = E_t (1-\Delta) \cos^2(\theta) \qquad \textbf{(4.3a)}$$

$$(\perp)\, E_n = E_t \left[(1-\Delta) \cos^2(\theta) + 3\Delta \sin^2(\theta) \right] \qquad \textbf{(4.3b)}$$

where the parameters Δ_1 and Δ_2 ($0 \leq \Delta_1, \Delta_2 \leq 1$) describe the surface corrugation. For the Pt(110)-(1×2) surface they indicated two limiting cases. For incidence parallel to the missing rows $\Delta_2 = 0$, $\Delta_1 = \Delta$ and equation 4.3a reduces to eq. 4.3a. For incidence perpendicular to the rows $\Delta_1 = \Delta_2 = \Delta$ and equation 4.3 can be written as eq. 4.3b. For Pt(110) Xia *et al.* [121] reported $\Delta = 0.178$.

In order to test for normal energy scaling in the CH_4 chemisorption on Pt(110), we have applied equation 4.2 to scale the S_0 measurements obtained at angle of incidence $\theta > 0°$. If the scaled S_0 points fall on the same trend line of the normal incidence measurements than it means that the CH_4 chemisorption on Pt(110) follows normal energy scaling. In Figure 4.12 we report both series of data obtained with $\theta > 0°$ and $\theta = 0°$.
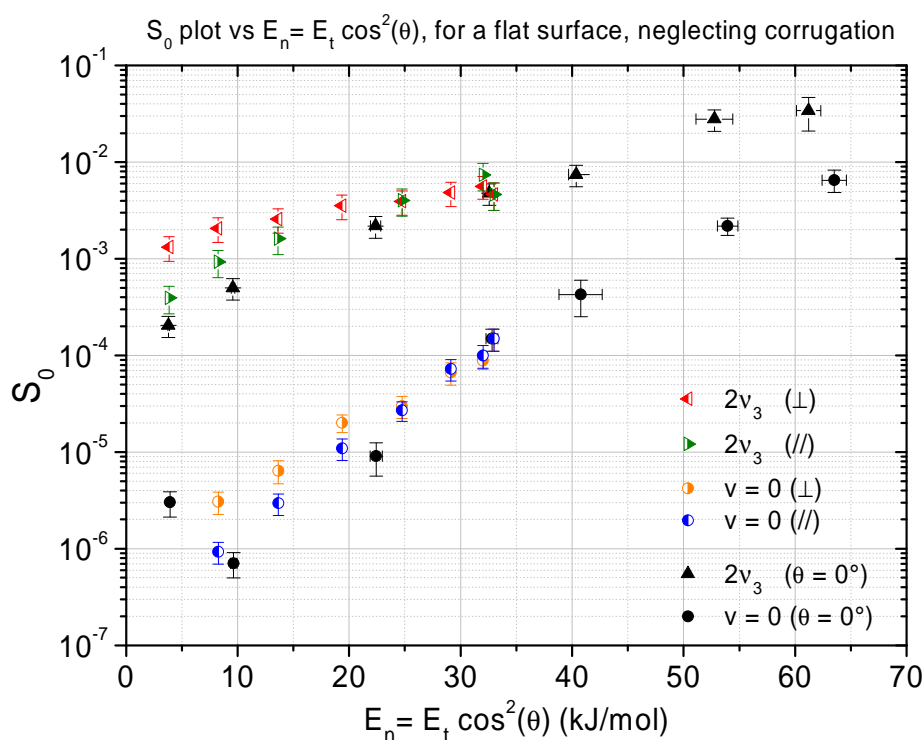
Figure 4.12 Chemisorption probability of CH_4 on Pt(110) as a function of the normal translational energy at $T_s = 400$ K. (▲): $2\nu_3$, $\theta = 0°$ (normal incidence); (■): ground-state, $\theta = 0°$ (normal incidence); (▶): $2\nu_3$, $\varphi = 0°(//)$; (◀): $2\nu_3$, $\varphi = 90°$ (⊥); (◐): ground-state, $\varphi = 90°$ (⊥); (◑): ground-state, $\varphi = 0°$ (//).

We can observe that the sticking coefficient measurements at $\varphi = 0°$ (//) plot vs E_n agree reasonably well with the S_0 obtained at $\theta = 0°$ (normal incidence). This observation suggests that, when the molecules hit the surface along the missing rows, only the normal energy effectively contributes to bring the molecules above the reaction barrier. However, when the surface is rotated 90° and the molecules impinge perpendicularly to the rows, we observe that the S_0 on Pt(110) (⊥) is systematically higher than the S_0 measured at normal incidence. The observation that normal energy scaling is not valid for molecules incident perpendicularly to the atomic rows could be due to the fact that that the molecules "see" a much higher corrugation when the surface is oriented at $\varphi = 90°$. We will now apply the scaling equation 4.3, which takes into account the local normal of the surface, and test if the higher reactivity of CH_4 at $\varphi = 90°$

can be understood in terms of local normal energy scaling. In Figure 4.13 the normal energy was calculated using the formula proposed by Xia and Engstrom (equation 4.3).
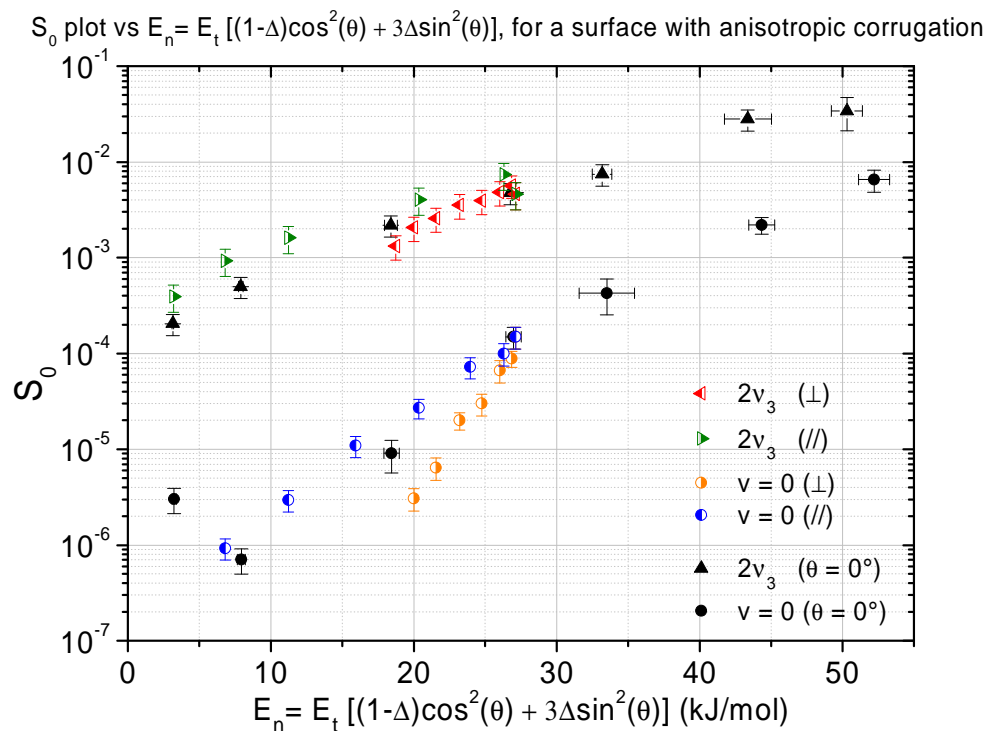
Figure 4.13 Chemisorption probability of CH_4 on Pt(110) as a function of the local normal translational energy (Δ = Xia and Engstrom[121]) (eq. 4.3), T_s = 400 K. (▲): $2\nu_3$, θ = 0° (normal incidence); (■): ground-state, θ = 0° (normal incidence); (▷): $2\nu_3$, φ = 0°(//); (◁): $2\nu_3$, φ = 90° ($\perp$); (◑): ground-state, φ = 90° ($\perp$); (◐): ground-state, φ = 0° (//).

We can observe that the v = 0 data series for φ = 90°, scaled with equation 4.3, does not fall on the same trend-line of the φ = 0° data. This means that the different reactivity of the methane on the two azimuthal orientations cannot be rationalized in terms of a pure local-normal scaling effect. In fact, according to Xia and Engstrom, the scaling equation 4.3 does not take into account possible shadowing effects that can be significant for the highly corrugated Pt(110) surface and large angle of incidence. In the following, we discuss how azimuthally dependent shadowing effects can explain the different reactivity of methane on the two different azimuthal configurations.

4.6.2.2 Shadowing Effects

Figure 4.14 shows the results of our state-resolved measurements for the methane in the $2\nu_3$ state and for the laser-off depositions as function of polar angle of incidence.
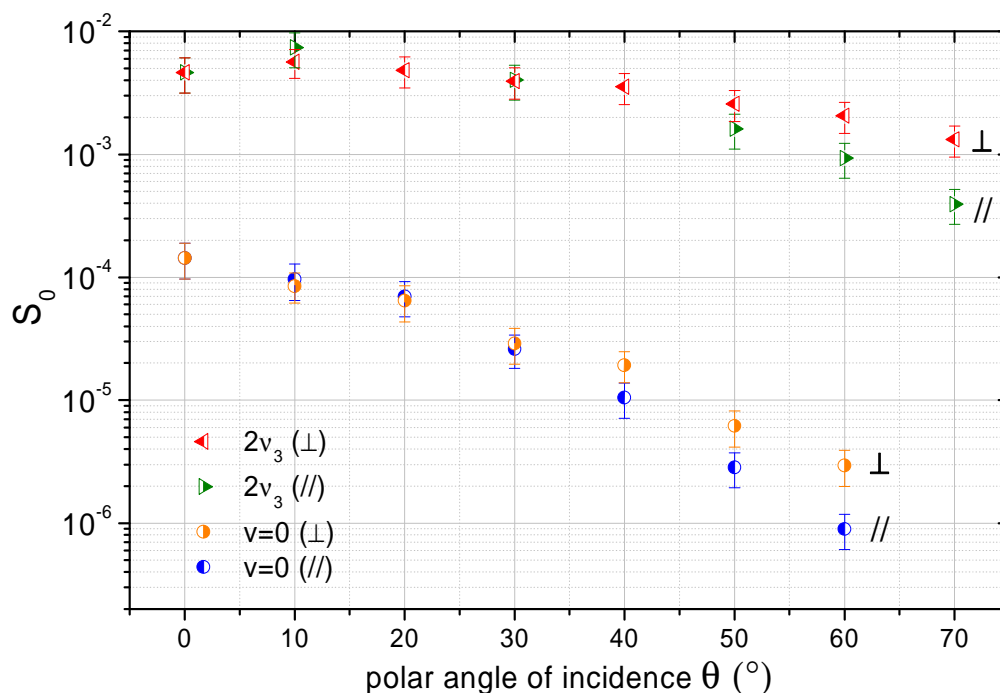
Figure 4.14 Initial sticking coefficient of CH_4 on Pt(110)-(1×2) (T_s = 400 K). The total kinetic energy is kept constant E_t = 32 kJ/mol and we measured S_0 as a function of the polar angle of incidence (θ) and two, mutually orthogonal, azimuthal configurations described in Figure 4.9. (▶): $2\nu_3$, φ = 0° (//). (◀): $2\nu_3$, φ = 90° ($\perp$). (◐): laser off, φ = 90°. (◑): laser off, φ = 0°.

The sticking coefficient $S_0^{(\perp)}$ for the perpendicular azimuthal orientation (φ = 90°) drops less quickly than the sticking coefficient $S_0^{(//)}$ for the parallel orientation (φ = 0°) as the polar angles of incidence increases. In our experiment the difference is detectable only for θ greater than 40°. The maximum difference in reactivity that we have observed is at θ = 60° for (GS) and at θ = 70° ($2\nu_3$ state), where S_0 of methane on Pt(110) ($\perp$) is ~3 times higher than on Pt(110) (//).

We interpret these results in terms of a "shadowing effect" due to the strongly anisotropic corrugation of the Pt(110)-(1×2) surface that occurs for the ⊥ incidence but not for the // incidence. It is important to note that initially only some fraction of the 2nd and 3rd layer Pt atoms are shadowed and , increasing θ, the methane molecules will collide preferentially with the atop atom sites as illustrated schematically in Figure 4.16. From the structure of the Pt(110)-(1×2) surface, described in detail in section 4.2, one can derive a so called "shadowing" angle of approximately ~ 55° (Figure 4.15).
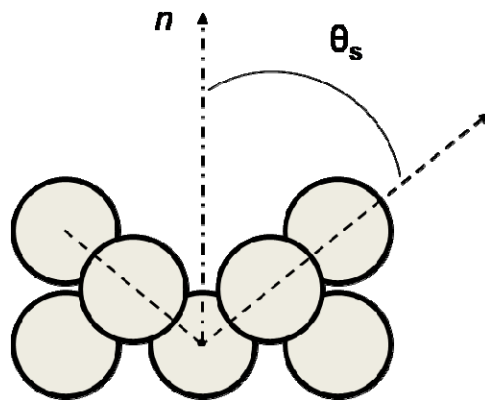
Figure 4.15 The Pt(110)-(1×2) surface has a strong corrugation along the [001] direction due to the missing rows reconstruction. Experimental investigations[107, 108, 111, 122] and *ab-initio* calculations[106] have reported slightly different values of shadowing angle in the range $55° < θ_s < 61°$. Geometrically, this shadowing angle corresponds to the angle between the $[1\overline{1}0]$ direction and the plane of the (111) microfacets.
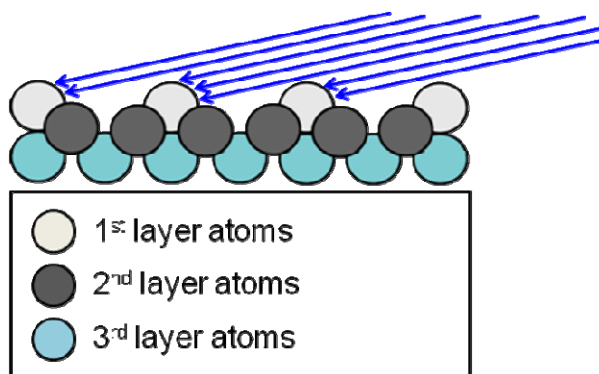
Figure 4.16 Schematic representation of methane molecules incident of the Pt(110)-(1×2) surface perpendicularly to the missing rows, with an angle of incidence θ > 50°. With this azimuthal configuration the molecules can directly hit only the atop atoms sites, since the hollow sites are shadowed by the vicinal top-layer rows.

4.6.2.3 Site-selective chemisorption

The fact that we observe higher reactivity for θ > 50° in the ⊥ azimuthal orientation than for the // orientation, where no shadowing occurs, suggest that the reactivity of the atop sites is higher than for trough sites in the 2nd and 3rd layer. From these observations we can deduce the presence of a significant difference in the energy barrier height for CH_4 dissociation on the different sites, pointing to the presence of a strong geometric corrugation of the PES for this reaction system [7, 119, 120].

Although Anghel *et al*. did not report the energy barriers on all the possible adsorption sites, the results of their DFT calculations suggested that the minimum reaction barrier for methane on Pt(110)-(1×2) is located on the ridge-atop atom sites (Figure 4.6), in agreement with our experimental results. For the Pt(110) (//) orientation, if we increase θ, CH_4 can always probe with equal probability all the adsorption sites, on the contrary, for Pt(110) (⊥), increasing the angle of incidence we can lead the molecules to probe preferentially the ridge atoms, hence the most favorable sites for dissociation[116].

These results have also a more general significance because we showed that we can control not only the translational, vibrational and rotational energy of the incident molecules, but also the specific site on the surface that the molecules hit. In this way we can bring the state-resolved measurements one step forward, toward the complete control of the reaction degrees of freedom.

Furthermore, the complete control of the reaction parameters provides also information that are highly valuable to theoreticians in order to calculate valid PES for gas/surface reactions.

4.6.2.4   Reactivity of low coordinated surface atoms

Recent high-resolution photoelectron spectroscopy measurements reported by Bianchettin *et al.*[118] provide an explanation for the higher reactivity of the 1st layer atoms. In their work Bianchettin and coworkers have investigated the electronic structure of Pt adatoms and small Pt clusters (Pt_N) on the Pt(111) surface measuring the Pt$4f_{7/2}$ core level shift. Then they performed DFT calculations to correlate the core level shifts (CLS) with the density of states in the Pt5d band and found that reducing the size of the Pt atoms cluster on the surface shifts the d-band center towards the Fermi level (Figure 4.17). They finally concluded that decreasing the size of the Pt clusters, hence the coordination of the adsorbed Pt atoms, increase their reactivity as they have a more favorable electronic configuration.
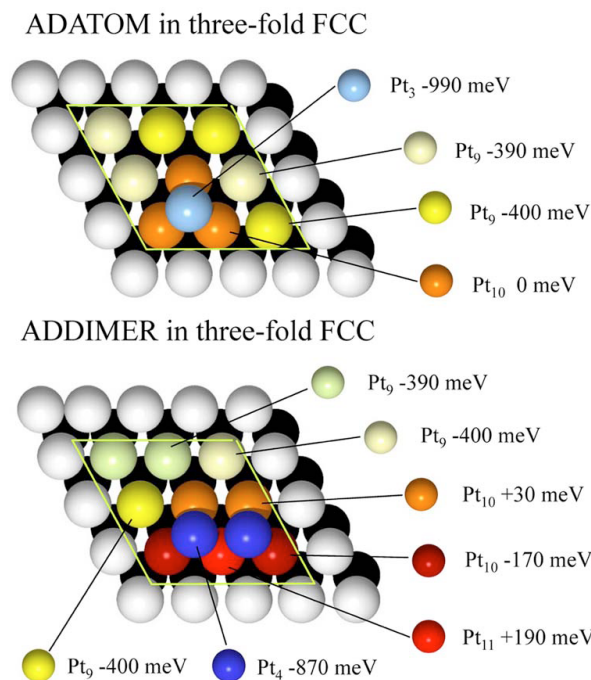
Figure 4.17 Top view of the structural models for the Pt/ Pt(111) surface for the adatom (a) and the ad-dimer (b) configurations used in the DFT calculations reported by Bianchettin *et al.*[118]. The Pt$_i$ atoms with different coordination number are denoted with different colors. The corresponding calculated CLSs are indicated.

Their conclusions are based on the Hammer and Nørskov[88] "*d*-band model", which correlates the position of the *d*-band center, with respect to the Fermi level, to the reactivity of metal surfaces. Hammer and Nørskov found that H_2 and O_2 dissociate easily on transition metals that have a *d*-band close to the Fermi level[88, 123]. Following the conclusions of Bianchettin *et al.* we can understand why CH_4 would adsorb preferentially on the atop sites of Pt(110)-(1×2). In fact, on the Pt(110)-(1×2) surface, the first layer atoms are less coordinated than the second and third layer atoms. Since Bianchettin *et al.* have reported that the less coordinated Pt surface atoms have a smaller *d*-band shift, we therefore propose that a favorable electronic configuration may be the cause of the higher reactivity of CH_4 on the atop atoms.

4.6.3 Washboard model of the CH_4/Pt(110)-(1×2) interaction

4.6.3.1 Sinusoidal surface corrugation

In order to interpret in a more quantitative way the effect of the Pt(110)-(1×2) surface corrugation on the reactivity, I have developed a simple model of the CH_4/Pt(110)-(1×2) interaction based on the *washboard model* originally proposed by Tully[124]. I make use of the fact that the corrugation of the Pt(110)-(1×2) is anisotropic, meaning that the shadowing of the part of 2nd and 3rd atomic layers is possible only for $\varphi = 90°$ ($\perp$). As in the washboard model of Tully, I describe the surface in the perpendicular azimuthal orientation with a sinusoidal function having periodicity equal to the Pt(110)-(1×2) unit cell:

$$z(x) = R \cos\left(\frac{\pi x}{a_0}\right) \quad \textbf{(4.3)}$$

where $R = 1.39$ Å is the Pt atomic radius, $a_0 = 3.92$ Å is the dimension of the FCC cubic unit cell of Pt, z is the coordinate relative to the [110] direction and x is the coordinate relative to the [001] direction (perpendicular to the missing rows) (Figure 4.9).

In this model, I describe the methane molecule as a hard sphere having radius r = 1.85 Å (Clark *et al.*[125]). We will assume that the hard sphere molecules move towards the surface until they will hit the surface hard wall potential described (Figure 4.18). Since the function 4.3 is periodic, we can limit our consideration to a single unit cell.
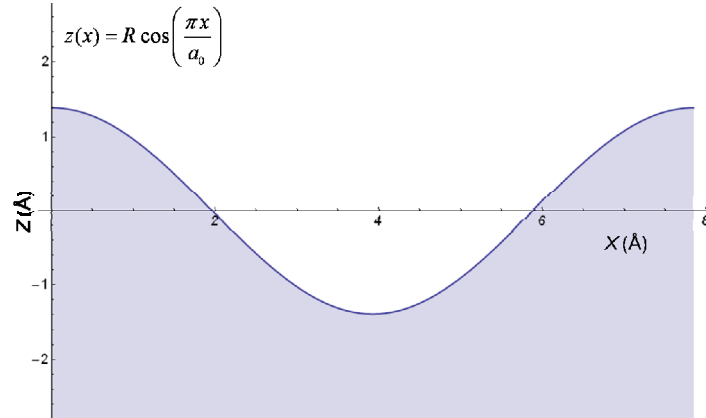
Figure 4.18 In the washboard model of the Pt(110)-(1×2) surface, the corrugation along the [001] direction is modeled with a sinusoidal function (equation 4.3) which parameters (amplitude and periodicity) are the height and length of the surface unit cell[106].

4.6.3.2 Trajectory of the incident molecules

With this simplified model we want to calculate, for a given incidence angle, the amount of surface that is shadowed by the first layer atoms. I calculate the point of impact of the molecules from the intersection of the trajectory of the molecules centre of mass (*CoM*) and the periodic surface. The trajectory of the centre of mass of the incident molecule is described by a straight line. This is a simplification of the real trajectory since the attractive potential of the surface could significantly steer the molecules when they approach the surface. Furthermore, I assume that the initial sticking coefficient, as a function of the angle of incidence θ and the azimuthal orientation ($\perp$ and $//$), can be expressed as the sum of the individual sticking probabilities on the first, second and third layer Pt atoms:

$$S_0^{\perp}(\theta) = c_1^{\perp} S_0^{1st} + c_2^{\perp} S_0^{2nd} + c_3^{\perp} S_0^{3rd} \qquad \textbf{(4.4)}$$

$$S_0^{//}(\theta) = c_1^{//} S_0^{1st} + c_2^{//} S_0^{2nd} + c_3^{//} S_0^{3rd} \qquad \textbf{(4.5)}$$

where the coefficients $c_i^{//}$ and $c_i^{\perp}$ (with $i = 1,2,3$) are the fraction of i-layer sites that are hit by molecules for the $//$ and $\perp$ orientation respectively and S_0^{1st}, S_0^{2nd} and S_0^{3rd} express the adsorption probability on 1st, 2nd and 3rd layer Pt atoms. For the $//$ orientation the coefficients $c_i^{//}$ do not change in function of θ because no shadowing occurs. For the $\perp$ orientation, $c_i^{\perp} = c_i^{\perp}(\theta)$.

From geometric considerations, we can see that the shadowing angle of the surface described by equation 4.3 is determined by the slope of the line tangent to the inflection point of surface $(d^2z(x)/dx^2 = 0)$. In the unit cell $(0 < x < 2a_0)$, the line described by equation 4.3 has inflection points at $x = a_0/2$ and $x = 3a_0/2$. If we assume that the molecules approach the surfaces coming from the left to the right of Figure 4.19, it is sufficient to consider only the inflection point at $x = a_0/2$. From the derivative of equation 4.3:

$$\frac{dz(x)}{dx} = -\frac{R\pi}{a_0}\sin\left(\frac{\pi x}{a_0}\right) \qquad \textbf{(4.6)}$$

we can calculate the angular coefficient of the line tangent to $z = 0$, $x = a_0/2$. From the angular coefficient we can obtain the shadowing angle $\theta_S \approx 42°$. The difference between the shadowing angle that we calculated and the experimental value $\theta_S \approx 55°$ determined by Adams *et al.*[122] is due to the fact that we use a smooth sinusoidal function to model the real surface. The next step will be to determine where the molecules hit the surface for a given angle of incidence. The position of the top three layers atoms [107, 108, 111, 122] is known, hence we can divide the surface unit cell length in different zones corresponding to the projections of the atoms onto the sinusoidal function (Figure 4.19).
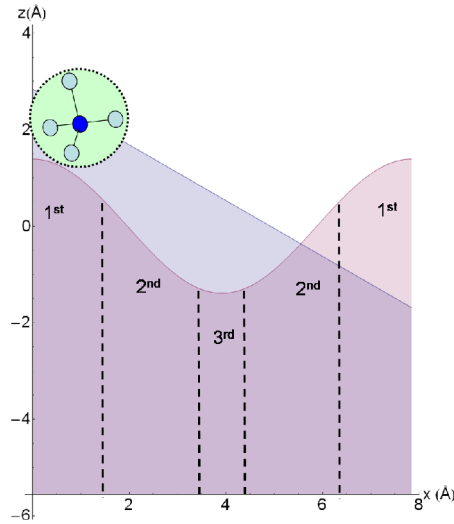
Figure 4.19 Knowing the positions of the atoms in the unit cell [122] we can divide the sinusoidal curve that describe the surface in different zones determined by the projections of the first three layers atoms onto the sinusoidal hard wall potential.

4.6.3.3   Determination of the impact site

The mathematical problem consists in finding, for a given angle θ, the point of intersection of a line (the CoM trajectory of CH_4) and a sinusoidal curve (the Pt(110)-(1×2) surface). This problem cannot be solved analytically, so I have used the calculus software *Mathematica* 6 to find the solutions numerically. From the coordinates (x_i, z_i) of the impact point we can determine if the molecules will collide with a first, second or third layer atom. Now our goal is to calculate the values of coefficients $c_i^{//}$ and $c_i^{\perp}$ in equation 4.4 and 4.5. We can distinguish two cases, based on the values of the angles φ and θ. In the first case (Figure 4.20 a) the molecules are incident on the surface for:

$\varphi = 0°, \theta \geq 0°$ **(4.7 a)**

or

$\varphi = 90°, 0° \leq \theta \leq \theta_s$ **(4.7 b)**

In this case the molecules can hit every point of the surface, hence:

$$c_i^{//} \equiv c_i^{\perp} = \sum_n l_{i,n} \Big/ \sum_i \sum_n l_{i,n} = l_i / 2a_0 \quad \textbf{(4.8)}$$

where l_i is the sum of the projection of the exposed part of the atoms of the ith-*layer* onto the x axis (Figure 4.20 a). For the three atomic layers we can write down explicitly the sums for $i = 1...3$: $l_1 = l_{1,1} + l_{1,2}$; $l_2 = l_{2,1} + l_{2,2}$; $l_3 = l_{3,1}$.

In the second case (Figure 4.20 b) the molecules are incident on the surface in the perpendicular azimuthal orientation and with an angle of incidence greater than the shadowing angle:

$$\varphi = 90°, \ \theta \geq \theta_s$$
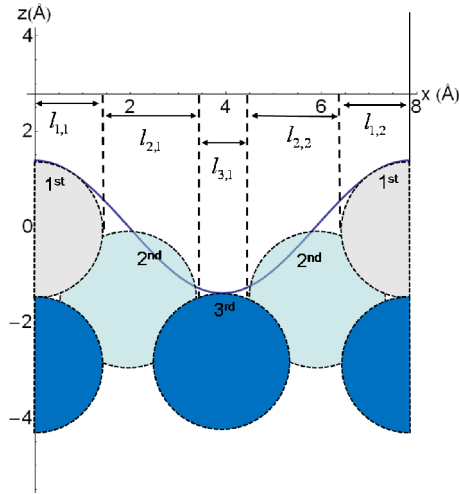
(a)   **(b)**
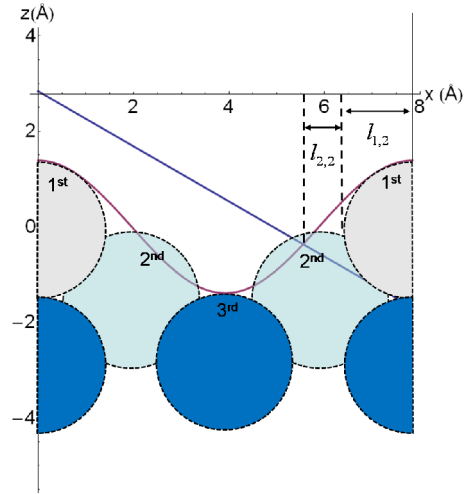
Figure 4.20 The coefficients $c_i^{//}$ and $c_i^{\perp}$ are given by the ratio of $l_i/2a_0$ where l_i is the sum of the projection of the exposed part of the atoms of the ith-*layer* onto the x axis. (a) ($\varphi = 0°$, $\theta \geq 0°$) or ($\varphi = 90°$, $0° \leq \theta \leq \theta_s$): the molecules can hit every point of the surface and so $c_i^{//} \equiv c_i^{\perp} = l_i/2a_0 = \sum_n l_{i,n} \Big/ 2a_0$. For the three atomic layers we can write down explicitly the sums for $i = 1...3$: $l_1 = l_{1,1} + l_{1,2}$; $l_2 = l_{2,1} + l_{2,2}$; $l_3 = l_{3,1}$. (b) ($\varphi = 90°$, $\theta \geq \theta_s$): part of the surface is shadowed by the 1st layer atoms. In this case the coefficients $c_i^{\perp}$ are given by: $c_1^{\perp} = l_{1,2}/(l_{1,2} + l_{2,2})$; $c_2^{\perp} = l_{2,2}/(l_{1,2} + l_{2,2})$.

In this case part of the surface is shadowed by the 1st layer atoms and the coefficients $c_i^\perp$ are given by:

$$c_i^\perp = \sum_n l_{i,n} \Big/ \sum_i \sum_n l_{i,n} \qquad \textbf{(4.9)}$$

where this time the sum at the denominator is only extended to the area of the surface that is not shadowed. In particular, in Figure 4.20 b, we consider the case where the molecules can stick only on 2nd and 1st layer atoms than $c_3^\perp = 0$, and the coefficients $c_1^\perp$ and $c_2^\perp$ are given by:

$$c_1^\perp = l_{1,2} / (l_{1,2} + l_{2,2}); \quad c_2^\perp = l_{2,2} / (l_{1,2} + l_{2,2}).$$

Now I define a parameter called *enh* obtained from equation 4.4 and 4.5:

$$enh = \frac{S_0^\perp(\theta)}{S_0^{//}(\theta)} = \frac{c_1^\perp S_0^{1st} + c_2^\perp S_0^{2nd} + c_3^\perp S_0^{3rd}}{c_1^{//} S_0^{1st} + c_2^{//} S_0^{2nd} + c_3^{//} S_0^{3rd}} \qquad \textbf{(4.10)}$$

This parameter expresses the relative change of reactivity (*enh* stands for "enhancement") between the two configurations ($\perp$ and $//$) as the angle of incidence is increased from 0° (normal incidence).

4.6.3.4   Comparison with experimental data

We have experimentally measured $S_0^\perp(\theta)$ and $S_0^{//}(\theta)$ and we can numerically evaluate $c_i^\perp$ and $c_i^{//}$ as a function of θ, in this way the unknowns in equations 4.10 are only the values of S_0^{1st}, S_0^{2nd} and S_0^{3rd}. Furthermore, the third layer atoms are already completely shadowed when $\theta = \theta_s$, meaning that the 3rd layers sites do not contribute to the global surface reactivity after the angle of incidence is increased above θ_s. In this way, for $\theta \geq \theta_s$, equation 4.10 simplifies into:

$$enh = \frac{c_1^{\perp} S_0^{1st} + c_2^{\perp} S_0^{2nd}}{c_1^{//} S_0^{1st} + c_2^{//} S_0^{2nd}} \qquad (4.11)$$

We have now to solve equation 4.11 imposing the condition:

$$0 \leq (S_0^{1st}, S_0^{2nd}) \leq 1. \qquad (4.12)$$

This condition is due to the fact that the molecules can stick on the surface with initial probability $0 \leq S_0 \leq 1$. It turns out that equation 4.11 does not have solutions that satisfy conditions 4.12, in particular we found that, in order to solve equation 4.11, the sticking coefficient S_0^{2nd} should be < 0, that is physically impossible. Although we cannot find analytically an acceptable solution for equation 4.11, we can still apply our model to see if it can reproduce in a qualitative way the evolution of enh as a function of θ. The exact numerical solution of equation 4.11 can be approximated by $S_0^{2nd} \rightarrow 0$, in this way we can assume that $S_0^{1st} \gg S_0^{2nd}$, and equation 4.11 can be simplified into:

$$enh \approx \frac{c_1^{\perp}}{c_1^{//}} \qquad (4.13)$$

To calculate enh with equation 4.13 we have to evaluate the coefficients c_i as a function of θ applying equation 4.8 and 4.9 (Figure 4.21).

(a)   Pt(110)-(1×2), $\varphi = 90°$ (//)   **(b)**   Pt(110)-(1×2), $\varphi = 90°$ ($\perp$)
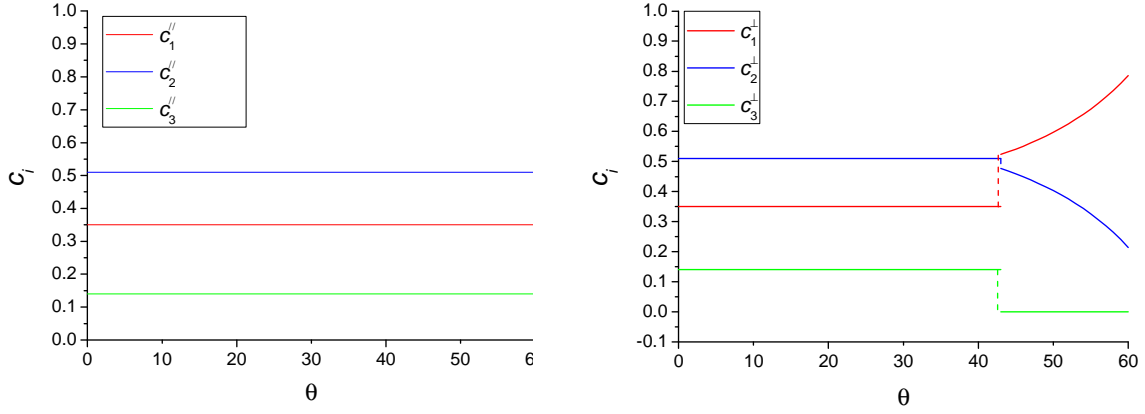
Figure 4.21 $c_i^{//}$ and $c_i^{\perp}$ (with $i = 1,2,3$) are the fraction of i-layer sites that can be hit by molecules for the $//$ and $\perp$ orientation respectively (equation 4.8 and 4.9).

When the surface is in the parallel configuration ($\varphi = 0°$) the coefficients c_i do not vary as θ is increased, because no shadowing is possible in this configuration (Figure 4.21 a). For $\varphi = 90°$ and $\theta > \theta_s$ we can see in Figure 4.21 (b) that the coefficient c_1 increases and part of the surface is shadowed. It is worth to note that at $60°$ $c_i^{\perp} \approx 90\%$, meaning that the molecules hit almost exclusively only the first layer atoms and our measurements become site-selective.

Now it is possible to compare the experimentally determined ratio $S_0^{\perp}(\theta)/S_0^{//}(\theta)$ with the *enh* calculated by equation 4.11. The result of this comparison is shown in Figure 4.22.
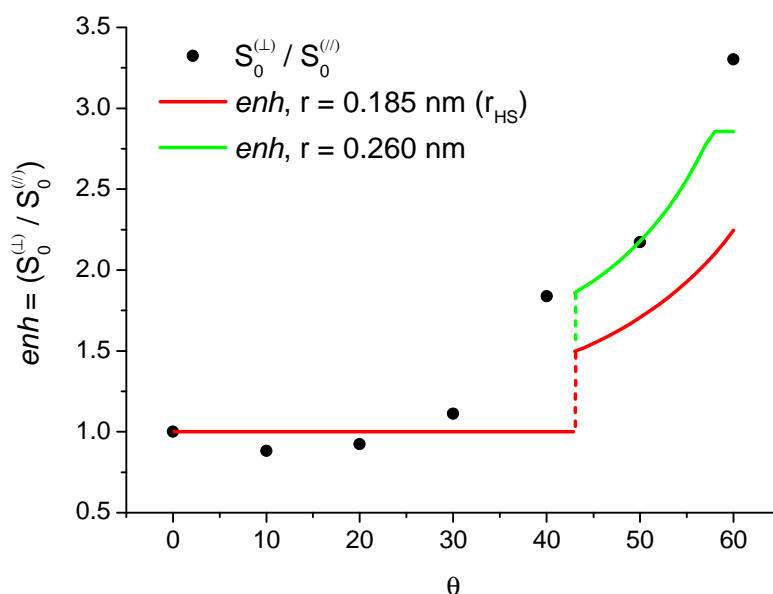
Figure 4.22 (●) $enh = S_0^{\perp}(\theta)/S_0^{//}(\theta)$; ratio between the experimentally measured sticking coefficients as a function of the angle of incidence θ. The red and the green solid lines indicates the parameter *enh* calculated as a function of θ by equation 4.11 ($enh = c_1^{\perp}/c_1^{//}$) using the hard sphere radius of methane (r_{HS} = 1.85 Å [125]) and a best fit radius r = 2.6 Å respectively.

Figure 4.22 shows how this simple model correctly predicts that the surface in the ($\perp$) configuration has higher reactivity than in the (//) configuration as θ is increased above the shadowing angle. Based on the model, our angle dependent data suggests that the reactivity of the top layer sites is significantly higher than the two subsequent layers and essentially dominates the reactivity of the Pt(110) surface. If we increase the radius of the hard spheres from 1.85 to 2.60 Å, the calculated *enh* curve approaches the experimental points. This observation suggests that the real surface is more corrugated than what is predicted by pure geometric considerations, probably due to the presence of an attractive potential close to the surface. It is also worth to note that at high angle (θ ≈ 58°) the *enh* curve for r = 2.60 Å becomes flat because the molecules start to impinge only to the top sites ($c_i^{\perp} = 1$).

4.7 Conclusions

In conclusion, we measured the initial sticking coefficient of CH_4 on Pt(110)-(1x2) as a function of the polar angle and the azimuthal angle of incidence. We observed that the sticking coefficient $S_0^{(\perp)}$ for the perpendicular azimuthal orientation becomes gradually higher than the sticking coefficient $S_0^{(//)}$ for the parallel orientation as the polar angles of incidence increases.

In an effort to interpret these results, we developed a simple washboard/hard sphere model which allow us to evaluate, for a given angle of incidence, the impact point of the molecules with the surface and the amount of surface "shadowed" by the atop atoms. Comparison between the data and the model shows that the latter describes qualitatively well the observed variation in the ratio $S_0^{\perp}(\theta)/S_0^{//}(\theta)$. The model predicts that, at high angle of incidence and for $\varphi = 90°$, the molecules impinge preferentially on the first layer atoms, hence we suggest that the ridge atop atoms are the most favorable sites for dissociation.

Our observations are in agreement with the ab initio calculations of Anghel *et al.*[116] and Bianchettin *et al.*[118]. It is also worth pointing out that we did not introduce in the model any arbitrary parameter to fit the experimental measurements, hence we suggest that our washboard model, in its simplicity, captures the physics of the problem.

Chapter 5: Summary and outlook

5.1 Summary

We performed quantum state-resolved measurements of the CH_4 sticking probability on two platinum surfaces: Pt(111) and Pt(110)-(1×2).

First, on Pt(111), we measured the state-resolved sticking probability of methane excited to the $\nu_1+\nu_4$ and $2\nu_3$ states, which correspond to a stretch-bend combination and a C-H stretch overtone respectively. A very similar reactivity enhancement with respect to ground state molecules was observed upon excitation of the $\nu_1+\nu_4$ and the $2\nu_3$ states, although the $2\nu_3$ state is 21 kJ/mol higher in energy. The different efficacies of these vibrational states (state specificity) is inconsistent with the predictions of the PC-MURT model proposed by the group of Harrison [38, 45, 74, 76-79], since this statistical model assumes that complete intramolecular energy redistribution takes place before the reaction occurs. On the contrary, our results show that memory of the initially excited state is preserved until the molecules reach the transition state.

The vibrationally adiabatic models proposed by Halonen *et al.*[30] and the wavepacket simulations performed by Milot *et al.*[37, 81, 82] predict that vibrational excitation of the ν_1 symmetric stretch mode of methane will enhance the dissociation more effectively than excitation of the asymmetric ν_3 stretch. This qualitative prediction is in good agreement with our results, since we measured a higher vibrational efficacy for the $\nu_1+\nu_4$ state, containing one quantum of symmetric stretch vibration, with respect to the $2\nu_3$ state.

We can also rationalize the higher efficacy of the $\nu_1+\nu_4$ state by observing that at the transition state[75] the breaking C-H bond is both stretched and bent from its equilibrium geometry.

For the Pt(110)-(1×2) surface, we measured the state-resolved reaction probability of CH_4 excited to the vibrational states $2\nu_3$, $\nu_1+\nu_4$ and $2\nu_2+\nu_4$. Our measurements show that vibrational excitation enhances the dissociation probability of methane on Pt(110)-(1×2) up to 3 orders of

magnitude with respect to ground state molecules. As seen for CH_4 on Pt(111), excitation of the $\nu_1+\nu_4$ state produces a similar increase in reactivity to that of the more energetic $2\nu_3$ state. Furthermore, it is also observed that the $\nu_1+\nu_4$ state has 50% higher vibrational efficacy than the nearly isoenergetic $2\nu_2+\nu_4$ state. This is a clear indication that the chemisorption of CH_4 on Pt(110)-(1×2) is "state-specific"[6, 36].

Ab initio calculations performed by Anghel *et al.*[116] show that the transition state structure for the dissociation of methane on Pt(110)-(1×2) involves simultaneous stretch and bend of the breaking C-H bond. Indeed, we have observed that the $\nu_1+\nu_4$ state has higher efficacy than both the $2\nu_2+\nu_4$ and $2\nu_3$ states, therefore, our results suggest that excitation of a vibrational state that maps the reaction coordinate is the most efficient way to vibrationally activate the chemisorption.

The similar vibrational efficacies of the $\nu_1+\nu_4$ and $2\nu_3$ states on the Pt(110) and Pt(111) suggest similarity in the CH_4 TS structure upon these surfaces. Comparison between the transition state geometries reported by Psofogiannakis *et al.*[75] for CH_4 on Pt(111) and by Anghel *et al.* [116] for CH_4 on Pt(110) confirm this hypothesis.

For the Pt(110)-(1×2) surface, we also measured the initial sticking coefficient of CH_4 on Pt(110)-(1×2) as a function of the polar angle and the azimuthal angle of incidence. We observed that, as the polar angle of incidence increases, the sticking coefficient $S_0^{(\perp)}$ of methane incident perpendicularly to the atomic rows becomes gradually higher than the sticking coefficient $S_0^{(//)}$ of methane incident along the missing rows. We interpret these results in terms of a "shadowing effect" due to the strong anisotropic corrugation of the Pt(110)-(1×2) surface.

In order to rationalize these results we developed a simple washboard/hard sphere model which allows us to evaluate, for a given angle of incidence, the impact point of the molecules with the surface and the amount of surface "shadowed" by the atop atoms. With this model we estimate that, at high angle of incidence ($\theta \geq 60°$) and for $\varphi = 90°$ ($\perp$ azimuthal configuration), the molecules impinge preferentially on the first layer atoms. The higher reactivity of the $\perp$ configuration suggests, in agreement with the *ab initio* calculation of Anghel *et al.*[116], that the minimum reaction barrier on the PES is located on the surface atop atoms.

In conclusion, with our quantum state-resolved measurements we tested the validity of available theoretical models[30, 37, 38] of gas-surface reaction dynamics. Furthermore, our

results provide a new benchmark for theoreticians in order to test and improve the calculation of multidimensional PES for chemisorption reactions.

5.2   Outlook

In this work we have measured the chemisorption probability of methane in its ground state and in several vibrationally excited states, over a wide range of kinetic energies.

In the future, we plan to extend our studies towards higher kinetic energies. Recently we have acquired an Even-Lavie pulsed valve that produces very short molecular beam pulses (~10 µs) and is stable up to 500 K. These extremely short molecular pulses will allow us to increase the fraction of the molecular beam pulse that is illuminated by our cylindrically focused IR laser beam, hence to increase the fraction of vibrationally excited molecules per pulse.

We also plan to continue our investigation of the angular dependence of the sticking probability at higher angle of incidence and for different total translational energy conditions. It is known that surface temperature increases the reaction probability of methane on both Pt(111) and Pt(110), but it will be interesting to investigate how the surface temperatures will affect the reaction probability of vibrationally excited molecules.

With our Auger spectrometer we have a limited sensitivity of ~1% ML of C on a platinum surface. Implementation of a more sensitive technique, like thermal programmed desorption (TPD) could significantly help us to improve the detection limit of our experimental setup.

Currently, our experimental setup is not optimized for TPD measurements, the major limitations is the position of the QMS, which is situated far from the surface and does not collect efficiently the desorbed species. The collection efficiency of the desorbed molecules could be significantly increased by positioning a differentially pumped QMS very close to the surface.

APPENDIX A: Character Table of the T$_d$ group

Table A.1 Character table of the T$_d$ group

T$_d$	E	8C$_3$	3C$_2$	6S$_4$	6σ_d		
A$_1$	1	1	1	1	1		$\alpha_{xx}+\alpha_{yy}+\alpha_{zz}$
A$_2$	1	1	1	-1	-1		
E	2	-1	2	0	0		$(\alpha_{xx}+\alpha_{yy}-2\alpha_{zz}, \alpha_{xx}-\alpha_{yy})$
F$_1$	3	0	-1	1	-1	(R_x, R_y, R_z)	
F$_2$	3	0	-1	-1	1	(T_x, T_y, T_z)	$(\alpha_{xy},\alpha_{xz},\alpha_{yz})$

APPENDIX B: Program for CRD spectroscopy

I wrote, using National Instrument LabVIEW 7.0, a program for the data acquisition of the signal from our CRD spectroscopy setup (Figure A.1).

This program performs the analog to digital conversion (ADC) of the exponential decay cavity-ring-down signal coming from the output of a FGA-10 IR photodiode, positioned near the exit mirror of the CRD chamber. The signal is collected through a data acquisition card (NI DAC 6115) that allow us to acquire the signal with a sample rate of 10 Ms (10^7 points per seconds), the signal is then digitized with a 12 bit resolution in range of $\pm$ 0.2 V, meaning that we can acquire the CRD signal with voltage resolution of 0.1 mV. The analog signal acquisition is triggered by the voltage signal coming from a Thorlabs photodiode, that collects the part of a back reflection of the 1064 nm beam of our laser setup.
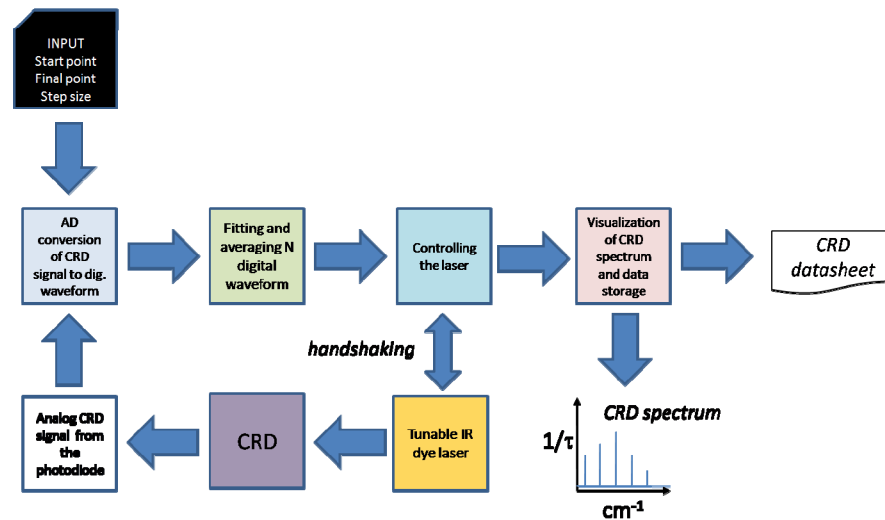
Figure A.1 Schematic flowchart of the CRD program

After the digitalization, the program performs a series of computational steps to fit the exponential decay curves and obtain the cavity ring-down time. It is also possible to average the results of a series of N of these fits, we typically average twenty, to improve the signal to noise ratio of the measurement. The resulting CRD time is then displayed in function of the laser

115

wavelength. In order to scan the laser (LambdaPhysik ScanMatePro) and collect the data synchronously, the program is able to command the execution of the laser scan steps via a RS32 serial port. This program has a graphical interface in which is possible to enter the initial and final position of the laser scan and the amplitude of the step. The CRD spectrum is visualized on the display and updated after every scan step. At the end of the scan it is possible to save the collected data in a spreadsheet format.

LIST OF FIGURES

119

121

LIST OF TABLES

BIBLIOGRAPHY

1.   *Molecules on surfaces.* 2007 [cited; Available from: http://nobelprize.org.
2.   Bernstein, R.B. and R.D. Levine, *Molecular Reaction Dynamics and Chemical Reactivity*. 1987: Oxford University Press.
3.   Masel, R.I., *Principles of Adsorption and Reaction on Solid Surfaces*. 1996, New York: Wiley
4.   Lui, S.C., J.W. Davenport, E.W. Plummer, D.M. Zehner, and G.W. Fernando, *Electronic-Structure Of Nial.* Physical Review B, 1990. **42**(3): p. 1582-1597.
5.   Lennard-Jones, J.E., *PROCESSES OF ADSORPTION AND DIFFUSION ON SOLID SURFACES.* Trans. Farady Soc., 1932. **28**: p. 333–359.
6.   Maroni, P., *Bond- and Mode- Specific Reactivity of Methane on Ni(100)*, in *Chemistry*. 2005, Swiss Federal Institute of Technology: Lausanne.
7.   Darling, G.R. and S. Holloway, *The dissociation of diatomic molecules at surfaces.* Rep. Prog. Phys., 1995. **58**: p. 1595-1672.
8.   Halstead, D. and S. Holloway, *The influence of potential energy surface topologies on the dissociation of H_2.* The Journal of Chemical Physics, 1990. **93**(4): p. 2859-2870.
9.   Levine, R.D. and R.B. Bernstein, *Molecular Reaction Dynamics and Chemical Reactivity*. 1987, New York: Oxford University Press.
10.   Kroes, G.J., E.J. Baerends, and R.C. Mowrey, *Six-Dimensional Quantum Dynamics of Dissociative Chemisorption of (v=, j=) H2 on Cu(100).* Physical Review Letters, 1997. **78**(18): p. 3583.
11.   Kroes, G.J., A. Gross, E.J. Baerends, M. Scheffler, and D.A. McCormack, *Quantum Theory of Dissociative Chemisorption on Metal Surfaces.* Acc. Chem. Res., 2002. **35**(3): p. 193-200.
12.   Polanyi, J.C., *Concepts in reaction dynamics.* Acc. Chem. Res., 1972. **5**(5): p. 161-168.
13.   Pijper, E., G.J. Kroes, R.A. Olsen, and E.J. Baerends, *Reactive and diffractive scattering of H2 from Pt(111) studied by six-dimensional wave packet method.* The Journal of Chemical Physics, 2002. **117**(12): p. 5885.
14.   Rettner, C.T., H.A. Michelsen, and D.J. Auerbach, *Quantum-state-specific dynamics of the dissociative adsorption and associative desorption of H_2 at a Cu(111) surface.* The Journal of Chemical Physics, 1995. **102**(11): p. 4625.
15.   Gross, A., S. Wilke, and M. Scheffler, *Six-Dimensional Quantum Dynamics of Adsorption and Desorption of H2 at Pd(100): Steering and Steric Effects.* Physical Review Letters, 1995. **75**(14): p. 2718.
16.   Crim, F.F., *Bond-Selected Chemistry: Vibrational State Control of Photodissociation and Bimolecular Reaction.* Journal Of Physical Chemistry, 1996. **100**(31): p. 12725-12734.
17.   Crim, F.F., *Vibrational State Control of Bimolecular Reactions: Discovering and Directing the Chemistry.* Acc. Chem. Res., 1999. **32**(10): p. 877-884.

18. Yoon, S., S. Henton, A.N. Zivkovic, and F.F. Crim, *The relative reactivity of the stretch-bend combination vibrations of CH₄ in the CL(2P3/2) + CH₄ reaction.* The Journal of Chemical Physics, 2002. **116**(24): p. 10744.

19. Corchado, J.C., D.G. Truhlar, and J. Espinosa-Garcia, *Potential energy surface, thermal, and state-selected rate coefficients, and kinetic isotope effects for Cl + CH₄ --> HCl + CH₃.* The Journal of Chemical Physics, 2000. **112**(21): p. 9375-9389.

20. Duncan, W.T. and T.N. Truong, *Thermal and vibrational-state selected rates of the CH₄+Cl <--> HCl+CH₃ reaction.* The Journal of Chemical Physics, 1995. **103**(22): p. 9642-9652.

21. Espinosa-Garcia, J. and J.C. Corchado, *Analytical potential energy surface for the CH₄+Cl --> CH₃+ClH reaction: Application of the variational transition state theory and analysis of the kinetic isotope effects.* The Journal of Chemical Physics, 1996. **105**(9): p. 3517-3523.

22. Bechtel, H.A., Z.H. Kim, J.P. Camden, and R.N. Zare, *Bond and mode selectivity in the reaction of atomic chlorine with vibrationally excited CH₂D₂.* The Journal of Chemical Physics, 2004. **120**(2): p. 791-799.

23. Yoon, S., R.J. Holiday, and F.F. Crim, *Vibrationally Controlled Chemistry: Mode- and Bond-Selected Reaction of CH3D with Cl.* Journal of Physical Chemistry B, 2005. **109**(17): p. 8388-8392.

24. Yoon, S., R.J. Holiday, E.L. Sibert Iii, and F.F. Crim, *The relative reactivity of CH₃D molecules with excited symmetric and antisymmetric stretching vibrations.* The Journal of Chemical Physics, 2003. **119**(18): p. 9568-9575.

25. Yan, S., Y.-T. Wu, B. Zhang, X.-F. Yue, and K. Liu, *Do Vibrational Excitations of CHD3 Preferentially Promote Reactivity Toward the Chlorine Atom?* Science, 2007. **316**(5832): p. 1723-1726.

26. Scoles, G., D. Bassi, U. Buck, and D. Laine, *Atomic and Molecular Beam Methods Vol I.* 1 ed. Atomic and Molecular Beam Methods, ed. G. Scoles. Vol. 1. 1988, New York: Oxford University Press.

27. Scoles, G., D. Laine, and U. Valbusa, *Atomic and Molecular Beam Methods Vol II.* Atomic and Molecular Beam Methods, ed. G. Scoles. Vol. 2. 1992, New York: Oxford University Press.

28. Juurlink, L.B.F., P.R. McCabe, R.R. Smith, C.L. DiCologero, and A.L. Utz, *Eigenstate-resolved studies of gas-surface reactivity: CH₄(v₃) dissociation on Ni(100).* Phys. Rev. Lett., 1999. **83**(3): p. 868.

29. Holmblad, P.M., J. Wambach, and I. Chorkendorff, *Molecular beam study of dissociative sticking of methane on Ni(100).* The Journal of Chemical Physics, 1995. **102**(20): p. 6255.

30. Halonen, L., S.L. Bernasek, and D.J. Nesbitt, *Reactivity of vibrationally excited methane on nickel surfaces.* The Journal of Chemical Physics, 2001. **115**(12): p. 5611.

31. Higgins, J., A. Conjusteau, G. Scoles, and S.L. Bernasek, *State selective vibrational (2v3) activation of the chemisorption of methane on Pt(111).* The Journal of Chemical Physics, 2001. **114**(12): p. 5277.

32. Schmid, M.P., P. Maroni, R.D. Beck, and T.R. Rizzo, *Surface reactivity of highly vibrationally excited methane prepared by pulsed laser excitation: CH₄ on Ni(100).* The Journal of Chemical Physics, 2002. **117**(19): p. 8603.

33. Beck, R.D., P. Maroni, D.C. Papageorgopoulos, T.T. Dang, P.M. Schmid, and T.R. Rizzo, *Vibrational mode-specific reaction of methane on a nickel surface.* Science, 2003. **302**: p. 98-100.

34. Smith, R.R., D.R. Killelea, D.F. DelSesto, and A.L. Utz, *Preference for Vibrational over Translational Energy in a Gas-Surface Reaction.* Science, 2004. **304**: p. 4.

35. Juurlink, L.B.F., R.R. Smith, D.R. Killelea, and A.L. Utz, *Comparative Study of C-H Stretch and Bend Vibrations in Methane Activation on Ni(100) and Ni(111).* Physical Review Letters, 2005. **94**(20): p. 208303-4.

36. Maroni, P., D.C. Papageorgopoulos, M. Sacchi, T.T. Dang, R.D. Beck, and T.R. Rizzo, *State-resolved gas/surface reactivity of methane in the symmetric C-H stretch vibration on Ni(100).* Physical Review Letters, 2005. **94**: p. 246104.

37. Milot, R. and A.P.J. Jansen, *Ten-dimensional wave packet simulations of methane scattering.* The Journal of Chemical Physics, 1998. **109**(5): p. 1966-1975.

38. Ukraintsev, V.A. and I. Harrison, *A statistical model for activated dissociative adsorption: Application to methane dissociation on Pt(111).* The Journal of Chemical Physics, 1994. **101**(2): p. 1564-1581.

39. Schmid, M.P., P. Maroni, R.D. Beck, and T.R. Rizzo, *Molecular beam apparatus for vibrationally controlled surface chemistry by pulsed laser radiation.* Rev. Sci. Instr., 2003. **74**(9): p. 11.

40. Schmid, M., *Interaction of Highly Excited Molecules with Solid Surfaces*, in *Chemistry.* 2002, Swiss Federal Institute of Technology: Lausanne.

41. Dang, T.T., *Quantum state-resolved studies of direct and precursor-mediated dissociative chemisorption of silane on Si(100)*, in *Chemistry.* 2007, Swiss Federal Institute of Technology: Lausanne.

42. Matsunami, N., Y. Yamamura, Y. Itikawa, and N. Itoh, *Energy Dependence of the Yields of Ion-Induced Sputtering of Monatomic Solids.* 1983: IPPJ-AM-32.

43. King, D.A. and M.G. Wells, *Molecular beam investigation of adsorption kinetics on bulk metal targets: Nitrogen on tungsten.* Surface Science, 1972. **29**(2): p. 454-482.

44. King, D.A. and M.G. Wells, *Molecular-Beam Investigation of Adsorption Kinetics on Bulk Metal Targets - Nitrogen on Tungsten.* Surface Science, 1972. **29**(2): p. 454.

45. DeWitt, K.M., L. Valadez, H.L. Abbott, K.W. Kolasinski, and I. Harrison, *Using Effusive Molecular Beams and Microcanonical Unimolecular Rate Theory to Characterize CH_4 Dissociation on Pt(111).* 2006. p. 6705-6713.

46. Janin, E., M. Göthelid, and U.O. Karlsson, *Formation of two-dimensional graphite islands on the Pt(110) (1 X 2) surface.* App. Surf. Sci., 2000. **162-163**: p. 184-189.

47. Bisson, R., M. Sacchi, T.T. Dang, B. Yoder, P. Maroni, and R.D. Beck, *State-Resolved Reactivity of $CH_4(2v_3)$ on Pt(111) and Ni(111): Effects of Barrier Height and Transition State Geometry. .* J. Phys. Chem. A, 2007. **111**: p. 12679-12683.

48. Armstrong, D.J., W.J. Alford, T.D. Raymond, A.V. Smith, and M.S. Bowers, *Parametric amplification and oscillation with walkoff-compensating crystals.* J. Opt. Soc. Am. B, 1997. **14**: p. 460.

49. Sutherland, R., *Handbook of nonlinear optics.* Vol. 1. 1996.

50. Meijer, G., M.G.H. Boogaarts, R.T. Jongma, D.H. Parker, and A.M. Wodtke, *Coherent Cavity Ring Down Spectroscopy.* Chemical Physics Letters, 1994. **217**(1-2): p. 112-116.

51. Herzberg, G., *Molecular Spectra and Molecular Structure Volume II. Infrared and Raman Spectra of Polyatomic Molecules.* 2 ed. 1989, Malabar, Florida 32950: Krieger Publishing Company.

52. Gray, D.L. and A.G. Robiette, *Extended measurement and analysis of the v_3 infrared band of methane.* Journal Of Molecular Spectroscopy, 1979. **77**: p. 440-456.

53. Robiette, A.G., D.L. Gray, and F.W. Birss, *The effective vibration-rotation hamiltonian for triply-degenerate fundamentals of tetrahedral XY4 molecules.* Molecular Physics, 1976. **32**(6): p. 1591-1607.

54. Margolis, J.S., *Measured line positions and strengths of methane between 5500 and 6180 cm^{-1}.* App. Opt., 1988. **27**(19): p. 4038-4051.

55. Fox, K., *Vibration-rotation interactions in infrared active overtone levels of spherical top molecules; $2v_3$ and $2v_4$ of CH_4,$2v_3$ of CD_4.* Journal Of Molecular Spectroscopy, 1962. **9**: p. 381-420.

56. Rothman, L.S., *The Hitran Molecular Spectroscopic Database and HAWKS.* J. Quant. Spectrosc. Radiat. Transfer, 1996. **60**(5): p. 665-710.

57. Wenger, C. and J.P. Champion, *Spherical top data system (STDS) software for the simulation of spherical top spectra.* Journal of Quantitative Spectroscopy and Radiative Transfer, 1998. **59**(3-5): p. 471-480.

58. Wang, X.-G. and E.L.S. III, *A nine-dimensional perturbative treatment of the vibrations of methane and its isotopomers.* The Journal of Chemical Physics, 1999. **111**(10): p. 4510.

59. Hilico, J.-C., O. Robert, M. Loëte, S. Toumi, A.S. Pine, and L.R. Brown, *Analysis of the Interacting Octad System of 12CH4.* Journal of Molecular Spectroscopy, 2001. **208**: p. 1-13.

60. Hilico, J.-C., O. Robert, M. Loëte, S. Toumi, A.S. Pine, and L.R. Brown, *Analysis of the Interacting Octad System of 12CH4.* Journal Of Molecular Spectroscopy **208**: p. 1-13.

61. Bisson, R., T.T. Dang, M. Sacchi, and R.D. Beck, *Cavity ring-down spectroscopy of jet-cooled silane isotopologues in the Si--H stretch overtone region.* The Journal of Chemical Physics, 2007. **127**(24): p. 244301-6.

62. Hippler, M. and M. Quack, *High-resolution Fourier transform infrared and cw-diode laser cavity ringdown spectroscopy of the $v_2 + 2 v_3$ band of methane near 7510 cm^{-1} in slit jet expansions and at room temperature.* The Journal of Chemical Physics, 2002. **116**(14): p. 6045-6055.

63. Besenbacher, F., I. Chorkendorff, B.S. Clausen, B. Hammer, A.M. Molenbroek, J.K. Norskov, and I.I. Stensgaard, *Design of a Surface Alloy Catalyst for Steam Reforming.* Science, 1998. **279**: p. 1913.

64. Larsen, J.H. and I. Chorkendorff, *From fundamental studies of reactivity on single crystals to the design of catalysts.* Surf. Sci. Rep., 1999. **35**: p. 163-222.

65. Juurlink, L.B.F., R.R. Smith, and A.L. Utz, *The role of rotational excitation in the activated chemisorption of vibrationally excited methane on Ni(100).* Faraday Discuss., 2000. **117**: p. 147-160.

66. Juurlink, L.B.F., R.R. Smith, and A.L. Utz, *Controlling Surface Chemistry with Light: Spatially Resolved Deposition of Rovibrational-State-Selected Molecules.* J. Phys. Chem. B, 2000. **104**: p. 10.

67. Luntz, A.C. and D.S. Bethune, *Activation of methane dissociation on a Pt(111) surface.* The Journal of Chemical Physics, 1989. **90**(2): p. 1272-1280.

68. Chen, P., I.V. Tomov, and P.M. Rentzepis, *Laser-induced transient structure and stress in a platinum(111) crystal studied by time-resolved X-ray diffraction.* Journal of Applied Crystallography, 1999. **32**(1): p. 82-88.

69. Davey, W.P., *Precision Measurements of the Lattice Constants of Twelve Common Metals.* Physical Review, 1925. **25**(6): p. 753.

70. Oakes, D.J., M.R.S. McCoustra, and M.A. Chesters, *Dissociative Adsorption of Methane on Pt(111) induced by Hyperthermal Collisions.* Faraday Discuss., 1993. **96**: p. 325-336.

71. Egeberg, R.C., S. Ullmann, I. Alstrup, C.B. Mullins, and I. Chorkendorff, *Dissociation of CH_4 on Ni(111) and Ru(0001).* Surface Science, 2002. **497**(1-3): p. 183-193.

72. Schoofs, G.R., C.R. Arumainayagam, M.C. McMaster, and R.J. Madix, *Dissociative Chemisorption of Methane on Pt(111).* Surf. Sci., 1989. **215**: p. 1.

73. Nesbitt, D.J. and R.W. Field, *Vibrational Energy Flow in Highly Excited Molecules: Role of Intramolecular Vibrational Redistribution.* J. Phys. Chem., 1996. **100**(31): p. 12735-12756.

74. Bukoski, A. and I. Harrison, *Assessing a microcanonical theory of gas-surface reactivity: Applicability to thermal equilibrium, nonequilibrium, and eigenstate-resolved dissociation of methane on Ni(100).* The Journal of Chemical Physics, 2003. **118**(21): p. 9762-9768.

75. Psofogiannakis, G., A. St-Amant, and M. Ternan, *Methan Oxidation Mechanism on Pt(111): A Cluster Model DFT Study.* J. Phys. Chem. B, 2006. **110**: p. 24593.

76. Abbott, H.L., A. Bukoski, and I. Harrison, *Microcanonical unimolecular rate theory at surfaces. II. Vibrational state resolved dissociative chemisorption of methane on Ni(100).* The Journal of Chemical Physics, 2004. **121**(8): p. 3792-3810.

77. Abbott, H.L., A. Bukoski, D.F. Kavulak, and I. Harrison, *Dissociative chemisorption of methane on Ni(100): Threshold energy from $CH_4(2v_3)$ eigenstate-resolved sticking measurements.* The Journal of Chemical Physics, 2003. **119**(13): p. 6407-6410.

78. Bukoski, A., H.L. Abbott, and I. Harrison, *Microcanonical unimolecular rate theory at surfaces. III. Thermal dissociative chemisorption of methane on Pt(111) and detailed balance.* The Journal of Chemical Physics, 2005. **123**(9): p. 094707-18.

79. Bukoski, A., D. Blumling, and I. Harrison, *Microcanonical unimolecular rate theory at surfaces. I. Dissociative chemisorption of methane on Pt(111).* The Journal of Chemical Physics, 2003. **118**(2): p. 843-871.

80. Cortright, R.D., R.R. Davda, and J.A. Dumesic, *Hydrogen from catalytic reforming of biomass-derived hydrocarbons in liquid water.* Nature, 2002. **418**(6901): p. 964-967.

81. Milot, R. and A.P.J. Jansen, *Energy distribution analysis of the wavepacket simulations of CH_4 and CD_4 scattering.* Surface Science, 2000. **452**(1-3): p. 179-190.

82. Milot, R. and A.P.J. Jansen, *Bond breaking in vibrationally excited methane on transition-metal catalysts.* Physical Review B, 2000. **61**(23): p. 15657.

83. Burghgraef, H., A.P.J. Jansen, and R.A. van Santen, *Electronic structure calculations and dynamics of methane activation on nickel and cobalt.* The Journal of Chemical Physics, 1994. **101**(12): p. 11012-11020.

84. Lee, M.B., Q.Y. Yang, and S.T. Ceyer, *Dynamics of the activated dissociative chemisoprtion of CH_4 and implication for the pressure gap in catalysis: A molecular beam-high resolution electron energy loss study.* The Journal of Chemical Physics, 1987. **87**(5): p. 2724.

85. Anderson, A.B. and J.J. Maloney, *Activation of methane on iron, nickel, and platinum surfaces: a molecular orbital study.* J. Phys. Chem., 1988. **92**(3): p. 809-812.

86. Wittborn, A.M.C., M. Costas, M.R.A. Blomberg, and P.E.M. Siegbahn, *The C--H activation reaction of methane for all transition metal atoms from the three transition rows.* The Journal of Chemical Physics, 1997. **107**(11): p. 4318-4328.

87. Luntz, A.C., *A simple model for associative desorption and dissociative chemisorption.* The Journal of Chemical Physics, 2000. **113**(16): p. 6901.

88. Hammer, B. and J.K. Norskov, *Electronic factors determining the reactivity of metal surfaces.* Surface Science, 1995. **343**(3): p. 211-220.

89. Kitchin, J.R., J.K. Norskov, M.A. Barteau, and J.G. Chen, *Modification of the surface electronic and chemical properties of Pt(111) by subsurface 3d transition metals.* The Journal of Chemical Physics, 2004. **120**(21): p. 10240-10246.

90. Nave, S. and B. Jackson, *Methane dissociation on Ni(111): The effects of lattice motion and relaxation on reactivity.* The Journal of Chemical Physics, 2007. **127**(22): p. 224702-11.

91. Kratzer, P., B. Hammer, and J.K. Norskov, *A theoretical study of CH_4 dissociation on pure and gold-alloyed Ni(111) surfaces.* The Journal of Chemical Physics, 1996. **105**(13): p. 5595-5604.

92. Yang, H. and J.L. Whitten, *Dissociative chemisorption of CH_4 on Ni(111).* The Journal of Chemical Physics, 1992. **96**(7): p. 5529-5537.

93. Luntz, A.C. and F.W. Harold, *Dissociation of methane and ethane on Pt(110): Evidence for a direct mechanism under thermal conditions.* The Journal of Chemical Physics, 1994. **101**(12): p. 10980-10989.

94. Sun, Y.K.-. and W.H. Weinberg, *Kinetics of dissociative adsorption of methane and ethane on Pt(110)-(1 x 2).* Journal Of Vacuum Science & Technology A-Vacuum Surfaces And Films, 1990. **8**: p. 2445.

95. McMaster, M.C. and R.J. Madix, *Alkane dissociation dynamics on Pt(110)-(1X2).* The Journal of Chemical Physics, 1993. **98**(12): p. 9963.

96. Walker, A.V. and D.A. King, *Dynamics of the Dissociative Adsorption of Methane on Pt{110}(1 X 2).* Physical Review Letters, 1999. **82**(25): p. 4.

97. Walker, A.V. and D.A. King, *Dynamics of dissociative methane adsorption on metals: CH_4 on Pt{110}(1X2).* The Journal of Chemical Physics, 2000. **112**(10): p. 10.

98. Walker, A.V. and D.A. King, *A molecular-beam study of methane dissociative adsorption on oxygen-precovered Pt{110}(1×2).* Surf. Sci., 2000. **444**: p. 6.

99. Seets, D.C., C.T. Reeves, B.A. Ferguson, M.C. Wheeler, and C.B. Mullins, *Dissociative chemisorption of methane on Ir(111): Evidence for direct and trapping-mediated mechanisms.* The Journal of Chemical Physics, 1997. **107**(23): p. 10229-10241.

100. Seets, D.C., M.C. Wheeler, and C.B. Mullins, *Mechanism of the dissociative chemisorption of methane over Ir(110)" trapping-mediated or direct?* Chemical Physics Letters, 1997. **266**: p. 6.

101. Seets, D.C., M.C. Wheeler, and C.B. Mullins, *Trapping-mediated and direct dissociative chemisorption of methane on Ir(110): A comparison of molecular beam and bulb experiments.* The Journal of Chemical Physics, 1997. **107**(10): p. 13.

102. Bonzel, H.P. and S. Ferrer, *A new model for the reconstructed (110)-1 x 2 surfaces of Ir, Pt and Au.* Surface Science, 1982. **118**(1-2): p. L263-L268.

103. Daw, M.S., *Calculations of the energetics and structure of Pt(110) reconstruction using the embedded atom method.* Surface Science, 1986. **166**(2-3): p. L161-L169.

104. Brocksch, H.J. and K.H. Bennemann, *Tight-binding study of the structural stability of the (110) surface of the 5d-transition metals Ir, Pt and Au.* Surface Science, 1985. **161**(2-3): p. 321-341.

105. Foiles, S.M., *Reconstruction of fcc (110) surfaces.* Surface Science, 1987. **191**(1-2): p. L779-L786.

106. Lee, J.I., W. Maanstadt, and A.J. Freeman, *Multilayer-relaxed structure of the (1 X 2) Pt(110) surface.* Phys. Rev. B, 1999. **59**(3): p. 1673.

107. Fenter, P. and T. Gustafsson, *Structural analysis of the Pt(110)-(1 <rm>x</rm> 2) surface using medium-energy ion scattering.* Physical Review B, 1988. **38**(15): p. 10197.

108. Fery, P., W. Moritz, and D. Wolf, *Structure determination of the (1 <rm>x</rm> 2) and (1 <rm>x</rm> 3) reconstructions of Pt(110) by low-energy electron diffraction.* Physical Review B, 1988. **38**(11): p. 7275.

109. Masson, F. and J.W. Rabalais, *Time-of-flight scattering and recoiling spectrometry (TOF-SARS) analysis of Pt{110} : I. Quantitative structural study of the clean (1 x 2) surface.* Surface Science, 1991. **253**(1-3): p. 245-257.

110. Sowa, E.C., M.A. Van Hove, and D.L. Adams, *The missing-row model for the reconstructed Pt(110)-(1 x 2) surface: A leed intensity analysis showing multilayer distortions.* Surface Science, 1988. **199**(1-2): p. 174-182.

111. Vlieg, E., I.K. Robinson, and K. Kern, *Relaxations in the missing-row structure of the (1 x 2) reconstructed surfaces of Au(110) and Pt(110).* Surface Science, 1990. **233**(3): p. 248-254.

112. Speller, S., J. Kuntze, T. Rauch, J. Bömermann, M. Huck, M. Aschoff, and W. Heiland, *The (1 x 2) and (1 x 4) structure on clean Pt(110) studied by STM, AES and LEED.* Surface Science, 1996. **366**: p. 9.

113. Tsay, J.S., F.C. Shyu, T.I. Fu, and C.S. Shern, *Adsorption and Absorption of Hydrogen on a Pt(ll0) Surface.* CHINESE JOURNAL OF PHYSICS, 1993. **32**: p. 10.

114. Engstrom, J.R., J.S. Tsay, and W.H. Weinberg, *The chemisorption of hydrogen on the (111) and (110)-(1 X 2) surfaces of iridium and platinum.* The Journal of Chemical Physics, 1987. **87**(5): p. 16.

115. Lee, M.B., Q.Y. Yang, S.L. Tang, and S.T. Ceyer, *Activated dissociative chemisorption of CH_4 on Ni(111): Observation of a methyl radical and impication.* The Journal of Chemical Physics, 1986. **85**(3): p. 1693.

116. Anghel, A.T., D.J. Wales, S.J. Jenkins, and D.A. King, *Pathways for dissociative methane chemisorption on Pt{110}(1 X 2).* Physical Review B, 2005. **71**: p. 4.

117. Beckerle, J.D., R.R. Cavanagh, M.P. Casassa, E.J. Heilweil, and J.C. Stephenson, *Subpicosecond transient infrared spectroscopy of adsorbates. Vibrational dynamics of CO/Pt(111).* The Journal of Chemical Physics, 1991. **95**(7): p. 5403-5418.

118. Bianchettin, L., A. Baraldi, S. de Gironcoli, E. Vesselli, S. Lizzit, L. Petaccia, G. Comelli, and R. Rosei, *Core level shifts of undercoordinated Pt atoms.* The Journal of Chemical Physics, 2008. **128**(11): p. 114706-6.

119. Darling, G.R. and S. Holloway, *The role of parallel momentum in the dissociative adsorption of H_2 at highly corrugated surfaces.* Surface Science Letters, 1994. **304**: p. L461-L467.

120. Dürr, M. and U. Höfer, *Dissociative adsorption of molecular hydrogen on silicon surfaces.* Surface Science Reports, 2006. **61**: p. 465-526.

121. Xia, L.-Q. and J.R. Engstrom, *The role of surface corrugation in direct translationally activated dissociative adsorption.* The Journal of Chemical Physics, 1994. **101**(6): p. 5329.

122. Adams, D.L., H.B. Nielsen, M.A. Van Hove, and A. Ignatiev, *LEED study of the Pt(110)-(1 x 2) surface.* Surface Science, 1981. **104**(1): p. 47-62.

123. Hammer, B. and J.K. Norskov, *Why gold is the noblest of all the metals.* Nature, 1995. **376**: p. 238.

124. Tully, J.C., *Washboard model of the gas-surface scattering.* The Journal of Chemical Physics, 1990. **92**((1)): p. 680.

125. Clark, L.A., A. Gupta, and R.Q. Snurr, *Siting and Segregation Effects of Simple Molecules in Zeolites MFI, MOR, and BOG.* J. Phys. Chem. B, 1998. **102**(35): p. 6720-6731.

Curriculum Vitae

Name: Marco

Family name: Sacchi

Birthplace: Magenta (MI), Italy, 04/09/1976

Permanent address: Largo B. Croce 1, 20011 Corbetta (MI), Italy

e-mail: marco3.sacchi@mail.polimi.it

Education

2004-2008   École Polytechnique Fédérale de Lausanne
             Ph.D. in physical chemistry, with Prof. Rainer D. Beck
             "The effect of molecular vibrations and surface structure on the chemisorption of methane on platinum"

2003-2004   IUSS-Istituto Universitario di Studi Superiori di Pavia
             Master on Material Science

1995-2002   Politecnico di Milano
             Degree in Chemical Engineering, with Prof. Maurizio Masi

Publications

State-resolved gas/surface reactivity of methane in the symmetric C-H stretch vibration on Ni(100), P. Maroni, D. C. Papageorgopoulos, **M. Sacchi**, T. T. Dang, R. D. Beck, T. R. Rizzo, *Physical Review Letters*, 94, 246104 (2005).

State-Resolved Reactivity of CH$_4$(2ν$_3$) on Pt(111) and Ni(111): Effects of Barrier Height and Transition State Location, R. Bisson, **M. Sacchi**, T.T. Dang, B. Yoder, P. Maroni, R.D. Beck, *Journal of Physical Chemistry A*, 111(49),12679 (2007).

Cavity ring-down spectroscopy of jet-cooled silane isotopologues in the Si-H stretch overtone region, R. Bisson, T.T. Dang, **M. Sacchi**, R.D. Beck, *Journal of Chemical Physics,* 127, 244301 (2007)

State-Resolved Reactivity of Vibrationally Excited CH$_4$ on Pt(110)-(1×2), M. Sacchi, R. Bisson, B. Yoder, T.T. Dang, R.D. Beck, 16th Symposium of Atomic and Surface Physics (SASP), Innsbruck University Press, ISBN 978-3-902571-31-1, 212 (2008)

Vibrational Activation in Direct and Precursor-Mediated Chemisorption of SiH$_4$ on Si(100), R. Bisson, T.T. Dang, **M. Sacchi**, R. D. Beck, *Journal of Chemical Physics* (submitted)

Acknowledgements

Foremost, I would like to express my deep gratitude to my advisor, Prof. Rainer D. Beck, for providing me invaluable research guidance and scientific insight.

I would like to gratefully acknowledge Prof. Thomas Rizzo for accepting me in his group.

My sincere gratitude goes to Dr. Regis Bisson, who provided an incredibly valuable and enthusiastic contribution to this thesis work.

For their help and for allowing me to work in a friendly and pleasant work environment, I would like to thank all my colleagues and former members of the "Surface Dynamics Group": Bruce Yoder, Dr. Thanh Tung Dang, Dr. Plinio Maroni and Dr. Dimitrios Papageorgopoulos. I wish to acknowledge Prof. John R. Morris, who gave me highly valuable suggestions while he was visiting our group.

I would like to acknowledge Prof. Pierre Vogel, Prof. Fleming Crim, Dr. Michel Rossi and Dr. Vittorio Fiorin for having accepted to be members of my thesis jury.

I also would like to thank the following people, without whom I could not have successfully accomplished my work.

André Fattet and all the people of the mechanical workshop for their skillful contribution in designing, building and repairing essential scientific equipment.

Gabriel Roch and all the people of the electronic workshop for their patience, efficiency and extraordinary technical ability.